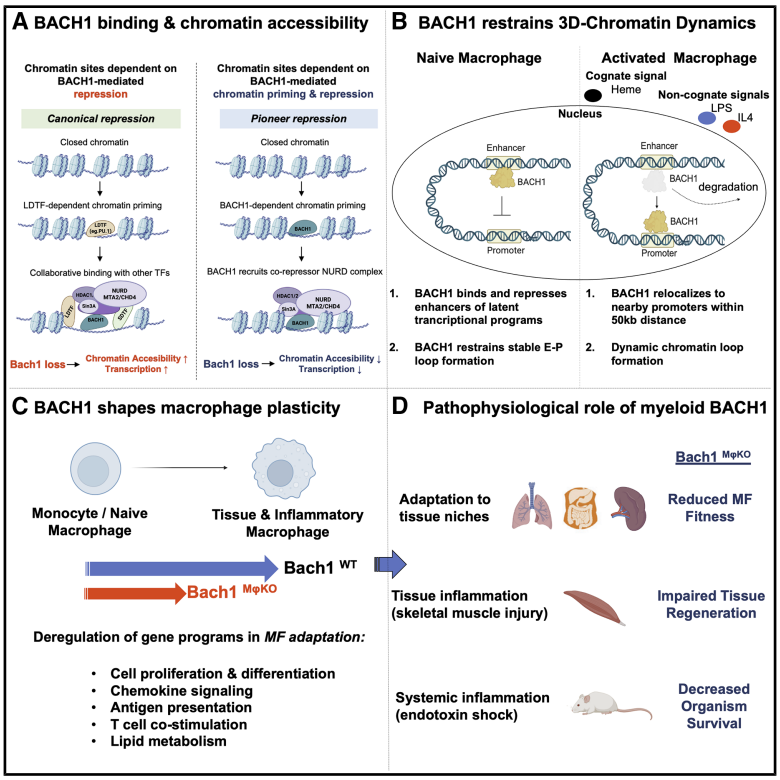
Immunity

The transcription factor BACH1 couples chromatin priming and repression to enable macrophage plasticity and adaptation

Graphical abstract



Highlights

- BACH1 acts as a pioneer repressor coupling chromatin opening with repression
- Inflammatory signals rewire BACH1 binding across enhancer-promoter networks
- BACH1 enables macrophage adaptation across tissue niches
- Myeloid BACH1 shapes local and systemic inflammatory responses *in vivo*

Authors

Petros Tzerpos, Dóra Bojcsuk, Krisztian Bene, ..., John W.R. Schwabe, Dariusz Plewczynski, Laszlo Nagy

Correspondence

lnagy@jhmi.edu

In brief

Macrophage plasticity and function involve precise regulation of transcriptional programs. Tzerpos et al. find that the transcription factor BACH1 establishes early chromatin accessibility while maintaining transcriptionally repressive states in naive macrophages before activation. This dual activity—termed pioneer repression—regulates macrophage adaptation and inflammatory kinetics *in vivo*.

Tzerpos et al., 2026, Immunity *59*, 2465–2482
September 8, 2026 © 2026 The Author(s). Published by Elsevier Inc.
https://doi.org/10.1016/j.immuni.2026.06.022

CellPress

Immunity

CellPress
OPEN ACCESS

Article

The transcription factor BACH1 couples chromatin priming and repression to enable macrophage plasticity and adaptation

Petros Tzerpos,[1,2,12] Dóra Bojcsuk,[1,12] Krisztian Bene,[1,3,12] Noemí Caballero-Sánchez,[1,4] Zofia Parteka-Tojek,[5,6] Krzysztof Banecki,[5,6] Sevastianos Korsak,[5,6] Sarah M. Pritchett,[7] Andreas Patsalos,[3] Darby Oleksak,[3] Wilhelm K. Berger,[3] Michalis E. Sarris,[3] Nikolaos Giannakis,[1] Sophie Chantalat,[8] Timea Cseh,[1] Evangelia K. Papachristou,[9] Ferenc Erdélyi,[10] Zoltán Máté,[10] Gabor Szabo,[10] Gergely Nagy,[1] Jason S. Carroll,[9] Charalampos G. Spilianakis,[2,11] John W.R. Schwabe,[7] Dariusz Plewczynski,[5,6] and Laszlo Nagy[1,3,13,*]

[1]Department of Biochemistry and Molecular Biology, Faculty of Medicine, University of Debrecen, Debrecen, Hungary
[2]Department of Biology, University of Crete, Heraklion, Greece
[3]Department of Medicine, Johns Hopkins University School of Medicine, Institute for Fundamental Biomedical Research, Johns Hopkins All Children's Hospital, St. Petersburg, FL, USA
[4]Doctoral School of Molecular Cell and Immunobiology, Faculty of Medicine, University of Debrecen, Debrecen, Hungary
[5]Faculty of Mathematics and Information Science, Warsaw University of Technology, Warsaw, Poland
[6]Centre of New Technologies, University of Warsaw, S. Banacha 2c, 02-097, Warsaw, Poland
[7]Leicester Institute of Structural and Chemical Biology, Department of Molecular and Cellular Biology, University of Leicester, University Road, Leicester LE1 7RH, UK
[8]Centre National de Génotypage, Institut de Génomique, CEA, Evry, France
[9]Cancer Research UK Cambridge Institute, University of Cambridge, Cambridge CB2 0RE, UK
[10]HUN-REN Institute of Experimental Medicine, Hungarian Academy of Sciences, Budapest, Hungary
[11]Institute of Molecular Biology and Biotechnology, Foundation for Research and Technology-Hellas, Heraklion, Greece
[12]These authors contributed equally
[13]Lead contact
*Correspondence: lnagy@jhmi.edu
https://doi.org/10.1016/j.immuni.2026.06.022

SUMMARY

Macrophage activation and tissue adaptation involve precise transcriptional control by lineage-determining transcription factors (LDTFs) and stimulus-dependent TFs. The heme-regulated transcriptional repressor BACH1 clusters with myeloid LDTFs in unstimulated macrophages, suggesting a role in shaping macrophage identity and function. We found that BACH1 bound to both inactive and active regulatory regions, including latent enhancers. BACH1 recruited the NuRD complex and had dual functions, establishing early chromatin accessibility while actively repressing transcription. Upon inflammatory stimulation, BACH1 rapidly redistributed in *cis* to nearby promoters, reshaping chromatin occupancy, motif specificity, and enhancer-promoter interactions. BACH1 constrained 3D chromatin architecture, limiting enhancer mobility and TF complex dynamics. *In vivo*, *Bach1* deletion impaired macrophage polarization and tissue adaptation and limited resilience during systemic and regenerative inflammation. Thus, BACH1 acts as an early chromatin accessibility-priming factor while actively repressing transcription—a regulatory activity that can be defined as pioneer repression—thereby shaping the macrophage epigenome in response to inflammatory and tissue contexts.

INTRODUCTION

Immunocytes patrol, migrate, and reside within diverse tissues, integrating local environmental cues to maintain homeostasis and respond to infection or injury.[1] Among them, macrophages (MFs) exhibit remarkable plasticity, adapting rapidly to tissue-specific signals to execute inflammatory, phagocytic, and reparative functions.[2,3] This adaptability is driven by dynamic transcriptional programs shaped by environmental inputs, including cytokines, metabolites, and pathogen-derived signals.[1,2] Signal integration leads to transient or stable transcriptional reprogramming, shaping multiple cellular states and responses.[4] Tissue-specific transcription factors (TFs), including GATA6 in the peritoneum,[5] PPAR-γ in the lung,[6] and SPI-C in the red pulp of the spleen,[7] contribute to MF subset specialization, underscoring the central role of transcriptional regulation and chromatin organization in MF identity.

Current models of stimulus-dependent transcription posit that lineage-determining transcription factors (LDTFs), such as PU.1 in myeloid cells, function as pioneer factors (PFs) that establish

This is an open access article under the CC BY license (http://creativecommons.org/licenses/by/4.0/).

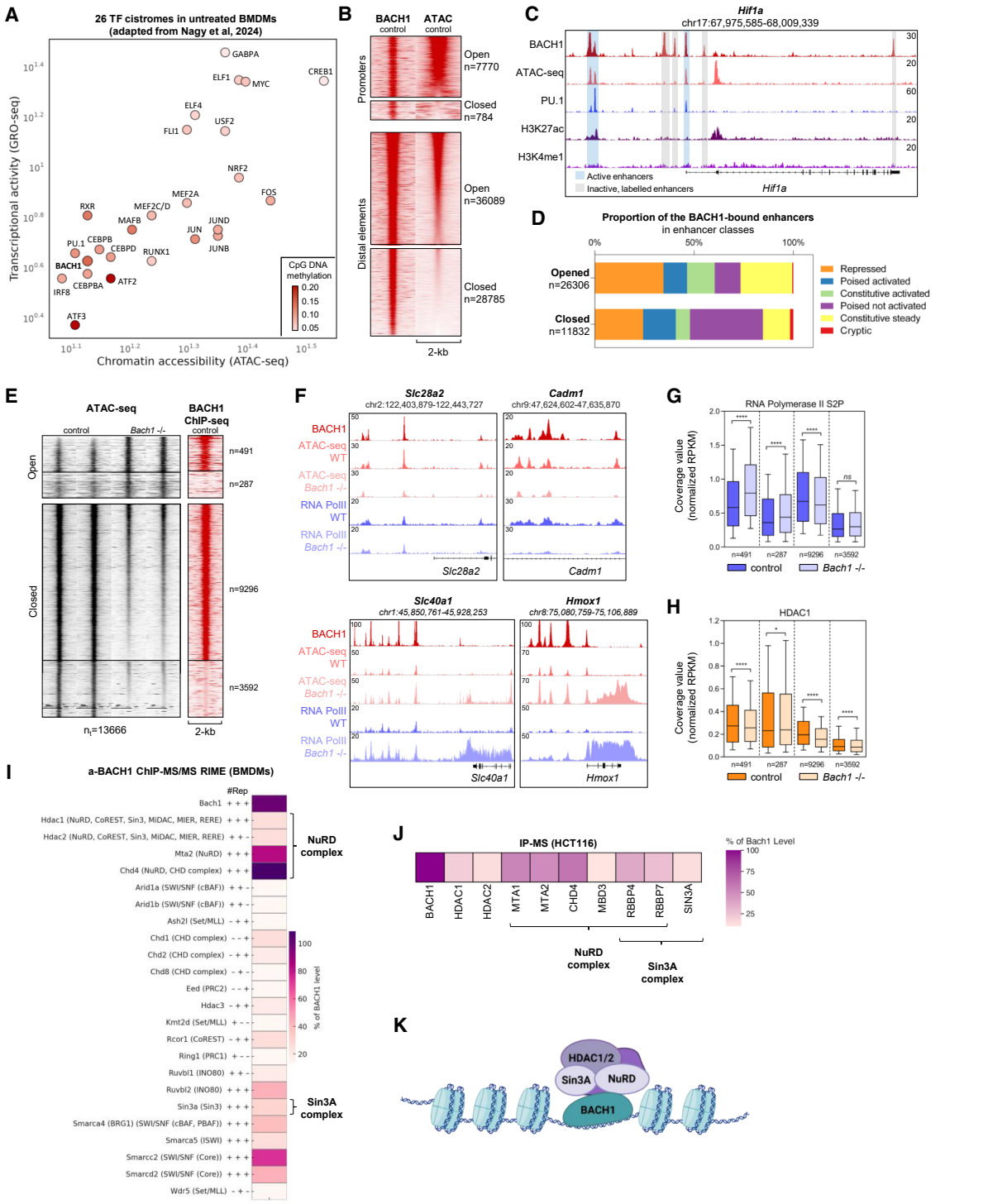


Figure 1. BACH1 acts as a pioneer repressor in macrophages by recruiting the NuRD complex

(A) Correlation of average coverage calculated from ATAC-seq, GRO-seq, and bisulfite-seq data of 26 TFs in naive BMDMs (adapted from Nagy et al.[13]).

(B) Heatmap of read distribution for the BACH1 cistrome clustered with ATAC-seq at enhancers and promoters in naive BMDMs.

(C) Genome track of a representative locus (*Hif1a*) showing BACH1 binding at active and inactive genomic elements.

(D) The proportion of BACH1 binding across six enhancer classes defined by Ostuni et al.[20]

(E) Heatmap showing four clusters of BACH1-bound and unbound regions that are significantly closed or opened in control versus Bach1$^{-/-}$ BMDMs.

(F) Genome tracks of *Slc28a2*, *Cadm1*, *Slc40a1*, and *Hmox1* showing BACH1 ChIP-seq, control and Bach1$^{-/-}$ ATAC-seq, and RNA polymerase II ChIP-seq coverages. ATAC-seq and polymerase II ChIP-seq replicates are overlaid; interval scales and genomic positions are indicated.

(legend continued on next page)

accessible chromatin landscapes and enable recruitment of stimulus-responsive transcription factors (SRTFs).[8,9] However, emerging evidence indicates that pioneering activity is not exclusive to LDTFs; other TFs, such as nuclear factor κB (NF-κB),[10] can also remodel chromatin under specific conditions. Nevertheless, key questions remain regarding how signaling cascades induce chromatin opening, whether a specific initiating mechanism exists, and whether the process is regulated by checkpoints.[11] In addition, although most pioneer TFs are linked to gene activation in cell fate decisions, whether pioneering activity (mediated either by LDTFs or SRTFs) also contributes to gene repression, and whether repressive TFs can establish or maintain inaccessible chromatin states prior to activation, remains unclear.[12]

In analyses of the cistromes of major TFs in unstimulated MFs to identify regulators that cluster with PFs, the transcriptional repressor BACH1 clusters with myeloid LDTFs, including PU.1, CEBPα/β, and IRF8.[13] BACH1 is a CNC-bZip TF that heterodimerizes with small Maf proteins and binds TRE/AP-1-related motifs.[14] Additionally, it possesses a BTB/POZ domain at its N-terminal region,[15] which mediates protein-protein interactions with co-repressors.[16] Its activity is regulated by heme binding, which promotes its destabilization and displacement from chromatin, permitting NRF2-dependent gene activation.[17,18] Although BACH1 is highly expressed in monocytes and tissue MFs,[14] and is proposed to be a core MF regulator,[19] its direct role in shaping MF chromatin architecture and identity has not been systematically defined.

In this study, we examined the role of BACH1 in shaping MF chromatin architecture and identity. In genome-wide epigenomic analyses, BACH1 bound extensively to both inactive and active regulatory regions, including latent enhancers prior to stimulation. BACH1 shaped chromatin accessibility and actively repressed enhancer activation, thereby establishing thresholds for inflammatory and immunomodulatory gene expression in MFs. Both cognate and non-cognate signals altered BACH1 occupancy preferences, resulting in local reshuffling of chromatin binding and the release of emerging enhancer-chromatin interactions in the 3D genome. *In vivo*, loss-of-function studies identified BACH1 as a key regulator of regenerative inflammation and organismal fitness during systemic inflammation. Our data support the hypothesis that BACH1-dependent coupling of chromatin priming with repression, a regulatory activity that we term "pioneer repression," is a critical mechanism for maintaining a primed but actively repressed chromatin landscape, enabling rapid and selective enhancer selection upon activation.

RESULTS

BACH1 binds to open and closed chromatin in naive MFs

Integrative analysis of 26 TF cistromes[13] in unstimulated MFs identified BACH1 as clustering with established myeloid LDTFs, including PU.1, CEBPα/β, and IRF8 (Figure 1A). To define the molecular basis of BACH1-mediated chromatin regulation, we examined its genomic occupancy and functional consequences in naive MFs. Chromatin immunoprecipitation sequencing (ChIP-seq) analysis revealed extensive BACH1 binding across the MF genome, comprising 73,428 sites (Figure S1A). Comparison with cistromes of core myeloid regulators (PU.1, IRF8, CEBPα, CEBPβ, RUNX1, and JUNB) demonstrated widespread co-occupancy at promoters and distal regulatory elements, consistent with integration into core MF transcriptional networks (Figures S1B and S1C). Notably, a substantial fraction of BACH1-bound regions lacked co-binding by these factors, indicating partial independence from canonical myeloid LDTFs. BACH1 occupancy varied quantitatively across genomic sites, allowing stratification into high-, intermediate-, and low-density binding clusters (Figures S1D and S1E). Motif analysis identified enrichment of both canonical MARE motifs and non-canonical TRE-related sequences across all occupancy classes (Figures S1F–S1H), indicating that BACH1 chromatin binding in MFs *in vivo* was extensive and diverse in terms of motif and site specificity.

In addition, we found that BACH1 binding correlated with both open and closed chromatin sites in distal and promoter-proximal genomic regions (Figures 1B and 1C). Importantly, we correlated BACH1 binding with all six previously dynamically defined classes of enhancers (before and after an MF activation stimulus[20]) in MFs (Figure 1D), including poised and latent enhancers, further suggesting a role for BACH1 in active repression of enhancers that were activated only upon stimulation. This binding pattern was consistent with a potential pioneer repressive function in shaping MF chromatin landscapes.

BACH1 acts as a pioneer repressor through association with the NuRD complex

We next examined whether BACH1 directly influences chromatin accessibility at its genomic targets. To this end, we rederived a full-body *Bach1* deletion strain lacking exons 3 and 4 (Bach1−/−) (Figures S2A–S2C) and performed assay for transposase-accessible chromatin using sequencing (ATAC-seq) in control and Bach1−/− bone-marrow-derived macrophages (BMDMs). Loss of BACH1 reduced chromatin accessibility at 9,296 sites, whereas 491 regions became more accessible in Bach1−/− MFs (Figure 1E). To determine whether these accessibility changes impacted transcriptional output, we profiled RNA polymerase II (RNA Pol II) CTD Ser2-phosphorylated occupancy in control and Bach1−/− BMDMs. Regions that lost accessibility upon *Bach1* deletion exhibited reduced elongation-associated Pol II occupancy (Figures 1F and 1G), indicating diminished transcriptional activity. Conversely, sites gaining accessibility in the absence of BACH1 showed increased Pol II occupancy (Figures 1F and 1G). These data demonstrated that BACH1-dependent modulation of chromatin accessibility

(G and H) Boxplots of normalized RNA polymerase II (G) and HDAC1 (H) ChIP-seq coverages (RPKM) in control and Bach1$^{-/-}$ BMDMs across the four clusters shown in (E). Statistical significance was determined by paired *t* test; *$p \leq 0.05$, **$p \leq 0.01$, ***$p \leq 0.001$, ****$p \leq 0.0001$. Whiskers indicate the 10th–90th percentile range and horizontal lines indicate the median.

(I and J) Protein abundance of HDAC1/2 complex subunits and other chromatin regulators identified by a-BACH1 ChIP-MS (RIME) in BMDMs and a-FLAG IP-MS in Bach1Flag HCT116 cells, shown as a percentage of BACH1 levels.

(K) Schematic model of the BACH1-HDAC1/2 complex on chromatin.

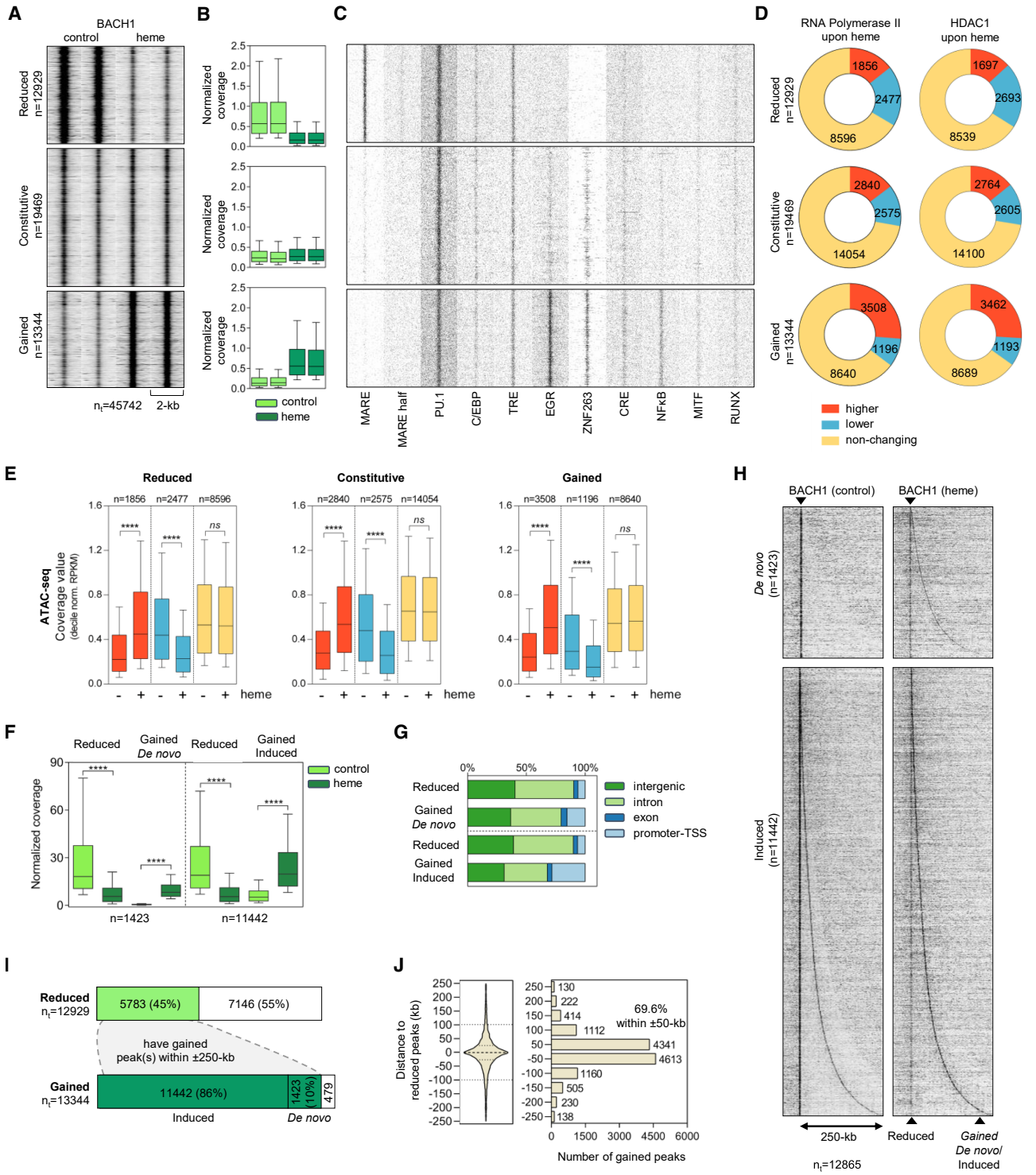


Figure 2. Cognate heme signaling elicits rapid redistribution of BACH1 binding to its local genomic neighborhood

(A) Read distribution heatmap showing significantly reduced and gained ($p \leq 0.05$, FC ≥ 1.5), and constitutive BACH1 binding sites before and after 100 μM heme treatment in BMDMs (2-kb windows centered on peak summits).

(B) Boxplots of normalized BACH1 coverage (RPKM) across reduced, constitutive, and gained regions in control and heme-treated BMDMs.

(C) Motif distribution heatmaps showing significantly enriched TF binding motifs within 2-kb windows around the summit of reduced, constitutive, and gained BACH1 sites.

(D) Pie charts showing the proportion and number of reduced, constitutive, and gained BACH1 sites with significantly higher (red), lower (blue), or unchanged (orange) RNA polymerase II and HDAC1 coverage following heme treatment.

(legend continued on next page)

directly correlated with transcriptional activity at proximal and distal regulatory regions.

To investigate the underlying mechanism, we tested whether BACH1 influences recruitment of HDAC1, a known BACH1-interacting co-repressor.[21] HDAC1 binding was decreased at both sites losing and gaining accessibility in Bach1−/− BMDMs (Figure 1H), suggesting a potential role for HDAC1-containing co-repressor complexes in BACH1-dependent regulation of chromatin accessibility in MFs. Given that HDAC1 and HDAC2 participate in multiple co-repressor complexes (including Sin3a, CoREST, RERE, NuRD, MIER, and MiDAC),[22] we asked whether BACH1 preferentially associates with a particular complex. Using RIME (ChIP-mass spectrometry [MS])[23] in untreated BMDMs, we found that BACH1 co-precipitated HDAC1 and HDAC2, together with core subunits of the NuRD complex, including CHD4 and MTA2, consistently across three biological replicates, along with other chromatin regulators (including SWI/SNF and INO80) (Figures 1I and S1I). Similarly, FLAG immunoprecipitation-MS in HCT116 cells expressing endogenous FLAG-tagged BACH1 identified nearly all NuRD subunits (MTA1, MTA2, CHD4, MBD3, RBBP4, and RBBP7), whereas SIN3A was the only additional HDAC1 complex component detected in both cellular systems (Figures 1J and 1K). Taken together, these observations suggested that BACH1's effect on chromatin openness correlated with association with the NuRD complex, the only HDAC1 complex with chromatin-remodeling activity (through its ATP-dependent chromodomain helicase subunit CHD4[24]).

Cognate heme-signaling elicits rapid redistribution of BACH1 binding to its local genomic neighborhood

We next asked whether the extensive BACH1 cistrome was static or dynamically remodeled upon signal-mediated MF activation. Because heme is a cognate ligand of BACH1[14] and promotes its destabilization,[17] we treated BMDMs with heme (1 h) and performed BACH1 ChIP-seq. As expected, heme stimulation resulted in a drastic reduction in BACH1 binding at 12,929 genomic sites (Figures 2A and 2B; reduced peaks), whereas 19,469 peaks remained unchanged (Figures 2A and 2B; constitutive peaks). Regions losing BACH1 binding were associated either with transcriptional repression or activation, accompanied by concordant changes in HDAC1 occupancy and chromatin accessibility (Figures 2D and 2E).

Unexpectedly, we also mapped new BACH1 peaks upon heme stimulation (13,344) (Figures 2A and 2B; gained peaks), which not only defied the established notion that increased heme levels rapidly degrade BACH1 but also suggested that BACH1 was actively relocating to new genomic sites. Consistent with this, nuclear BACH1 protein remained detectable after heme treatment (Figure S3A). *De novo* motif enrichment revealed enrichment of TRE motifs in all three clusters, while MARE motifs were enriched only in the reduced binding cluster (Figures 2C and S2B). Interestingly, EGR, ZNF263, and NF-κB motifs were specifically enriched in the gained binding cluster, suggesting that heme alters BACH1's binding selectivity in the genome. Gained BACH1 binding correlated with increased transcriptional activity, HDAC1 recruitment, and chromatin accessibility (Figures 2D, 2E, and S3B).

Strikingly, 96% of gained BACH1 sites (either *de novo* or induced) were located within 250 kb of a primary reduced peak (Figures 2F–2I), and multiple gained sites frequently clustered around a single reduced site (Figure S3D). Moreover, gained binding events were enriched at promoters (Figures 2G and S3E). Analysis of reduced-gained peak pairs within a 250-kb window demonstrated that most gained sites localized in close proximity to reduced sites, with 69.6% occurring within 50 kb (Figure 2J). Gained peaks were distributed both upstream and downstream of reduced peaks, indicating local redistribution rather than random reassignment across the genome.

Together, these findings demonstrated that heme induced rapid and spatially constrained redistribution of BACH1 binding within local genomic neighborhoods. Rather than complete chromatin disengagement, a substantial fraction of nuclear BACH1 remained associated with chromatin and relocated to nearby regulatory elements, including promoters and transcriptionally poised regions, accompanied by altered motif usage and transcriptional output.

BACH1 repression restricts 3D chromatin structure dynamics

The rapid heme-induced redistribution of BACH1 from distal regulatory elements to nearby promoters prompted us to examine whether these binding changes reflect alterations in local chromatin architecture. Consistent with this hypothesis, several proposed models of enhancer function[25–28] suggest that loading of TF complexes can be initiated from distal enhancers to promoters under gene-activation conditions, either through enhancer-promoter looping in 3D, stochastic enhancer scanning through hopping and sliding, or gradient diffusion of TF complexes to nearby genomic regions.

To quantify 3D enhancer connectivity, we performed capture Hi-C (cHi-C) in BMDMs using a custom probe panel targeting 9,127 high-occupancy BACH1-bound regions based on peak stratification (Figure S1D; Figure 3A). This approach enabled high-resolution mapping of chromatin interactions

(E) Boxplots of normalized ATAC-seq coverage (RPKM) across reduced, constitutive, and gained regions in control and heme-treated BMDMs. Statistical significance was determined by paired *t* test; $^{*}p \leq 0.05$, $^{**}p \leq 0.01$, $^{***}p \leq 0.001$, $^{****}p \leq 0.0001$. Whiskers indicate the 10th–90th percentile range and horizontal lines indicate the median.

(F) Boxplots showing normalized coverage of reduced versus *de novo* gained (left) and reduced versus induced gained (right) BACH1 peak pairs under control and heme-treated conditions. Statistical significance calculation as in (E).

(G) Stacked bar charts depicting the genomic distribution of reduced and *de novo* gained (top) and reduced and gained (bottom) BACH1 peaks.

(H) Heatmap of reduced BACH1 binding sites (left) and their closest *de novo* gained (n = 1,423) and induced gained (n = 11,442) sites before and after heme treatment. Peak pairs within a 250-kb window are ordered by relative distance.

(I) The proportion of reduced BACH1 peaks that can or cannot be associated with at least one gained or *de novo* gained peak within a ±250-kb window.

(J) Violin plot and bar charts showing the distance and number of gained BACH1 peaks relative to reduced sites.

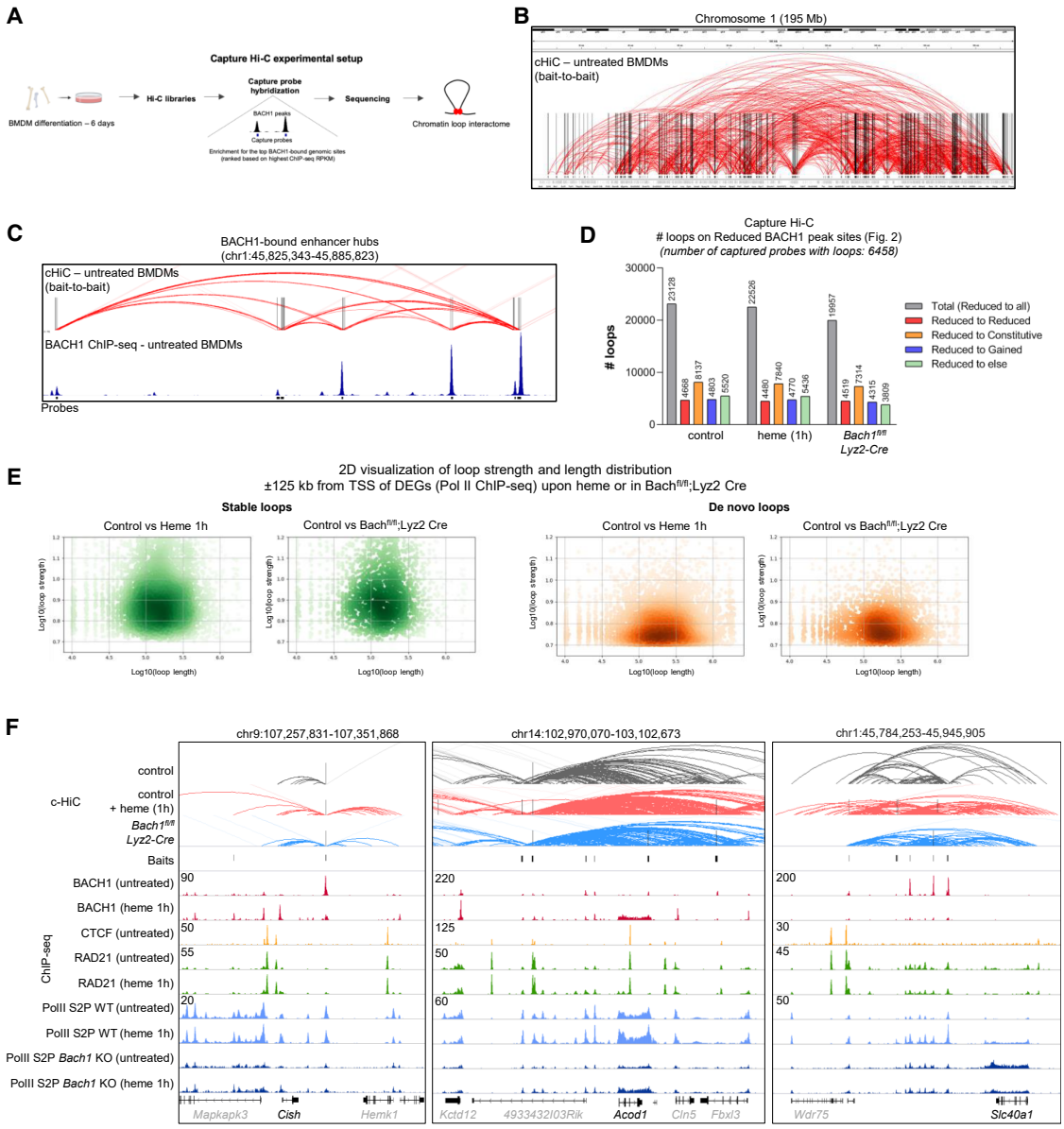


Figure 3. BACH1 repression restricts 3D chromatin structure dynamics

(A) Schematic of the capture Hi-C (cHi-C) workflow used to map chromatin interactions in BMDMs, using a custom capture probe panel targeting BACH1-bound enhancers.

(B) Genome-wide cHi-C loop arc diagram of chromosome 1 in untreated BMDMs, showing bait-to-bait interactions captured with the BACH1 enhancer probe panel.

(C) Zoomed-in view of a BACH1-bound enhancer hub at the *Slc40a1* locus, showing loop interactions in untreated BMDMs with the corresponding BACH1 ChIP-seq signal. Capture probe locations are indicated with black boxes.

(D) Bar graph showing the number of chromatin loops between repressed BACH1 peaks and other BACH1 peak classes (reduced, gained, and constitutive), as defined in Figure 2A.

(E) Scatterplots of loop strength versus loop length for stable (left) and *de novo* (right) loops comparing control vs. heme-treated BMDMs (1 h) and control vs. Bach1-deficient BMDMs. Loops within ±125 kb of differentially expressed genes (RNA Pol II ChIP-seq) are shown.

(F) Representative loci (*Cish*, *Slc40a1*, and *Acod1*) showing cHi-C interactions and BACH1, RAD21, RNA Pol II S2P, and CTCF ChIP-seq signals across conditions, categorized by response to heme or BACH1 loss.

genome-wide (an example on chromosome 1 is shown in Figure 3B). In untreated BMDMs, BACH1-bound regions formed robust and highly interconnected enhancer communities (bait-to-bait interactions) (Figure 3C). Notably, many regions that later exhibited reduced, constitutive, or gained BACH1 binding upon heme exposure (Figure 2A) were already spatially proximal in the resting state (Figure 3D). Reduced-gained peak pairs accounted for 20.8% (4,803/23,128) of all interactions involving reduced

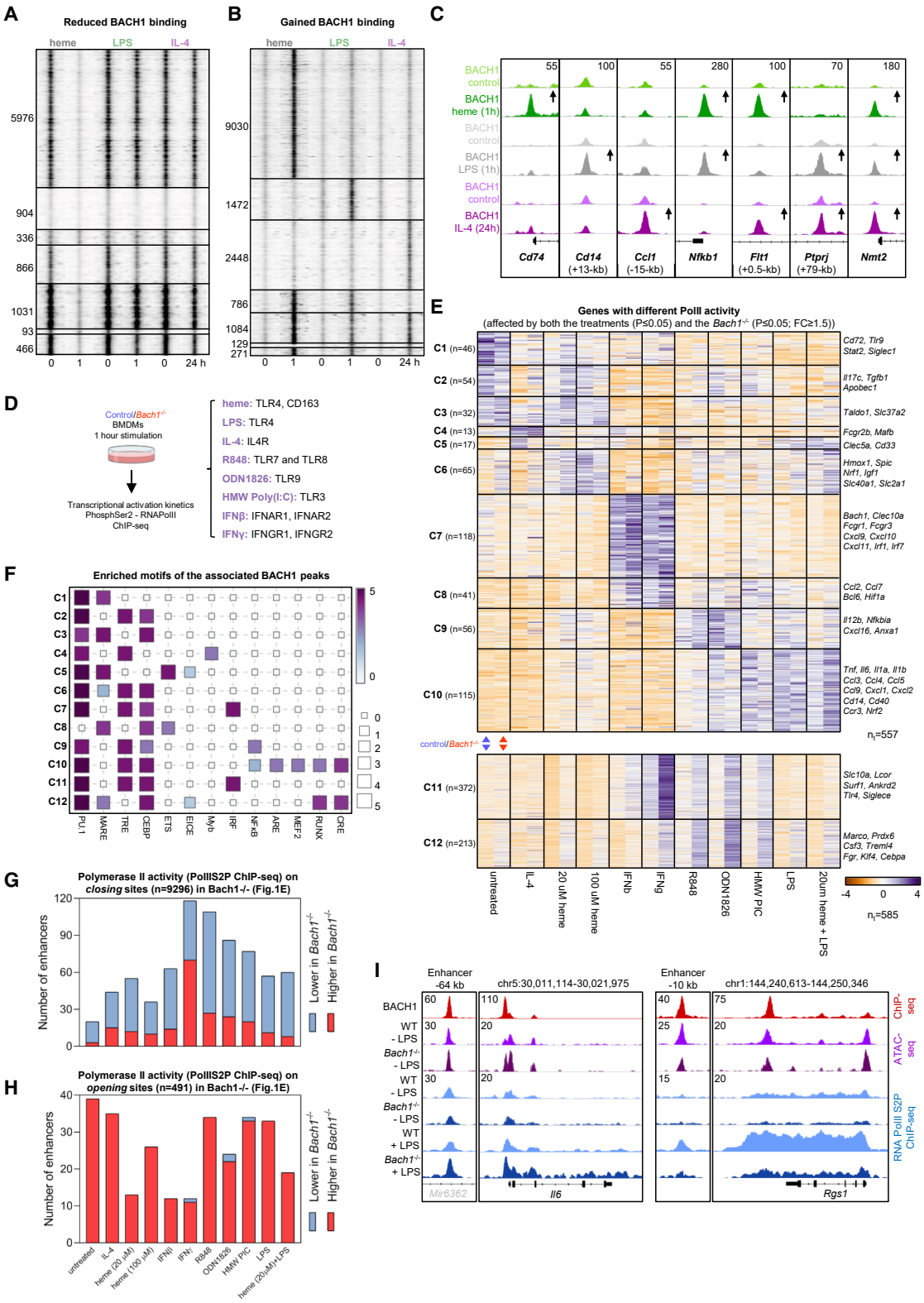


Figure 4. Non-cognate inflammatory signaling redistributes BACH1 binding and impacts early transcriptional response to diverse macrophage activation signals

(A and B) Clustered read distribution heatmaps showing significantly reduced (A) and gained (B) BACH1 binding sites ($p \leq 0.05$, FC ≥ 1.5) following heme, LPS, and/or IL-4 treatment.

(legend continued on next page)

regions (6,458 probes with detected loops), indicating that a substantial fraction of redistributed sites resided within preformed chromatin loops. However, the overall number of reduced-gained interactions did not significantly change following heme treatment or BACH1 deletion, suggesting that most redistribution events were not strictly determined by preexisting 3D proximity.

To assess how chromatin architecture changed in response to heme or BACH1 depletion, we performed cHi-C after 1 h heme stimulation and in myeloid-specific *Bach1*-deficient MFs (*Bach1*$^{fl/fl}$ Lyz2-Cre) (Figures S2D–S2G). Focusing on differentially transcribed genes (based on Pol II ChIP-seq within ±125 kb of the transcription start site [TSS]), we observed that newly formed loops displayed reduced interaction strength and increased loop length in both conditions (Figure 3E). Two-dimensional visualization of loop strength versus length revealed a coordinated shift toward weaker and longer-range interactions around regulated genes (Figure 3E), consistent with previous reports[28]. For example, the *Slc40a1* and *Acod1* loci (chromosomes 1 and 14, respectively) demonstrated that reduced-gained BACH1-bound region pairs could occur in untreated BMDMs and were further induced upon heme treatment (*Acod1*) or upon deletion of BACH1 (*Slc40a1*) (Figure 3F). In contrast, new heme- and BACH1-dependent loops at the *Cish* locus (chromosome 9) could occur without detectable transcriptional changes (Figure 3F).

We further examined the *Acod1* locus as a model of coordinated TF redistribution and chromatin structure dynamics. We identified a reduced BACH1 peak with neighboring gained peaks at nearby promoters upon heme treatment, as well as occupancy throughout the transcribed gene body, in a pattern resembling elongating RNA Pol occupancy (Figure 3F, right panel). This relocalization could override observed CTCF binding. This pattern prompted us to explore whether chromatin sliding mechanisms, such as transcription- and/or cohesin-mediated loop extrusion, could explain BACH1 relocalization. Using the LoopSage 3D-simulation pipeline,[29] we found that, in untreated conditions, a BACH1-bound enhancer located ~40 kb downstream of the *Acod1* TSS behaved as a potential boundary element separating the locus into two topological domains (Figure S4, upper panel). Upon heme treatment or BACH1 deletion, these domains merged into a single expanded interaction domain (Figure S4, central and bottom panels), consistent with reduced boundary constraint. Collectively, these findings supported a model in which BACH1 not only represses enhancer activity but also contributes to local chromatin organization, restricting enhancer-promoter interactions and constraining 3D chromatin dynamics in MFs.

Non-cognate inflammatory signaling redistributes BACH1 binding and impacts early transcriptional response to diverse MF activation signals

We next asked whether BACH1 chromatin binding was dynamically regulated by non-cognate inflammatory signals. WT BMDMs were stimulated with lipopolysaccharide (LPS) or interleukin (IL)-4 to model inflammatory and alternative activation states,[30] and BACH1 occupancy was profiled by ChIP-seq. Similar to heme stimulation, both LPS and IL-4 induced loss of BACH1 binding at primary sites (reduced peaks) and the appearance of gained binding sites (Figures 4A–C). Although a subset of affected regions was shared across heme, LPS, and IL-4 stimulation, each signal also induced unique sets of reduced and gained binding events, indicating signal-specific rewiring of the BACH1 cistrome.

To determine whether BACH1 modulates transcriptional responses to diverse stimuli, we profiled elongation-associated RNA Pol II (Ser2P) occupancy in control and Bach1−/− BMDMs following short-term (1 h) stimulation with eight activation signals: heme, LPS, IL-4, R848, ODN1826, polyI:C, interferon β (IFN-β), and IFN-γ (Figures 4D and S5A–S5B). Across all treatments, 2,350 genes displayed differential RNA Pol II occupancy in wild-type (WT) BMDMs. Of these, 557 genes (23.7%) were differentially expressed in Bach1−/− MFs ($p \leq 0.05$; FC ≥ 1.5) (Figures S5C–S5E). In addition, 585 genes were differentially expressed exclusively in Bach1−/− BMDMs without detectable Pol II changes in WT cells, suggesting that BACH1 deletion lowered activation thresholds and sensitized MFs to inflammatory cues. Clustering of RNA Pol II occupancy patterns revealed signal-specific transcriptional modules (Figure 4E). For example, distinct clusters were enriched for IL-4-, heme-, IFN-, and Toll-like receptor (TLR)-ligand-responsive genes. Two additional clusters contained the 585 Bach1−/−-specific genes, including genes induced only upon stimulation in the absence of BACH1 and genes exhibiting *de novo* elongation-associated RNA Pol II occupancy even in unstimulated Bach1−/− MFs. These findings indicated that BACH1 constrained early transcriptional responses in a signal-dependent manner.

Given the signal specificity of BACH1-dependent transcriptional effects, we next examined whether BACH1 cooperates with stimulus-specific TFs. We analyzed motif enrichment in BACH1-bound enhancers located within ±100 kb of genes exhibiting altered RNA Pol II occupancy (Figures 4F and S5F). In addition to enrichment of canonical myeloid motifs (PU.1 and CEBP) and BACH1 motifs (MARE and TRE), signal-specific motifs were detected in defined clusters. IRF motifs were enriched near IFN-responsive genes, whereas NF-κB motifs were enriched near TLR ligand-responsive genes (Figures 4F and S5F), consistent with context-dependent regulation. Importantly,

(C) Integrative Genomics Viewer (IGV) tracks of BACH1 ChIP-seq coverage in control, heme-, LPS-, and IL-4-treated BMDMs at representative BACH1 binding sites from (A) and (B); interval scales and distances to the nearest TSS are indicated.
(D) Experimental design for stimulation of WT and Bach1-deficient BMDMs and RNA Pol II S2P ChIP-seq.
(E) Row-normalized, *k*-means-clustered (C1–C10) heatmap of gene promoters showing significantly altered RNA Pol II activity in response to multiple treatments in control BMDMs ($p \leq 0.05$) and also affected by *Bach1* deletion ($p \leq 0.05$, FC ≥ 1.5). Lower panels (C11 and C12) show promoters differing between control and Bach1$^{-/-}$ BMDMs.
(F) Proportional heatmap showing enriched motif frequencies (normalized to element number) across clusters C1–C12 defined in (E).
(G–I) Differential RNA Pol II activity (Pol II S2P ChIP-seq) upon activation signals at distal elements with increased or decreased chromatin accessibility in untreated *Bach1*-deficient BMDMs (from Figure 1E); representative loci are shown in (I).

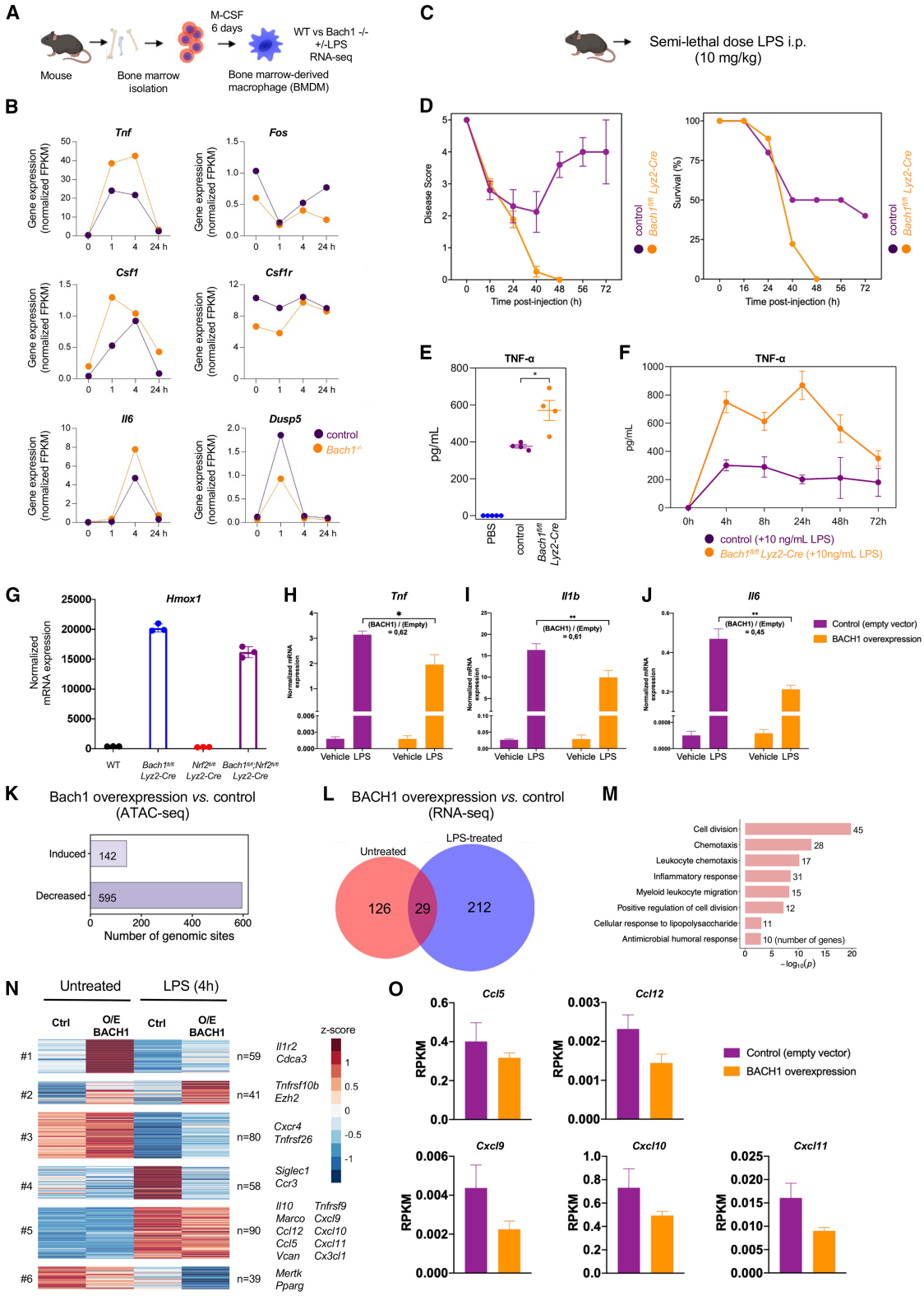


Figure 5. BACH1 modulates the inflammatory response kinetics *in vitro* and *in vivo*

(A and B) Experimental design and (B) examples of up- and downregulated genes in control and Bach1$^{-/-}$ BMDMs treated with LPS for 0, 1, 4, and/or 24 h. (C and D) Experimental design and (D) disease score and survival of control and *Bach1*$^{fl/fl}$*Lyz2-Cre* mice following intraperitoneal (i.p.) LPS injection. Data show mean survival percentages from five to eight mice per group; error bars indicate ± SD.

(legend continued on next page)

changes in transcriptional activity upon stimulation correlated with baseline alterations in chromatin accessibility observed in Bach1−/− BMDMs (Figures 4G–4I), indicating that early BACH1-dependent chromatin regulation shapes latent transcriptional programs.

Together, these data demonstrated that non-cognate inflammatory signals dynamically redistributed BACH1 binding and that BACH1 restrained early transcriptional activation programs across diverse MF stimuli.

BACH1 modulates the inflammatory response kinetics *in vitro* and *in vivo*

To determine whether BACH1-dependent chromatin and transcriptional effects translated into altered inflammatory responses, we performed RNA sequencing (RNA-seq) in WT and Bach1−/− BMDMs under basal conditions and following LPS stimulation (Figure 5A). BACH1 deletion resulted in dysregulated expression of multiple inflammatory genes upon LPS challenge, including *Tnf*, *Il1a*, *Il6*, *Il12a*, and *Tnfsf4* (Figures 5B and S6), indicating that BACH1 constrained early inflammatory transcriptional programs *in vitro*.

We next assessed the *in vivo* relevance of these findings using an LPS-induced endotoxemia model in myeloid-specific *Bach1*-deficient mice (*Bach1*$^{fl/fl}$ Lyz2-Cre) (Figure 5C). Mice were injected intraperitoneally with a titrated semi-lethal (LD50) dose of LPS. *Bach1*$^{fl/fl}$ Lyz2-Cre mice exhibited accelerated clinical deterioration compared with control littermates within 24 h (Figure 5D). By 48 h, all *Bach1*$^{fl/fl}$ Lyz2-Cre mice (n = 10) had succumbed, whereas approximately 50% of control mice survived and recovered (Figure 5D), indicating increased susceptibility to systemic inflammatory challenge in the absence of myeloid BACH1. Given the dysregulation of *Tnf* expression observed *in vitro* and its known functional role in septic shock and sepsis mortality,[31] we measured plasma tumor necrosis factor α (TNF-α) protein levels following LPS stimulation. TNF-α was significantly elevated in *Bach1*$^{fl/fl}$ Lyz2-Cre mice 4 h post intraperitoneal (i.p.) LPS injection and in Bach1−/− BMDMs *in vitro* (Figures 5E and 5F). Together, these findings demonstrated that myeloid BACH1 restrained inflammatory gene expression and protected against excessive systemic inflammatory responses *in vivo*.

BACH1 is sufficient to modulate chromatin accessibility in MFs

Our loss-of-function analyses indicated that BACH1 profoundly shapes chromatin accessibility and transcriptional responses in MFs. Because NRF2 is a known transcriptional activator that can replace BACH1 at shared genomic sites,[14] we examined whether NRF2 activity accounts for the transcriptional changes observed upon BACH1 deletion. We focused on *Hmox1*, a prototypical BACH1 and NRF2 target gene, and generated myeloid-specific *Nrf2*-deficient mice (*Nrf2*$^{fl/fl}$; LysM-Cre) as well as double-deficient mice lacking both BACH1 and NRF2 in myeloid cells (Bach1$^{fl/fl}$; *Nrf2*$^{fl/fl}$ Lyz2-Cre mice) (Figure S7A). Bach1$^{fl/fl}$ Lyz2-Cre BMDMs displayed constitutive upregulation of *Hmox1*, which remained largely elevated in Bach1$^{fl/fl}$; *Nrf2*$^{fl/fl}$ Lyz2-Cre MFs (Figure 5G). Similar trends were observed for additional shared targets (Figure S7B). Importantly, these data supported the hypothesis that BACH1 is not a passive placeholder but an active repressor in MFs.

To determine whether BACH1 is sufficient to modulate chromatin accessibility and transcription, we performed overexpression experiments by lentiviral transduction of primary WT BMDMs with full-length murine BACH1 (Figure S7C). Although transduction efficiency was limited to ∼40% (Figure S7D), BACH1 expression increased approximately 3-fold, resulting in further repression of established BACH1 targets *Hmox1* and *Spic* by 18% and 16%, respectively (Figure S7E). Upon LPS stimulation, BACH1 overexpression significantly reduced the magnitude of induction of inflammatory genes, including *Tnf*, *Il1b*, and *Il6*, without affecting their basal expression (Figures 5H–5J). ATAC-seq under basal conditions revealed that 3-fold BACH1 overexpression increased chromatin accessibility at 142 sites and decreased accessibility at 595 sites (Figures 5K and S7F), suggesting that the primary effect of BACH1 overexpression was to promote chromatin compaction. RNA-seq analysis under basal conditions and following LPS stimulation demonstrated largely distinct sets of genes regulated by BACH1 overexpression in the two conditions (Figure 5L), suggesting that a substantial component of BACH1 repression became apparent only upon activation. Pathway enrichment analysis identified processes relevant to MF function, including chemotaxis, migration, cell division, and LPS responses (Figure 5M). Clustering of gene expression changes revealed distinct kinetic patterns (Figure 5N). For example, certain genes were induced selectively at baseline (e.g., *Il1r2* and *Cxcr4*), others were induced both at baseline and upon LPS (e.g., *Tnfrsf10b* and *Ezh2*), whereas multiple immunomodulatory genes exhibited reduced induction upon LPS in the presence of excess BACH1 (e.g., *Siglec1*, *Il10*, and *Cxcl9–11*) (Figure 5O). A separate cluster comprised genes whose expression was reduced in both basal and stimulated conditions (e.g., *Mertk* and *Pparg*). Collectively, these overexpression experiments complemented the loss-of-function analyses and demonstrated that BACH1 is sufficient to modulate chromatin accessibility and constrain transcriptional activation programs in MFs, consistent with an active pioneer repressive role.

(E and F) ELISA measurements of serum TNF-α levels in control and *Bach1*$^{fl/fl}$*Lyz2-Cre* mice 4 h after i.p. LPS injection (E), and TNF-α levels in culture media from LPS-stimulated control and *Bach1*$^{fl/fl}$*Lyz2-Cre* BMDMs (F). Scatterplots show mean values from five to eight mice per group; error bars indicate ± SD. *p < 0.05.
(G) Quantitative reverse-transcription PCR (RT-qPCR) analysis of Hmox1 expression in control, *Bach1*, *Nrf2*, and double-deficient BMDMs (n = 3).
(H–J) RT-qPCR analysis of *Tnfa*, *Il1b*, and *Il6* expression following LPS stimulation in WT BMDMs transduced with a BACH1-overexpressing lentiviral vector (n = 3). Bar graphs present the mean ± SD of the biological replicates (*p < 0.05, **p < 0.01, and ***p < 0.001).
(K) Number of genomic regions with altered chromatin accessibility (ATAC-seq) in WT BMDMs transduced with a BACH1-overexpressing lentiviral vector (n = 2).
(L–N) (L) Number of differentially expressed genes (DEGs) (RNA-seq), (M) pathway analysis (GO biological process), and (N) k-means clustering in vehicle- and LPS-treated lentiviral-transduced WT BMDMs, with a plasmid vector overexpressing BACH1 (n = 3).
(O) RPKM levels of selected genes (*Ccl5*, *Ccl12*, *CXCL9*, *Cxcl10*, and *Cxcl11*) in LPS-treated lentiviral-transduced of WT BMDMs, with a plasmid vector overexpressing BACH1 (n = 3).

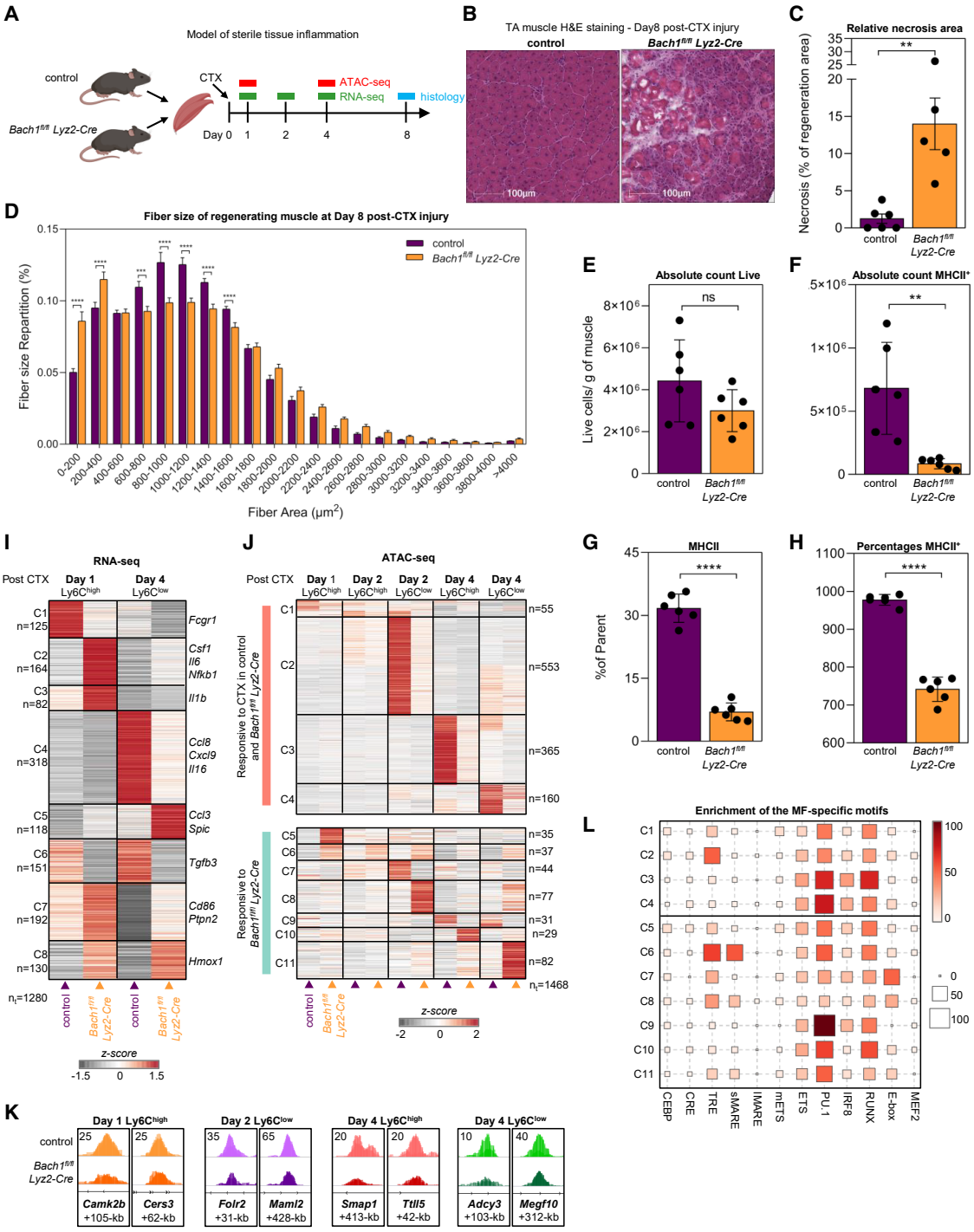


Figure 6. BACH1 is indispensable for enhancer activation during MF adaptation in sterile regenerative inflammation

(A) Schematic of the CTX-induced muscle inflammation model in control and *Bach1*$^{fl/fl}$*Lyz2-Cre* mice.

(B) Representative H&E-stained tibialis anterior (TA) muscle sections from control and *Bach1*$^{fl/fl}$*Lyz2-Cre* mice at day 8 post-CTX injury; scale bars, 100 µm.

(C) Relative necrotic area within regenerating muscle at day 8 post-CTX injury in control and *Bach1*$^{fl/fl}$*Lyz2-Cre* mice. Bars show mean values from 5–6 animals per group; error bars indicate ± SD.

(D) Fiber size distribution and average cross-sectional area (CSA) of regenerating muscle fibers at day 8 post-CTX injury in control and *Bach1*$^{fl/fl}$*Lyz2-Cre* mice (n = 6 per group; ± SD).

(E) Flow cytometry analysis of live cells per gram of TA tissue at day 8 post-CTX injury. Bars show mean values normalized to the necrotic area from 5–6 animals per group (± SD).

(F) Flow cytometry analysis of MHCII$^+$ cells per gram TA tissue at day 8 post-CTX injury in control and *Bach1*$^{fl/fl}$*Lyz2-Cre* mice (n = 5–6; ± SD).

(legend continued on next page)

BACH1 is indispensable for enhancer activation during MF adaptation in sterile regenerative inflammation

To assess the physiological relevance of myeloid BACH1 *in vivo*, we employed the cardiotoxin (CTX)-induced muscle injury model,[32] which elicits a sterile inflammatory response followed by MF-driven tissue regeneration (Figure 6A).[33] Histological analysis at day 8 post-injury revealed persistent necrotic fibers and an aberrant muscle fiber size distribution in *Bach1*$^{fl/fl}$ *Lyz2-Cre* mice compared with controls (Figures 6B–6D), consistent with defective regeneration. Total immune cell infiltration at day 4 was comparable between genotypes (Figure 6E); however, infiltrating monocytes in *Bach1*$^{fl/fl}$ *Lyz2-Cre* mice failed to upregulate MHCII (Figures 6F–6H and S8A), a marker associated with MF maturation and resolution-phase transitions.[34] These findings suggested impaired inflammatory-to-regenerative MF progression in the absence of *Bach1*. This prompted us to examine whether myeloid BACH1 established coherent, broad, functionally relevant gene expression programs during the early and late effector phases of MFs in regeneration. To this end, we profiled by bulk RNA-seq fluorescence-activated cell sorting (FACS)-purified populations of inflammatory (Ly6C^{high}) and regenerative (Ly6C^{low}) MFs from days 1 and 4 post-CTX injured muscles from control and *Bach1*$^{fl/fl}$ *Lyz2-Cre* mice. We identified 1,280 genes in total that were differentially expressed, which could be grouped in 8 clusters (Figures 6L, S8B, and S8C). Clusters 1, 4, and 6 contained genes that could not be induced to control levels in the absence of *Bach1*, either in early inflammatory MFs (C1; *Fcgr1*), or in late regenerative MFs (C4; *Ccl8, Cxcl9, Il16*), or in both (C6; *Tgfb3*), suggesting that BACH1 was indispensable for reaching their activation optimum. In contrast, clusters 2, 3, 5, and 7 contained genes with higher gene expression amplitude in early inflammatory MFs (C2; *Csf1, Il6, Nfkb1*, C3; *Il1b*), or in late regenerative MFs (C5; *Ccl3, Spic*) or in both (C7; *Cd86, Ptpn2*), whereas cluster 8 (*Spic*) contained genes significantly upregulated only in the absence of *Bach1* and not in the control, indicative of repressive activity of BACH1 on these 5 gene clusters. Interestingly, clusters 2 and 7 contained genes that were active only at day 1 in control samples, but their expression was still sustained on day 4 in *Bach1*$^{fl/fl}$ *Lyz2-Cre* mice, suggesting that *Bach1* deletion resulted in a defective shift from pro-inflammatory to anti-inflammatory gene programs and sequential cellular state transitions.

Due to the fact that transcriptional regulation is closely linked to chromatin accessibility, we next performed ATAC-seq on FACS-purified inflammatory and regenerative MFs isolated at days 1, 2, and 4 post-CTX (Figure 6J). We identified 1,468 genomic regions with differential accessibility in *Bach1*-deficient MFs (Figure S8D). Of these, 1,133 injury-responsive regulatory sites (clusters 1–4) required BACH1 for chromatin opening and were significantly less accessible in *Bach1*$^{fl/fl}$ *Lyz2-Cre* mice, particularly at days 2 and 4 post-injury (Figure 6J, upper panel; 6K; and S8E). In contrast, 335 regions (clusters 5–11) that were not injury responsive in controls displayed aberrant gains or losses of accessibility in the absence of BACH1 (Figure 6J, lower panel). Motif analysis revealed enrichment of MF lineage TF motifs (PU.1, IRF, RUNX, and ETS) across clusters. TRE/AP-1 motifs were broadly enriched, whereas canonical MARE motifs were selectively enriched in defined clusters (Figure 6L), consistent with direct BACH1 involvement at a subset of regulatory elements. Together, these data demonstrated that BACH1 was required for proper enhancer activation and temporal transcriptional reprogramming during MF-mediated tissue regeneration, coordinating both chromatin accessibility and gene expression programs necessary for effective resolution of sterile inflammation.

BACH1 is required for MF fitness in a distinct set of tissue niches *in vivo*

Given the broad effects of BACH1 on chromatin accessibility and inflammatory gene programs, we next examined whether BACH1 influences MF fitness within tissue microenvironments. We generated competitive bone marrow (BM) chimeras by transferring a 1:1 mixture of WT (CD45.1) and Bach1$^{-/-}$ (CD45.2) BM cells into lethally irradiated recipients (Figure 7A). Donor-derived cells contributed equally to monocytes and BM MFs, as well as circulating monocytes in blood, spleen, and liver (Figures 7A, S9, and S10). In contrast, differentiated tissue-resident MFs in the spleen, liver, peritoneum, and lung were predominantly WT derived, with lung alveolar MFs (AMs) being almost exclusively of WT origin (Figure 7A). Importantly, Bach1$^{-/-}$ BM cells efficiently repopulated tissues when transferred alone (Figure S9), indicating that BACH1 was dispensable for ontogeny but was required for competitive fitness and tissue adaptation.

To determine whether this disadvantage was cell intrinsic and myeloid restricted, we generated similar competitive chimeras using *Bach1*$^{fl/fl}$ *Lyz2-Cre* (CD45.2) BM mixed with WT (CD45.1) BM (Figure 7B). Again, a 1:1 mixture revealed a competitive deficit of *Bach1*-deficient MFs in the peritoneum and lung, whereas the BM monocyte contribution remained equivalent. Increasing the proportion of *Bach1*-deficient BM (1:3 and 1:20 ratios) partially restored representation in tissues (Figure 7B), confirming a competitive rather than developmental defect. Because AMs showed the most pronounced fitness defect, we examined expression of the AM maturation marker *SiglecF*. In all competitive BM ratios (1:1, 1:3, and 1:20), *SiglecF* expression was significantly reduced in *Bach1*-deficient AMs (Figure 7C). Similar reductions were observed in steady-state lungs from mice with early (Vav-Cre) or late (LysM-Cre) BACH1 deletion

(G) Median fluorescence intensity (MFI) of MHCII in muscle macrophages (MFs) at day 8 post-CTX injury; mean values from 5–6 animals per group (± SD).
(H) Frequency of MHCII^{+} MFs at day 8 post-CTX injury in control and *Bach1*$^{fl/fl}$*Lyz2-Cre* mice (n = 5–6; ± SD).
(I) Row-normalized heatmap showing differentially expressed genes ($p \leq 0.05$, FC ≥ 1.5) in day 1 Ly6C^{high} and day 4 Ly6C^{low} populations following CTX injury in control and *Bach1*$^{fl/fl}$*Lyz2-Cre* TA muscles (n = 3).
(J) Row-normalized heatmap of differentially accessible chromatin regions ($p \leq 0.05$, FC ≥ 1.5) associated with CTX and/or Bach1 deletion in Ly6C^{high} and Ly6C^{low} populations at days 1, 2, and 4 post-CTX injury (n = 2).
(K) IGV tracks of ATAC-seq coverage at representative differentially accessible regions after CTX injury; replicates are overlaid, and distances to the nearest TSS are indicated.
(L) Proportional heatmap showing MF-specific motif enrichment (normalized to the element number) across clusters C1–C11 defined in (J) (sMARE, small MARE; lMARE, large MARE; mETS, methylatable ETS).

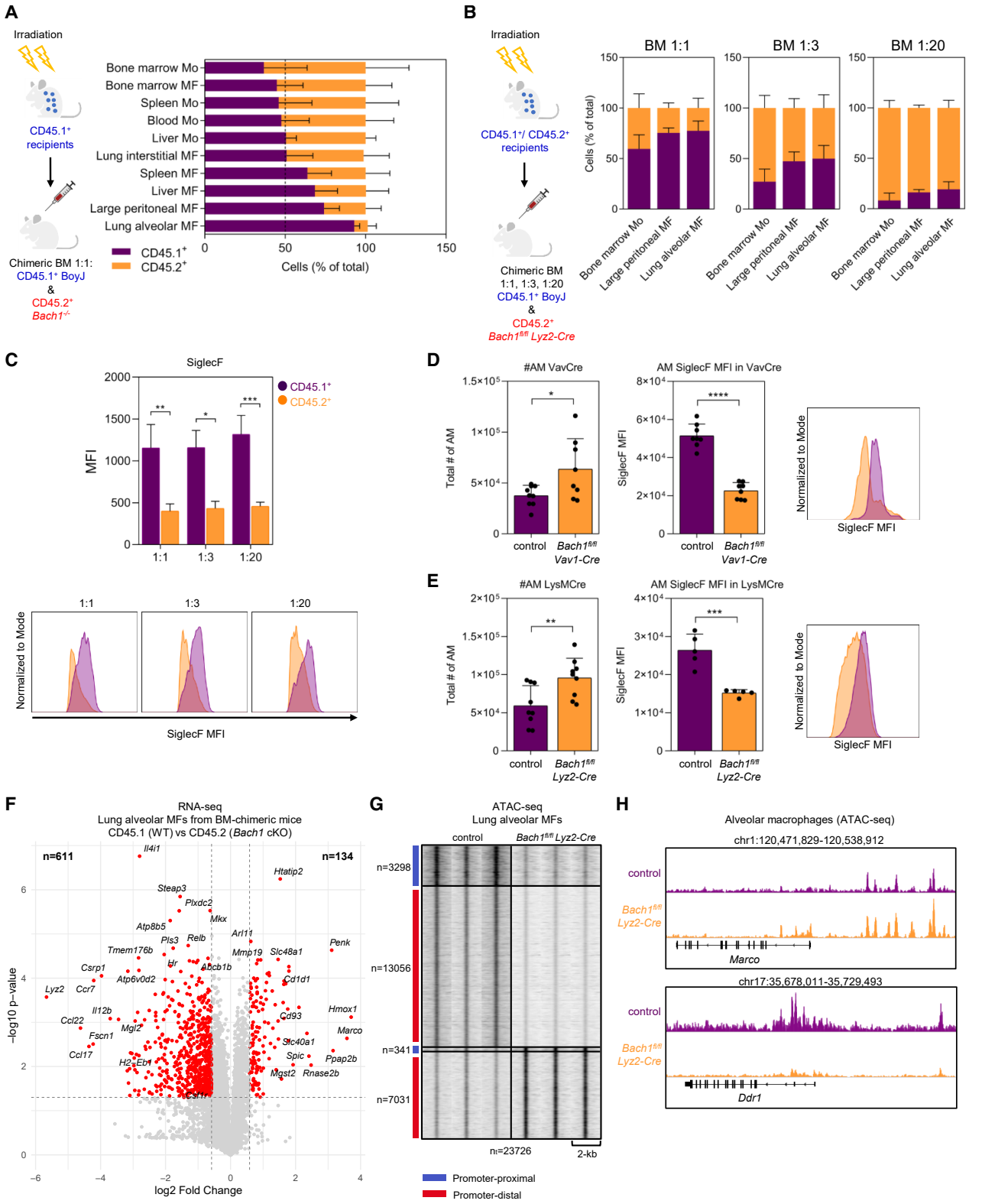


Figure 7. BACH1 is required for MF fitness in a distinct set of tissue niches *in vivo*

(A) Flow cytometry analysis showing the ratio of tissue-derived CD45.1$^+$ Bach1$^{+/+}$ and CD45.2$^+$ Bach1$^{-/-}$ macrophages (MFs) and monocytes in BACH1 mixed chimeric mice. Bar plots show frequencies of CD45.1$^+$ and CD45.2$^+$ cells in the indicated populations from lethally irradiated recipients ≥8 weeks after transfer of a 1:1 mixture of donor BM cells. Eight mice per group; error bars indicate ± SD.

(legend continued on next page)

(Figures 7D and 7E). Although total AM numbers increased in these models, *SiglecF* expression remained diminished, indicating impaired maturation despite the increase.

To define the molecular basis of this phenotype, we performed RNA-seq on WT and *Bach1*-deficient AMs isolated from competitive chimeras (CD45.1 WT versus CD45.2 *Bach1*$^{fl/fl}$ *Lyz2-Cre* AMs from the same lung). We identified 134 upregulated and 611 downregulated genes in *Bach1*-deficient AMs (Figure 7F). Downregulated genes included key regulators of AM identity and function (*SiglecF*, *Car4*, *Marco*, and *Pparg*), antigen presentation (*Ciita*, *H2-Aa*, *H2-Ab1*, *Cd74*, *Cd80*, and *Cd86*), lipid metabolism (*Lpcat1*), and differentiation or chemokine signaling (*Csf1r*, *Ccr7*, *Ccl17*, and *Ccl22*), indicating broad disruption of tissue-adaptive programs.

Consistent with these transcriptional alterations, ATAC-seq in WT and *Bach1*-deficient AMs demonstrated that BACH1 was required to maintain chromatin accessibility at 13,056 distal elements and 3,298 promoters, whereas its deletion resulted in increased accessibility at 7,031 distal elements and 341 promoters (Figures 7G and 7H). These findings mirrored the dual chromatin-regulatory role observed *in vitro* and underscored a critical requirement for BACH1 to sustain enhancer-accessibility programs necessary for MF maturation and fitness within tissue niches.

DISCUSSION

In this study, we investigated the role of the transcriptional repressor BACH1 in MF chromatin regulation and function. We found that BACH1 binds extensively to both open and closed chromatin regions, regulates chromatin accessibility, and dynamically redistributes in response to inflammatory stimulation. These changes were associated with altered enhancer-promoter interactions and transcriptional outputs. *In vivo*, myeloid BACH1 was required for MF polarization, adaptation in tissue niches, and organismal and tissue fitness during inflammatory and regenerative responses. Together, these findings suggest that BACH1-mediated pioneer repression, defined as the ability of a transcriptional repressor to engage chromatin, shape accessibility, and constrain transcriptional activation prior to stimulation, represents a regulatory layer governing MF plasticity and adaptation. There are several mechanistic and functional implications of these findings.

First, our data demonstrated that BACH1 exhibited pioneering activity across multiple biological systems, including naive BMDMs, dynamically adapting monocyte-derived MFs during sterile muscle regeneration, and lung AMs. In all contexts, BACH1 was required for chromatin opening at defined regulatory elements. Notably, during muscle regeneration, numerous injury-responsive sites failed to acquire accessibility in the absence of BACH1 throughout inflammatory-to-regenerative transitions, indicating that BACH1 was not merely modulating kinetics but was required for establishing enhancer competence at a subset of loci. Given its high expression in circulating monocytes,[19] BACH1 likely acts early in myeloid differentiation to commission regulatory regions that remain transcriptionally restrained until tissue-specific cues are encountered. These observations expand the prevailing view that pioneering activity is predominantly linked to transcriptional activation by LDTFs.[12,35] Instead, our findings support a model in which pioneer repression stabilizes enhancer landscapes in a poised but constrained state. Although recent studies have shown that classical PFs, such as FOXA and OCT4, can recruit remodelers to enforce repression,[36] our work extends this framework by identifying a canonical transcriptional repressor as a pioneer-like factor. Through association with chromatin-modifying complexes (e.g., HDAC/NuRD, SWI/SNF, and INO80) and modulation of chromatin accessibility, BACH1 enforces transcriptional repression while preserving the priming competence of regulatory elements. Thus, pioneer repression emerges as a regulatory strategy that safeguards transcriptional timing in highly plastic immune cells.

Second, we showed that BACH1 binding was extensive in naive MFs and became highly dynamic upon activation. In response to heme, BACH1 dissociated from a subset of enhancers while remaining bound at others. It also acquired new binding at nearby promoters and regulatory elements enriched for alternative motifs, such as NF-κB, EGR, and ZNF263. It remains unclear whether other TFs, through association with BACH1 or through their impact on chromatin, drive these new binding events. However, we found that newly induced BACH1 binding occurred in close proximity to primary binding sites and, in some cases, within pre-existing enhancer-enhancer or enhancer-promoter loops. This short-range relocation was accompanied by the formation of longer but weaker chromatin loops and altered transcriptional kinetics, consistent with a role for BACH1 in constraining enhancer-promoter interactions under resting conditions. Mechanistically, these dynamics align with models in which TFs undergo facilitated diffusion, sampling nearby chromatin regions through sliding or hopping rather than complete dissociation. An alternative explanation for BACH1's observed short-range redistribution is provided by the transcription factor activity gradient (TAG) model,[28] which proposes that TFs

(B) Ratios of CD45.1$^+$ Bach1$^{+/+}$ and CD45.2$^+$ Bach1$^{-/-}$ monocytes and tissue-resident MFs in the bone marrow, peritoneum, and lungs of BACH1 chimeric mice (n = 8; ± SD).
(C) Median fluorescence intensity (MFI) of Siglec-F in CD45.1$^+$ and CD45.2$^+$ alveolar macrophages (AMs) from the lungs of BACH1 chimeric mice. Bars show mean MFI values (n = 8; ± SD); histogram overlays show one representative mouse. *p < 0.05, **p < 0.01, ***p < 0.001.
(D) Flow cytometry analysis of total lung AM numbers and Siglec-F MFI in control and *Bach1*$^{fl/fl}$Vav1-Cre mice. Eight mice per group; error bars indicate ± SD. Representative histograms are shown. *p < 0.05, ****p < 0.0001.
(E) Flow cytometry analysis of total lung AM numbers and Siglec-F MFI in control and *Bach1*$^{fl/fl}$Lyz2-Cre mice (n = 5–10; ± SD). Representative histograms are shown. **p < 0.01, ***p < 0.001.
(F) Volcano plot showing differentially expressed genes ($p \leq 0.05$, FC ≥ 1.5) between CD45.1$^+$ (WT) and CD45.2$^+$ (*Bach1*$^{fl/fl}$Lyz2-Cre) lung alveolar MFs from BM-chimeric mice (n = 3).
(G–I) Read distribution heatmap and representative loci showing significant ATAC-seq signal changes between control and *Bach1*$^{fl/fl}$*Lyz2-Cre* lung alveolar MFs.

undergo dynamic, distance-dependent diffusion rather than being strictly tethered by chromatin loops. In this model, BACH1 posttranslational modifications in response to heme may alter its DNA-binding specificity and affinity,[17,18] shifting interactions from high-affinity enhancer motifs to weaker interactions at nearby promoters. BACH1 binding was also altered upon LPS and IL-4 stimulation, suggesting that these dynamics are not uniquely heme-dependent and that diverse inflammatory signals may modulate BACH1 localization in a context-specific manner. It is tempting to consider that newly acquired BACH1 binding establishes an adapted baseline during inflammatory resolution, with potential implications for trained immunity and transcriptional memory.

Third, we found that BACH1 was crucial for myeloid responses, plasticity, and adaptation. BACH1's regulation of chromatin accessibility underpins (1) a dependence of tissue-resident MF programs on BACH1 at baseline, reflected in reduced fitness of BACH1-deficient MFs in specific niches; (2) broad, stimulus-specific control of inflammatory gene expression across multiple activation pathways; and (3) a requirement for BACH1 in efficient polarization and resolution of inflammation and in preserving organismal fitness during systemic inflammatory stress. Competitive BM chimeras showed that BACH1 integrates local cues to sustain MF fitness *in situ*, particularly in the lung alveoli, peritoneum, and spleen. Even in the spleen, where heme metabolism genes (*Hmox1*, *Fth1*, and *Spic*) were significantly upregulated in BACH1-deficient MFs, these cells did not gain a competitive advantage, suggesting that BACH1 regulates a broader adaptation module beyond heme metabolism. At the transcriptional level, Pol II-based analyses demonstrated that BACH1 deletion caused premature, sustained, or exaggerated induction and repression of inflammatory genes across signals, indicating that BACH1 sets activation thresholds rather than acting as a simple on/off switch. *In vivo*, myeloid-specific *Bach1* deletion compromised the resolution of local regenerative inflammation and increased sensitivity to systemic LPS, with lethal TNF-dominated responses. Notably, BACH1 did not affect myeloid ontogeny or tissue infiltration, underscoring its role as a quantitative regulator of gene expression.

Our study positions BACH1 as a regulator of MF plasticity and adaptation. The proposed mechanism highlights a role for pioneer repression in shaping enhancer landscapes and ensuring appropriate transcriptional responses to inflammatory and homeostatic signals. Future work should explore whether similar mechanisms operate in other cell types, including adaptive immune cells, epithelial cells, and fibroblasts. In addition, modulation of BACH1 activity, for example, through heme-mimicking compounds, may represent a potential strategy for targeting inflammatory diseases.

Limitations of the study

Our designation of BACH1 as a pioneer repressor relies on an operational definition based on genome-wide BACH1 occupancy profiling, including binding to closed chromatin, regulation of chromatin accessibility, and transcriptional repression. Although we did not directly test nucleosome engagement by BACH1 in reconstituted biochemical systems, both loss-of-function and overexpression experiments, combined with signal-dependent removal through its physiological heme degron, support a direct role for BACH1 in shaping enhancer accessibility. Nevertheless, our data cannot fully distinguish whether BACH1 initiates chromatin opening at regulatory elements or contributes to the maintenance of accessible chromatin states once established. Finally, while our results support recruitment of NuRD-associated complexes as part of this mechanism, the precise contribution of individual NuRD components, such as its chromatin remodeling subunit CHD4, and other chromatin complexes to BACH1-dependent pioneer repression will require further investigation.

RESOURCE AVAILABILITY

Lead contact

Requests for reagents should be directed to and will be fulfilled by the lead contact, Laszlo Nagy (lnagy@jhmi.edu).

Materials availability

Requests for unique cell lines and mice generated in this study should be directed to the lead contact.

Data and code availability

The generated next-generation sequencing datasets are available in the Gene Expression Omnibus (GEO) repository under accession number GSE245651.

ACKNOWLEDGMENTS

The authors wish to acknowledge Attila Pap, Pal Boto, Szilard Poliska, Nadra Alzain, David Deak, Xiaoyan Wei, and Oksana Gonchar for their help in experiments. We also thank members of the Nagy laboratory for discussions and critical reading of the manuscript. P.T. was supported by a Marie Curie Intra-European Fellowship for Experienced Researchers (EU FP7/2007–2013) under the Initial Training Network NR-NET (grant agreement no. 606806). D.B. and G.N. were supported by Hungarian Academy fellowships (PD137902 and FK146945, respectively). K. Bene was supported by the Hungarian National Excellence Program (NTP-NFTO-21-B-0258), the fellowship program of the Hungarian Society for Immunology, and the scholarship program of the Rosztoczy Foundation (AZ, USA). N.C.-S. was supported by H2020 Marie Skłodowska-Curie Actions (grant number: 860034). D.P., S.K., K. Banecki, and Z.P.-T.'s research was funded by Warsaw University of Technology within the Excellence Initiative: Research University (IDUB) program and co-supported by the Polish National Science Center (2020/37/B/NZ2/03757). This work was funded by the NIH grants (AI185363, DK138430, and HL170426), the National Research, Development and Innovation Office in Hungary (K124298 and K147147), and the European Advanced infraStructure for Innovative Genomics grant – EASI (PID7865).

AUTHOR CONTRIBUTIONS

Conceptualization: P.T. and L.N. Investigation: P.T., K. Bene, N.C.-S., S.M.P., A.P., D.O., and T.C. Methodology: P.T., S.K., S.C., E.K.P., F.E., Z.M., G.S., and C.G.S. Formal analysis, data curation, and visualization: P.T., D.B., K. Bene, N.C.-S., Z.P.-T., K. Banecki, S.K., N.G., E.K.P., and G.N. Funding acquisition: L.N. Supervision: J.W.R.S., J.S.C., D.P., and L.N. Writing – original draft: P.T. Writing – review & editing: P.T., D.B., K. Bene, and L.N.

DECLARATION OF INTERESTS

The authors declare no competing interests.

DECLARATION OF GENERATIVE AI AND AI-ASSISTED TECHNOLOGIES IN THE WRITING PROCESS

The authors used ChatGPT 5.3 for minor rephrasing but reviewed and edited the article afterward. The authors take full responsibility for the content of the published article.

STAR★METHODS

Detailed methods are provided in the online version of this paper and include the following:

- KEY RESOURCES TABLE
- EXPERIMENTAL MODEL AND STUDY PARTICIPANT DETAILS
  - Mouse strains
  - Bone marrow-derived macrophage (BMDM) differentiation
  - Human colorectal carcinoma HCT116 cell line
- METHOD DETAILS
  - Stimulation of BMDMs
  - Real-time quantitative PCR for mRNA detection (qPCR)
  - RNA-seq
  - ATAC-seq
  - ChIP-seq
  - Immunoprecipitation coupled with Mass-Spectrometry (IP-MS)
  - Capture Hi-C
  - Cardiotoxin (CTX)-induced acute sterile muscle injury model
  - Bone marrow transplantation (BMT) and the generation of BM-chimeric mice
  - Tissue processing, flow cytometry, and fluorescence-activated cell sorting (FACS)
  - Intraperitoneal lipopolysaccharide (LPS)-induced sepsis model
  - Immunoblot
  - Enzyme-linked immunosorbent assay (ELISA)
- QUANTIFICATION AND STATISTICAL ANALYSIS
  - Statistical analysis
  - RNA-seq analysis
  - ATAC-seq analysis
  - Transcription factor ChIP-seq analysis
  - RNA Polymerase II ChIP-seq analysis
  - *De novo* motif enrichment analysis and motif remap
  - Visualization
  - Capture Hi-C analysis & Loop dynamics simulation

SUPPLEMENTAL INFORMATION

Supplemental information can be found online at https://doi.org/10.1016/j.immuni.2026.06.022.

Received: May 29, 2025
Revised: December 22, 2025
Accepted: June 20, 2026
Published: July 17, 2026

REFERENCES

1. Natoli, G., and Ostuni, R. (2019). Adaptation and memory in immune responses. Nat. Immunol. *20*, 783–792. https://doi.org/10.1038/s41590-019-0399-9.
2. Amit, I., Winter, D.R., and Jung, S. (2016). The role of the local environment and epigenetics in shaping macrophage identity and their effect on tissue homeostasis. Nat. Immunol. *17*, 18–25. https://doi.org/10.1038/ni.3325.
3. Okabe, Y., and Medzhitov, R. (2016). Tissue biology perspective on macrophages. Nat. Immunol. *17*, 9–17. https://doi.org/10.1038/ni.3320.
4. Ostuni, R., and Natoli, G. (2011). Transcriptional control of macrophage diversity and specialization. Eur. J. Immunol. *41*, 2486–2490. https://doi.org/10.1002/eji.201141706.
5. Okabe, Y., and Medzhitov, R. (2014). Tissue-specific signals control reversible program of localization and functional polarization of macrophages. Cell *157*, 832–844. https://doi.org/10.1016/j.cell.2014.04.016.
6. Schneider, C., Nobs, S.P., Kurrer, M., Rehrauer, H., Thiele, C., and Kopf, M. (2014). Induction of the nuclear receptor PPAR-gamma by the cytokine GM-CSF is critical for the differentiation of fetal monocytes into alveolar macrophages. Nat. Immunol. *15*, 1026–1037. https://doi.org/10.1038/ni.3005.
7. Kohyama, M., Ise, W., Edelson, B.T., Wilker, P.R., Hildner, K., Mejia, C., Frazier, W.A., Murphy, T.L., and Murphy, K.M. (2009). Role for Spi-C in the development of red pulp macrophages and splenic iron homeostasis. Nature *457*, 318–321. https://doi.org/10.1038/nature07472.
8. Gosselin, D., and Glass, C.K. (2014). Epigenomics of macrophages. Immunol. Rev. *262*, 96–112. https://doi.org/10.1111/imr.12213.
9. Heinz, S., Benner, C., Spann, N., Bertolino, E., Lin, Y.C., Laslo, P., Cheng, J.X., Murre, C., Singh, H., and Glass, C.K. (2010). Simple combinations of lineage-determining transcription factors prime cis-regulatory elements required for macrophage and B cell identities. Mol. Cell *38*, 576–589. https://doi.org/10.1016/j.molcel.2010.05.004.
10. Feng, A.C., Thomas, B.J., Purbey, P.K., de Melo, F.M., Liu, X., Daly, A.E., Sun, F., Lo, J.H.H., Cheng, L., Carey, M.F., et al. (2024). The transcription factor NF-κB orchestrates nucleosome remodeling during the primary response to toll-like receptor 4 signaling. Immunity *57*, 462–477.e9. https://doi.org/10.1016/j.immuni.2024.02.004.
11. Balsalobre, A., and Drouin, J. (2022). Pioneer factors as master regulators of the epigenome and cell fate. Nat. Rev. Mol. Cell Biol. *23*, 449–464. https://doi.org/10.1038/s41580-022-00464-z.
12. Katsuda, T., Sussman, J.H., Zaret, K.S., and Stanger, B.Z. (2024). The yin and yang of pioneer transcription factors: Dual roles in repression and activation. BioEssays *46*, e2400138. https://doi.org/10.1002/bies.202400138.
13. Nagy, G., Bojcsuk, D., Tzerpos, P., Cseh, T., and Nagy, L. (2024). Lineage-determining transcription factor-driven promoters regulate cell type-specific macrophage gene expression. Nucleic Acids Res. *52*, 4234–4256. https://doi.org/10.1093/nar/gkae088.
14. Igarashi, K., Kurosaki, T., and Roychoudhuri, R. (2017). BACH transcription factors in innate and adaptive immunity. Nat. Rev. Immunol. *17*, 437–450. https://doi.org/10.1038/nri.2017.26.
15. Ito, N., Watanabe-Matsui, M., Igarashi, K., and Murayama, K. (2009). Crystal structure of the Bach1 BTB domain and its regulation of homodimerization. Genes Cells *14*, 167–178. https://doi.org/10.1111/j.1365-2443.2008.01259.x.
16. Dohi, Y., Ikura, T., Hoshikawa, Y., Katoh, Y., Ota, K., Nakanome, A., Muto, A., Omura, S., Ohta, T., Ito, A., et al. (2008). Bach1 inhibits oxidative stress-induced cellular senescence by impeding p53 function on chromatin. Nat. Struct. Mol. Biol. *15*, 1246–1254. https://doi.org/10.1038/nsmb.1516.
17. Zenke-Kawasaki, Y., Dohi, Y., Katoh, Y., Ikura, T., Ikura, M., Asahara, T., Tokunaga, F., Iwai, K., and Igarashi, K. (2007). Heme induces ubiquitination and degradation of the transcription factor Bach1. Mol. Cell. Biol. *27*, 6962–6971. https://doi.org/10.1128/MCB.02415-06.
18. Haldar, M., Kohyama, M., So, A.Y.L., Kc, W., Wu, X., Briseño, C.G., Satpathy, A.T., Kretzer, N.M., Arase, H., Rajasekaran, N.S., et al. (2014). Heme-mediated SPI-C induction promotes monocyte differentiation into iron-recycling macrophages. Cell *156*, 1223–1234. https://doi.org/10.1016/j.cell.2014.01.069.
19. Gautier, E.L., Shay, T., Miller, J., Greter, M., Jakubzick, C., Ivanov, S., Helft, J., Chow, A., Elpek, K.G., Gordonov, S., et al. (2012). Gene-expression profiles and transcriptional regulatory pathways that underlie the identity and diversity of mouse tissue macrophages. Nat. Immunol. *13*, 1118–1128. https://doi.org/10.1038/ni.2419.
20. Ostuni, R., Piccolo, V., Barozzi, I., Polletti, S., Termanini, A., Bonifacio, S., Curina, A., Prosperini, E., Ghisletti, S., and Natoli, G. (2013). Latent enhancers activated by stimulation in differentiated cells. Cell *152*, 157–171. https://doi.org/10.1016/j.cell.2012.12.018.

21. Jiang, L., Jia, M., Wei, X., Guo, J., Hao, S., Mei, A., Zhi, X., Wang, X., Li, Q., Jin, J., et al. (2020). Bach1-induced suppression of angiogenesis is dependent on the BTB domain. EBiomedicine *51*, 102617. https://doi.org/10.1016/j.ebiom.2019.102617.

22. Asmamaw, M.D., He, A., Zhang, L.R., Liu, H.M., and Gao, Y. (2024). Histone deacetylase complexes: Structure, regulation and function. Biochim. Biophys. Acta Rev. Cancer *1879*, 189150. https://doi.org/10.1016/j.bbcan.2024.189150.

23. Mohammed, H., Taylor, C., Brown, G.D., Papachristou, E.K., Carroll, J.S., and D'Santos, C.S. (2016). Rapid immunoprecipitation mass spectrometry of endogenous proteins (RIME) for analysis of chromatin complexes. Nat. Protoc. *11*, 316–326. https://doi.org/10.1038/nprot.2016.020.

24. Farnung, L., Ochmann, M., and Cramer, P. (2020). Nucleosome-CHD4 chromatin remodeler structure maps human disease mutations. eLife *9*, e56178. https://doi.org/10.7554/eLife.56178.

25. Schoenfelder, S., and Fraser, P. (2019). Long-range enhancer-promoter contacts in gene expression control. Nat. Rev. Genet. *20*, 437–455. https://doi.org/10.1038/s41576-019-0128-0.

26. Vernimmen, D., and Bickmore, W.A. (2015). The Hierarchy of Transcriptional Activation: From Enhancer to Promoter. Trends Genet. *31*, 696–708. https://doi.org/10.1016/j.tig.2015.10.004.

27. Galouzis, C.C., and Furlong, E.E.M. (2022). Regulating specificity in enhancer-promoter communication. Curr. Opin. Cell Biol. *75*, 102065. https://doi.org/10.1016/j.ceb.2022.01.010.

28. Karr, J.P., Ferrie, J.J., Tjian, R., and Darzacq, X. (2022). The transcription factor activity gradient (TAG) model: contemplating a contact-independent mechanism for enhancer-promoter communication. Genes Dev. *36*, 7–16. https://doi.org/10.1101/gad.349160.121.

29. Korsak, S., and Plewczynski, D. (2024). LoopSage: An energy-based Monte Carlo approach for the loop extrusion modeling of chromatin. Methods *223*, 106–117. https://doi.org/10.1016/j.ymeth.2024.01.015.

30. Czimmerer, Z., Halasz, L., Daniel, B., Varga, Z., Bene, K., Domokos, A., Hoeksema, M., Shen, Z., Berger, W.K., Cseh, T., et al. (2022). The epigenetic state of IL-4-polarized macrophages enables inflammatory cistromic expansion and extended synergistic response to TLR ligands. Immunity *55*, 2006–2026.e2006. https://doi.org/10.1016/j.immuni.2022.10.004.

31. Korneev, K.V. (2019). Mouse Models of Sepsis and Septic Shock. Mol. Biol. (Mosk) *53*, 799–814. https://doi.org/10.1134/S0026898419050100.

32. Wang, Y., Lu, J., and Liu, Y. (2022). Skeletal Muscle Regeneration in Cardiotoxin-Induced Muscle Injury Models. Int. J. Mol. Sci. *23*, 13380. https://doi.org/10.3390/ijms232113380.

33. Patsalos, A., Tzerpos, P., Wei, X., and Nagy, L. (2021). Myeloid cell diversification during regenerative inflammation: Lessons from skeletal muscle. Semin. Cell Dev. Biol. *119*, 89–100. https://doi.org/10.1016/j.semcdb.2021.05.005.

34. Panduro, M., Benoist, C., and Mathis, D. (2018). T(reg) cells limit IFN-gamma production to control macrophage accrual and phenotype during skeletal muscle regeneration. Proc. Natl. Acad. Sci. USA *115*, E2585–E2593. https://doi.org/10.1073/pnas.1800618115.

35. Liu, Y., and Wade, P.A. (2024). Out with the old, in with the new: Pioneer transcription factors as activators and repressors of lineage specification genes. Mol. Cell *84*, 411–412. https://doi.org/10.1016/j.molcel.2023.12.031.

36. Matsui, S., Granitto, M., Buckley, M., Ludwig, K., Koigi, S., Shiley, J., Zacharias, W.J., Mayhew, C.N., Lim, H.W., and Iwafuchi, M. (2024). Pioneer and PRDM transcription factors coordinate bivalent epigenetic states to safeguard cell fate. Mol. Cell *84*, 476–489.e10. https://doi.org/10.1016/j.molcel.2023.12.007.

37. Patsalos, A., Tzerpos, P., Halasz, L., Nagy, G., Pap, A., Giannakis, N., Lyroni, K., Koliaraki, V., Pintye, E., Dezso, B., et al. (2019). The BACH1-HMOX1 Regulatory Axis Is Indispensable for Proper Macrophage Subtype Specification and Skeletal Muscle Regeneration. J. Immunol. *203*, 1532–1547. https://doi.org/10.4049/jimmunol.1900553.

38. Kim, D., Paggi, J.M., Park, C., Bennett, C., and Salzberg, S.L. (2019). Graph-based genome alignment and genotyping with HISAT2 and HISAT-genotype. Nat. Biotechnol. *37*, 907–915. https://doi.org/10.1038/s41587-019-0201-4.

39. Pertea, M., Pertea, G.M., Antonescu, C.M., Chang, T.C., Mendell, J.T., and Salzberg, S.L. (2015). StringTie enables improved reconstruction of a transcriptome from RNA-seq reads. Nat. Biotechnol. *33*, 290–295. https://doi.org/10.1038/nbt.3122.

40. Li, H., Handsaker, B., Wysoker, A., Fennell, T., Ruan, J., Homer, N., Marth, G., Abecasis, G., and Durbin, R.; 1000 Genome Project Data Processing Subgroup (2009). The Sequence Alignment/Map format and SAMtools. Bioinformatics *25*, 2078–2079. https://doi.org/10.1093/bioinformatics/btp352.

41. Quinlan, A.R., and Hall, I.M. (2010). BEDTools: a flexible suite of utilities for comparing genomic features. Bioinformatics *26*, 841–842. https://doi.org/10.1093/bioinformatics/btq033.

42. Zhang, Y., Liu, T., Meyer, C.A., Eeckhoute, J., Johnson, D.S., Bernstein, B.E., Nusbaum, C., Myers, R.M., Brown, M., Li, W., et al. (2008). Model-based analysis of ChIP-Seq (MACS). Genome Biol. *9*, R137. https://doi.org/10.1186/gb-2008-9-9-r137.

43. Li, H., and Durbin, R. (2009). Fast and accurate short read alignment with Burrows-Wheeler transform. Bioinformatics *25*, 1754–1760. https://doi.org/10.1093/bioinformatics/btp324.

44. de Hoon, M.J., Imoto, S., Nolan, J., and Miyano, S. (2004). Open source clustering software. Bioinformatics *20*, 1453–1454. https://doi.org/10.1093/bioinformatics/bth078.

45. Saldanha, A.J. (2004). Java Treeview–extensible visualization of microarray data. Bioinformatics *20*, 3246–3248. https://doi.org/10.1093/bioinformatics/bth349.

46. Hulsen, T., de Vlieg, J., and Alkema, W. (2008). BioVenn - a web application for the comparison and visualization of biological lists using area-proportional Venn diagrams. BMC Genomics *9*, 488. https://doi.org/10.1186/1471-2164-9-488.

47. Khan, A., and Mathelier, A. (2017). Intervene: a tool for intersection and visualization of multiple gene or genomic region sets. BMC Bioinform. *18*, 287. https://doi.org/10.1186/s12859-017-1708-7.

48. Ritchie, M.E., Phipson, B., Wu, D., Hu, Y., Law, C.W., Shi, W., and Smyth, G.K. (2015). limma powers differential expression analyses for RNA-sequencing and microarray studies. Nucleic Acids Res. *43*, e47. https://doi.org/10.1093/nar/gkv007.

49. Robinson, M.D., McCarthy, D.J., and Smyth, G.K. (2010). edgeR: a Bioconductor package for differential expression analysis of digital gene expression data. Bioinformatics *26*, 139–140. https://doi.org/10.1093/bioinformatics/btp616.

50. Zhou, Y., Zhou, B., Pache, L., Chang, M., Khodabakhshi, A.H., Tanaseichuk, O., Benner, C., and Chanda, S.K. (2019). Metascape provides a biologist-oriented resource for the analysis of systems-level datasets. Nat. Commun. *10*, 1523. https://doi.org/10.1038/s41467-019-09234-6.

51. Thorvaldsdóttir, H., Robinson, J.T., and Mesirov, J.P. (2013). Integrative Genomics Viewer (IGV): high-performance genomics data visualization and exploration. Brief. Bioinform. *14*, 178–192. https://doi.org/10.1093/bib/bbs017.

52. Amemiya, H.M., Kundaje, A., and Boyle, A.P. (2019). The ENCODE Blacklist: Identification of Problematic Regions of the Genome. Sci. Rep. *9*, 9354. https://doi.org/10.1038/s41598-019-45839-z.

53. Wingett, S., Ewels, P., Furlan-Magaril, M., Nagano, T., Schoenfelder, S., Fraser, P., and Andrews, S. (2015). HiCUP: pipeline for mapping and processing Hi-C data. F1000Res *4*, 1310. https://doi.org/10.12688/f1000research.7334.1.

54. Cairns, J., Freire-Pritchett, P., Wingett, S.W., Varnai, C., Dimond, A., Plagnol, V., Zerbino, D., Schoenfelder, S., Javierre, B.M., Osborne, C., et al. (2016). CHiCAGO: robust detection of DNA looping interactions in Capture Hi-C data. Genome Biol *17*, 127. https://doi.org/10.1186/s13059-016-0992-2.

55. Toda, G., Yamauchi, T., Kadowaki, T., and Ueki, K. (2021). Preparation and culture of bone marrow-derived macrophages from mice for functional analysis. Star Protoc. *2*, 100246. https://doi.org/10.1016/j.xpro.2020.100246.

56. Buenrostro, J.D., Giresi, P.G., Zaba, L.C., Chang, H.Y., and Greenleaf, W.J. (2013). Transposition of native chromatin for fast and sensitive epigenomic profiling of open chromatin, DNA-binding proteins and nucleosome position. Nat. Methods *10*, 1213–1218. https://doi.org/10.1038/nmeth.2688.

57. Daniel, B., Balint, B.L., Nagy, Z.S., and Nagy, L. (2014). Mapping the genomic binding sites of the activated retinoid X receptor in murine bone marrow-derived macrophages using chromatin immunoprecipitation sequencing. Methods Mol. Biol. *1204*, 15–24. https://doi.org/10.1007/978-1-4939-1346-6_2.

58. Orlando, G., Kinnersley, B., and Houlston, R.S. (2018). Capture Hi-C Library Generation and Analysis to Detect Chromatin Interactions. Curr. Protoc. Hum. Genet. *98*, e63. https://doi.org/10.1002/cphg.63.

59. Giannakis, N., Sansbury, B.E., Patsalos, A., Hays, T.T., Riley, C.O., Han, X., Spite, M., and Nagy, L. (2019). Dynamic changes to lipid mediators support transitions among macrophage subtypes during muscle regeneration. Nat. Immunol. *20*, 626–636. https://doi.org/10.1038/s41590-019-0356-7.

60. Shrum, B., Anantha, R.V., Xu, S.X., Donnelly, M., Haeryfar, S.M.M., McCormick, J.K., and Mele, T. (2014). A robust scoring system to evaluate sepsis severity in an animal model. BMC Res. Notes *7*, 233. https://doi.org/10.1186/1756-0500-7-233.

61. Sulzbacher, M.M., Sulzbacher, L.M., Passos, F.R., Bilibio, B.L.E., de Oliveira, K., Althaus, W.F., Frizzo, M.N., Ludwig, M.S., Da Cruz, I.B.M., and Heck, T.G. (2022). Adapted Murine Sepsis Score: Improving the Research in Experimental Sepsis Mouse Model. BioMed Res. Int. *2022*, 5700853. https://doi.org/10.1155/2022/5700853.

62. Daniel, B., Nagy, G., Hah, N., Horvath, A., Czimmerer, Z., Poliska, S., Gyuris, T., Keirsse, J., Gysemans, C., Van Ginderachter, J.A., et al. (2014). The active enhancer network operated by liganded RXR supports angiogenic activity in macrophages. Genes Dev. *28*, 1562–1577. https://doi.org/10.1101/gad.242685.114.

STAR★METHODS

KEY RESOURCES TABLE

REAGENT or RESOURCE	SOURCE	IDENTIFIER
Antibodies		
Anti-RNAPII-pS2	Abcam	Cat# ab5095; RRID: AB_304749
Anti-HDAC1	Abcam	Cat# ab7028; RRID: AB_305705
APC anti-mouse F4/80	BioLegend	Cat# 123116; RRID: AB_893481
PE-Cy7 anti-mouse CD11b	BioLegend	Cat# 101216; RRID: AB_312799
PE anti-mouse CD11c	BD Biosciences	Cat# 561044; RRID: AB_2033996
AF700 anti-mouse MHCII (I-A/I-E)	Biolegend	Cat# 107622; RRID: AB_493727
PerCP-Cy5.5 anti-mouse Ly6G	Biolegend	Cat# 127616; RRID: AB_1877271
FITC anti-mouse Ly6C	Biolegend	Cat# 128005; RRID: AB_1186134
APC-Cy7 anti-mouse SiglecF	BD Biosciences	Cat# 565527; RRID: AB_2732831
BV421 anti-mouse NK1.1	Biolegend	Cat# 108731; RRID: AB_10895916
BV421 anti-mouse CD3 epsilon	Biolegend	Cat# 100341; RRID:AB_2562556
BV421 anti-mouse B220	Biolegend	Cat# 103239; RRID: AB_10933424
PE anti-mouse CD115	Biolegend	Cat# 135505; RRID: AB_1937254
BV421 anti-mouse CD45.2	BD Biosciences	Cat# 562895; RRID: AB_2737873
FITC anti-mouse CD45.1	Biolegend	Cat# 110705; RRID: AB_313494
PE anti-CD45	Biolegend	Cat# 103105; RRID: AB_312970
Anti-mouse BACH1	Custom-generated (Patsalos et al.[37])	N/A
Anti-mouse BACH1 (clone F-9)	Santa Cruz Biotechnology	Cat# sc-271211; RRID: AB_10608972
Anti-Heme Oxygenase 1 antibody (HO-1)	Abcam	Cat# Ab13248; RRID: AB_2118663
Fc Receptor blocking reagent, mouse	Miltenyi Biotec	Cat# 130-092-575; RRID:AB_2892833
CD45 MicroBeads, mouse	Miltenyi Biotec	Cat# 130-052-301;RRID:AB_2877061
Goat-anti-mouse IgG (H+L), HRP conjugate	Advansta	Cat# R-05071-500; RRID: AB_10718209
Goat-anti-rabbit IgG (H+L), HRP conjugate	Advansta	Cat# R-05072-500; RRID: AB_10719218
Bacterial and virus strains		
pLV[Exp]-Neo-CMV>3xFLAG/mBach1	Vectorbuilder	Custom design
pLV[Exp]-EGFP/Puro-EF1A>mCherry	Vectorbuilder	VB010000-9492agg
Chemicals, peptides, and recombinant proteins		
Mouse recombinant interleukin 4	Peprotech	214–14
Mouse recombinant interferon alpha 1	R&D Systems	12105–1
Mouse recombinant interferon beta	R&D Systems	8234-MB
Mouse recombinant interferon gamma	R&D Systems	485-MI
Hemin	Sigma Millipore	51280-1G
Ammonium hydroxide solution	Sigma Millipore	338818–100ML
Cardiotoxin	Sigma Millipore	11061-96-4
High Molecular Weight poly(I:C), TLR3 agonist	InvivoGen	tlrl-pic
Resiquimod (R848), TLR7/8 agonist	InvivoGen	tlrl-r848-5
ODN1826, TLR9 Agonist	InvivoGen	tlrl-1826
LPS (Salmonella enterica serotype Minnesota Re 595)	Sigma Millipore	L6261
Penicillin-Streptomycin (10,000 U/mL)	Thermo Fisher Scientific	15140122
Glutamax™ Supplement	Thermo Fisher Scientific	35050061
Debris removal solution	Miltenyi Biotec	130-109-398
Ponceau S Staining Solution	Thermo Fisher Scientific	A40000279

(*Continued on next page*)

Continued

REAGENT or RESOURCE	SOURCE	IDENTIFIER
Dulbecco's Modification Of Eagles Medium (DMEM)	Thermo Fisher Scientific	10569044
Gibco's Macrophage Serum Free Media	Gibco, Thermo Fisher Scientific	12065074
Normal mouse serum	Thermo Fisher Scientific	10410
Normal rat serum	Thermo Fisher Scientific	10710C
HBSS, calcium, magnesium, no phenol red	Thermo Fisher Scientific	14025092
D-PBS, no calcium, no magnesium	Thermo Fisher Scientific	14190144
Collagenase II	Gibco, Thermo Fisher Scientific	17101015
Collagenase IV	Gibco, Thermo Fisher Scientific	17104019
Deoxyribonuclease I from bovine pancreas	Sigma Millipore	D4263
Critical commercial assays		
High-Capacity cDNA Reverse Transcription Kit	Applied Biosystems	4368813
Light Cycler 480 SY Green Master	Roche	46887352001
ELISA MAX™ Deluxe Set Mouse IL-6	BioLegend	431316
ELISA MAX™ Deluxe Set Mouse TNF-α	BioLegend	430916
Pierce™ BCA Protein Assay Kit	Thermo Fisher Scientific	23227
Nuclear Extraction Kit	Chemicon International, Sigma Millipore	2900
NextSeq 500/550 High Output Kit v2.5 (75 Cycles)	Illumina	20024906
NEBNext Ultra II RNA Library Prep with Purification Beads	New England BioLabs	E7775
CountBright™ Absolute Counting Beads	Thermo Fisher Scientific	C36950
eBioscience Fixable Viability Dye eFluor 506	Thermo Fisher Scientific	65-0866-14
Arima Hi-C kit	Arima Genomics	A510008
SureSelect Custom Tier2 2.9Mb Probes targeting murine BACH1-bound sequences	Agilent	This study custom design
SureSelect XT HS Target Enrichment Kit	Agilent	G9916B
Accel-NGS 2S Plus DNA Library Kit	Swift Biosciences	21024
Deposited data		
RNA-seq, ChIP-seq, ATAC-seq and cHi-C	This paper	GEO: GSE245651
Experimental models: Cell lines		
Primary bone marrow-derived macrophages	WT C57BL/6, Bach1f$^{fl/fl}$;Lyz2-Cre, Nrf2f$^{fl/fl}$;Lyz2-Cre, Bach1f$^{fl/fl}$;Nrf2f$^{fl/fl}$;Lyz2-Cre	N/A
L929 mouse fibroblast cell line	WT C3H/An mouse	ATCC
Control & Bach1-FKBP12-FLAG tagged HCT116	HCT116	This study
Experimental models: Organisms/strains		
C57BL/6	The Jackson Laboratory	000664
Bach1$^{fl/fl}$	This study	N/A
Nfe2l2(Nrf2)$^{fl/fl}$	The Jackson Laboratory	025433
Bach1$^{fl/fl}$;*Nfe2l2*$^{fl/fl}$	This study	N/A
Lyz2-Cre	The Jackson Laboratory	004781
Vav1-Cre	The Jackson Laboratory	008610
Oligonucleotides		
Mouse *Il6*,*Il1b, Ppia,* and *Hmox1* primers for mRNA expression	Il6, Il1b, Ppia: Czimmerer et al[30]; Hmox1: Patsalos et al.[37]	https://doi.org/10.4049/jimmunol.1900553; https://doi.org/10.1016/j.immuni.2022.10.004

(*Continued on next page*)

Continued

REAGENT or RESOURCE	SOURCE	IDENTIFIER
Mouse *Tnf* primers for mRNA exxpression	Forward: ACAAGCCTGTAGCCCACGTC Reverse: GGTGAGGAGCACGTAGTCGG	N/A
Software and algorithms		
FlowJo v10	BD Life Sciences	https://www.flowjo.com/
GraphPad Prism v8	GraphPad Software	https://www.graphpad.com/
HISAT2 v2.1.0	Kim et al.[38]	https://ccb.jhu.edu/software/hisat2
StringTie v1.3.4d	Pertea et al.[39]	https://ccb.jhu.edu/software/stringtie
SAMtools v1.7	Li et al.[40]	http://samtools.sourceforge.net
HOMER	Heinz et al.[9]	http://homer.ucsd.edu/homer
BEDTools v2.27.1	Quinlan and Hall[41]	https://bedtools.readthedocs.io
MACS2	Zhang et al.[42]	https://github.com/macs3-project/MACS
BWA v07.17	Li and Durbin[43]	https://bio-bwa.sourceforge.net/
Cluster 3.0	de Hoon et al.[44]	http://bonsai.hgc.jp/~mdehoon/software/cluster/software.htm
JavaTreeView v1.1.6r4	Saldanha et al.[45]	https://jtreeview.sourceforge.net/
BioVenn	Hulsen et al.[46]	https://www.biovenn.nl/
Intervene	Khan and Mathelier[47]	https://asntech.shinyapps.io/intervene/
limma (R package)	Ritchie et al.[48]	https://bioconductor.org/packages/limma
edgeR (R package)	Robinson et al.[49]	https://bioconductor.org/packages/edgeR
pheatmap (R package)	Pheatmap 1.0.13	https://github.com/raivokolde/pheatmap
tidyverse (R package)	Tidyverse 2.0.0	https://www.tidyverse.org
sqldf (R package)	sqldf 0.4-12	https://cran.r-project.org/package=sqldf
ggplot (R package)	ggplot2 4.0.3	https://ggplot2.tidyverse.org/
Metascape	Zhou et al.[50]	https://metascape.org
Integrative Genomics Viewer (IGV v2.4.16)	Thorvaldsdóttir et al.[51]	https://software.broadinstitute.org/software/igv
ENCODE blacklist	Amemiya et al.[52]	https://github.com/Boyle-Lab/Blacklist
HiCUP	Wingett et al.[53]	https://www.bioinformatics.babraham.ac.uk/projects/hicup/
CHiCAGO	Cairns et al.[54]	https://bioconductor.org/packages/Chicago
LoopSage	Korsak et al.[29]	https://github.com/loop-sage/LoopSage
Other		
gentleMACS™ Octo Dissociator with Heaters	Miltenyi Biotec	N/A
LS columns	Miltenyi Biotec	130-042-401
MS columns	Miltenyi Biotec	130-042-201
bioRender	N/A	https://www.biorender.com/

EXPERIMENTAL MODEL AND STUDY PARTICIPANT DETAILS

Mouse strains

Female and male breeder mice for C57BL/6 mice were used and bred under specific-pathogen-free (SPF) conditions. *Bach1*$^{fl/fl}$*Lyz2*-Cre and *Bach1*$^{-/-}$ animals were kept on the C57BL/6 genetic background. The *Bach1*$^{fl/fl}$ animals were generated in the Institute of Experimental Medicine (Budapest) (Figure S2D). *Lyz2*-Cre mouse strain was a generous gift from Dr. Attila Mocsai (Semmelweis University, Budapest). We crossed *Bach1*$^{fl/fl}$ animals with *Lyz2-Cre* animals to establish the conditional deletion strain (*Bach1*$^{fl/fl}$ *Lyz2*-Cre). *Nrf2*$^{fl/fl}$ mice were purchased from Jackson Labs. In the *in vivo* experiments, we used *Bach1*$^{+/+}$ or *Bach1*$^{fl/ff}$ littermates as controls. Animals were handled according to the regulatory standards of the animal facilities of the University of Debrecen (permission number: 9/2023/DEMAB) and Johns Hopkins All Children's Hospital (license number: MO21C391). Eight- to 12-week-old healthy male mice were used for all our experiments.

Bone marrow-derived macrophage (BMDM) differentiation

BMDM differentiation was performed as previously described.[55] In brief, bone marrow cells isolated from mouse femurs and tibias were differentiated into BMDMs for 5 days in macrophage medium supplemented with L929-conditioned medium containing M-CSF. On day 5, culture medium was replaced with fresh macrophage medium supplemented with 1% FBS and cells were cultured for an additional 24 h. On day 6, differentiated BMDMs were either processed for downstream analyses or subjected to experimental stimulation.

Human colorectal carcinoma HCT116 cell line

HCT116 cells were used to generate a stable BACH1-FKBP12-3xFLAG knock-in line. Cells were transfected with CRISPR/Cas9 and homologous donor plasmids designed to introduce a C-terminal FKBP12-3xFLAG tag at the endogenous BACH1 locus. Following dual antibiotic selection (Geneticin and Hygromycin), individual clones were isolated, screened by PCR, and homozygous knock-in clones were expanded and maintained for subsequent studies.

METHOD DETAILS

Stimulation of BMDMs

BMDMs were treated with IL-4 (20 ng/mL), IFNγ (20 ng/mL), IFNβ (20 ng/mL), heme (20 and 100 μM), LPS (10 and 100 ng/ml), polyI:C HMW (10 μg/ml), R848 (1 μg/ml), and ODN1826 (5 μM). The stimulation period is specified in the figure legends. For lentiviral transduction of BMDMs, a high titer (>$1x10^8$ TU/ml) lentiviral vector containing the full-length cDNA of mouse BACH1 was designed and ordered as packaged virus from VectorBuilder. Transduction efficiency was tested with control virus: pLV[Exp]-EGFP/Puro-EF1A>mCherry. $5x10^5$ BMDMs were transduced at Day 3 of differentiation at MOI:5 and used for experiments after 48-72 hours.

Real-time quantitative PCR for mRNA detection (qPCR)

RNA was isolated with Trizol reagent (Ambion). RNA was reverse transcribed with High-Capacity cDNA Reverse Transcription Kit (Applied Biosystems) according to manufacturer's protocol. Transcript quantification was performed by qPCR reactions using SYBR green master mix (Roche). Transcript expressions were normalized to Ppia.

RNA-seq

The quality of total RNA samples was checked on Agilent BioAnalyzer using Eukaryotic Total RNA Nano Kit according to manufacturer's protocol. Samples with RNA integrity number (RIN) value >7 were accepted for library preparation process. RNA-Seq libraries were prepared from total RNA using Ultra II RNA Sample Prep kit (New England BioLabs) according to the manufacturer's protocol. Briefly, poly-A RNAs were captured by oligo-dT conjugated magnetic beads then the mRNAs were eluted and fragmented at 94-Celsius degree. First strand cDNA was generated by random priming reverse transcription and after second strand synthesis step double stranded cDNA was generated. After repairing ends, A-tailing and adapter ligation steps adapter ligated fragments were amplified in enrichment PCR and sequencing libraries were generated. Sequencing runs were performed on Illumina NextSeq 500 and HiSeq2000 instruments.

ATAC-seq

Assay for Transposase-Accessible Chromatin using sequencing (ATAC-seq) was carried out as described earlier with minor modifications.[56] 50,000 cells were lysed with ATAC-Lysis Buffer (10mM Tris-HCl pH7.4, 10mM NaCl, 3mM $MgCl_2$, 0.1% IGEPAL) and nuclei were isolated were used for tagmentation using Nextera DNA Library Preparation Kit (Illumina). After tagmentation DNA was purified with MinElute PCR Purification Kit (Qiagen). Tagmented DNA was amplified with Kapa Hifi Hot Start Kit (Kapa Biosystems) using 8-10 PCR cycles. Amplified libraries were purified again with MinElute PCR Purification Kit. Fragment distribution of libraries was assessed with Agilent Bioanalyzer and libraries were sequenced on a HiSeq 2500 platform.

ChIP-seq

Chromatin immunoprecipitation (ChIP) was performed with minor modifications of the previously described protocol.[57] Briefly, $1x10^7$ BMDMs were double cross-linked with DSG (45min) and formaldehyde (10min). Nuclei were isolated using a lysis buffer containing 0.15M NaCl, 0.005M EDTA pH 7.5, 0.05M Tris-HCl pH 7.5, 0.5% NP40, supplemented with protease inhibitor (Roche) prior to use. Chromatin was sheared with sonication and immunoprecipitated overnight with the appropriate antibody. Chromatin-antibody complexes were extensively washed and eluted after pull-down by paramagnetic beads. Eluted complexes were decrosslinked overnight and purified by the MinElute PCR Purification Kit. Immunoprecipitated DNA was quantified by a Qubit fluorometer. Libraries were prepared from 10ng DNA withTruSeq ChIP library systems (Illumina) according to the manufacturer's instructions. Libraries were sequenced on HiSeq 2500. The following antibodies were used: BACH1 (custom from Spilianakis lab[37]), RNAPII-pS2 (ab5095), RAD21 (ab992), HDAC1 (ab7028).

In the case of ChIP-MS (RIME) BACH1 peptides were immunoprecipated and analysed in LC-MS/MS in LTQ Velos Orbitrap mass spectrometer, using the Rapid Immunoprecipitation Mass spectrometry of Endogenous proteins (RIME) for analysis of chromatin complexes.[23]

Immunoprecipitation coupled with Mass-Spectrometry (IP-MS)

Bach1-FKBP12-FLAG tagged cells or wildtype HCT116 cells were harvested by scraping then pelleted by centrifugation (5 mins, 4000 RPM, 4°C). Cells were resuspended in 5mL Buffer A (50 mM Tris/Cl pH 7.5, 50 mM Potassium Acetate, 10% (V/V) Glycerol, 0.4% (V/V) Triton X-100 with 1 Roche complete EDTA Free protease inhibitor tablet per 50 mL) and lysed by sonication (Three cycles of 10s/30s on/off at 20%). Samples were then clarified by centrifugation (10 mins, 15,600 RPM, 4°C). The supernatant was then loaded onto Anti-FLAG M2 resin (Sigma), pre-washed with lysis buffer and incubated for 1h, 4°C rolling. The resin was washed as follows: 1x Buffer A, 3x Buffer B (50 mM Tris/Cl pH 7.5, 50 mM Potassium Acetate, 5% (V/V) Glycerol) and 3x Buffer C (50 mM Tris/Cl pH 7.5, 50 mM Potassium Acetate, 5% (V/V) Glycerol, 0.5 mM TCEP). Samples were then eluted using an equal volume of 250ug/ml FLAG peptide in buffer C, to volume of resin. Elute samples were collected after incubation for 1h, 4°C rolling, and again after overnight for, 4°C, rolling. Samples were pooled and submitted for LC-MS/MS analysis.

Capture Hi-C

We applied a capture Hi-C (cHi-C) approach[58] to map chromatin interactions in 9,127 BACH1-bound genomic sites (top BACH1 bound sites ranked based on RPKM coverage in a-BACH1 ChIP-seq). Briefly, differentiated mouse BMDMs were cross-linked with 2% formaldehyde and stored as cell pellets at -80°C. Cells were lysed and processed using the Arima Hi-C kit according to the manufacturer's protocol. A capture enrichment step was applied to the generated Hi-C libraries using custom-designed probes (SureSelect, Agilent Tier 2 -2,9Mb) targeting a selective group of regulatory elements, including the 9,127 BACH1-bound genomic sites. cHi-C libraries were prepared with the Arima Hi-C kit and Agilent SureSelect library systems according to the manufacturers's protocol.

Cardiotoxin (CTX)-induced acute sterile muscle injury model

Mice (8–12-week-old males) were anesthetized with isoflurane (adjusted flow rate or concentration to 2.0-2.5%), and 50 μl of 10 μM CTX (217503-1MG; EMD Millipore) was injected into the tibialis anterior (TA) muscle. Mice were brought out of anesthesia and monitored until they were euthanized and processed at various time points. Muscles were recovered for flow cytometry analysis at day 1 to day 4 after injury or for muscle histology.

Bone marrow transplantation (BMT) and the generation of BM-chimeric mice

Recipient mice consisted of either CD45.1$^+$ congenic BoyJ mice or F1 offspring generated by crossing BoyJ (CD45.1$^+$) mice with C57BL/6 (CD45.2) mice, resulting in CD45.1/CD45.2 heterozygous were irradiated with 11 Gy. The irradiated mice were kept in special cages with HEPA filter before and after BMT. The graft bone marrow (BM) cells were isolated from the donor CD45.1$^+$ Bach1+/+ and CD45.2$^+$ *Bach1*-deficient mice by bone marrow flushing. The recipient mice were anesthetized with 2.0-2.5v/v% isoflurane, and 5 x 10^6 donor BM cells in sterile PBS were injected into the retroorbital cavity. In the chimera experiments, different ratios of CD45.1$^+$ Bach1$^{+/+}$ and CD45.2$^+$ Bach1-deficient BM cells were injected retroorbitally. The drinking water of the recipient mice contained 125 mg/L clavulanic acid and 875 mg/L amoxycillin for 4 weeks. After 8-12 weeks of BMT, the mice were sacrificed for tissue processing and flow cytometry analysis.

Tissue processing, flow cytometry, and fluorescence-activated cell sorting (FACS)

After the euthanasia of mice derived from the BMT experiments, the blood was collected from the retroorbital cavity, which was followed by the isolation of peritoneal lavage with 7 mL PBS, perfusion of the lungs, collection of the lungs and one lobe of liver, collection of the spleen and the bone marrow of one femur. The spleen was smashed in ice cold PBS on a 100 μm cell strainer using a 10 mL syringe. The red blood cells (RBCs) were removed by Red Blood Cell Removal solution (Miltenyi Biotec). The blood leukocytes, the BM-, peritoneal-, and spleen-derived cells were washed twice with ice cold PBS and filtered with a 100 μm cell strainer. Cell pellets were collected by centrifugation at 350xg for 5 min, 4°C. The isolated lung and liver samples were homogenized using digestion solution containing 500 μg/mL deoxyribonuclease I (Merck-Millipore), 1 mg/mL collagenase IV (Gibco) in empty RPMI1640 (Thermo Fischer). The gentleMACS™ Octo Dissociator with Heaters (Miltenyi Biotec) was used to dissociate the lungs and liver tissues. After dissociation, FBS was added to the solution to inhibit the enzymatic reactions. The cell homogenates were washed twice with 70 μm cell strainers. After washing steps, the tissue debris was removed using Debris Removal Solution (Miltenyi Biotec) based on the manufacturer's protocol. The RBCs were removed as described above. Purified tissue-derived cells were washed again using 70 μm cell strainers. The cells were stained with eBioscience™ Fixable Viability Dye eFluor™ 506 (Thermo Fischer) in PBS, followed by staining with Fc receptor blocker (Miltenyi Biotec) and fluorochrome-conjugated antibodies for 20 min on ice. The stained cells were washed with ice cold magnetic-activated cell sorting (MACS) buffer containing 0.5% bovine serum albumin (BSA) and 2 mM EDTA in PBS. Flow cytometry analysis was performed to measure the number and the ratio of macrophages, monocytes, neutrophil and eosinophil granulocytes of the isolated tissues.

The isolation of muscle-infiltrating MFs was performed as described previously.[37,59] Briefly, the fascia of the TA was removed, and muscles were dissociated in either RPMI containing 0.2% collagenase B (Roche Diagnostics GmbH) at 37°C for 1 h or by using the magnetic-activated cell sorting (MACS) Skeletal Muscle Dissociation Kit (130–098-305; Miltenyi) or gentleMACS Octo Dissociator, per kit instructions. Cell homogenate was filtered through a 100 μm and a 40 μm cell strainer, and CD45$^+$ cells were isolated using magnetic sorting (Miltenyi Biotec). For FACS, MFs were treated with Fcγ receptor blocking antibodies, 5% normal rat serum, and 5% normal mouse serum. The Ly6C^{high}F4/80^{low} MFs, Ly6C^{low}F4/80^{high} MFs, and Ly6G^{high}F4/80$^-$ neutrophils were quantified.

The BD FACSAria III (BD Life Sciences) instrument was used for flow cytometry measurement and FACS. To measure the number of the cells, CountBright™ Absolute Counting Beads (Thermo Fischer) were used based on the manufacturer's suggestion. The flow cytometry data were analyzed with FlowJo software, version 10 (BD Life Sciences). The following antibodies were used for cell isolation: F4/80 (BM8) (Biolegend), CD3ε (145-2C11), CD11b (M1/70), CD11c (N418), CD45 (30-F11), CD45.1 (A20), CD45.2 (104), CD115 (AFS98), I-A/I-E (1A8), Ly6C (HK1.4), Ly6G (1A8), NK1.1 (PK136), B220 (RA3-6B2) (all Biolegend), SiglecF (E50-2440) (BD Pharmigen).

Intraperitoneal lipopolysaccharide (LPS)-induced sepsis model

Six-to-8-week-old male C57BL/6 WT mice were used for these experiments. The mice were injected intraperitoneally (i.p.) with 10 mg/kg LPS (*Salmonella enterica* serotype *minnesota* Re 595-derived, Sigma-Aldrich) dissolved in 500 μL 1xPBS. The control mice were challenged i.p. with same volumes of PBS. After 4 hours of treatments, the mice were sacrificed and 500 μL blood was collected for serum preparation. In another set of experiments, mice were monitored for 4 days, and disease score was calculated based on body condition and clinical assessment by researcher blinded to experimental grouping based on appearance, level of consciousness, activity, response to stimulus, eye/eyelid openness, alertness and respiration quality.[60,61] All the experimental mice were terminated on day 4. Animals were handled according to the regulatory standards of the animal facilities of the University of Debrecen. Animal studies were approved by the Animal Care and Protection Committee at the University of Debrecen (9/2023/DEMAB).

Immunoblot

To detect BACH1 protein, nuclear extracts of BMDM were used. Briefly, the supernatant of BMDM was replaced with ice cold PBS containing 2 mM EDTA, and the cells were shaken for 5 min. The BMDM were scraped carefully and transferred into conical tubes. The collected cells were centrifuged at 300xg at 4°C for 10 minutes. To gain subcellular cytosolic and nuclear fractions, the Chemicon's Nuclear Extraction kit (Merck-Millipore) was used based on the manufacturer's protocol. The nuclear protein concentration was measured with the Pierce BCA Protein Assay Kit (Thermo Scientific) at a wavelength of 570 nm (Biotek Synergy HT Plate reader). Every sample was normalized using BSA standard (Thermo Scientific, stock is 2 mg/mL). The samples were diluted up to 1 mg/mL concentration, mixed with equal volumes of 2×SDS denaturation-buffer (0.125 M Tris-HCl, pH 6.8, containing 4% SDS, 20% glycerol, 10% MEA, 0.02% bromophenol blue dye), and incubated at 95°C for 10 min. Proteins were separated on 10 % SDS-polyacrylamide gels and blotted onto a PVDF membrane (Merck-Millipore) using the semi-dry blotting method. Membranes were blocked with 5% non-fat dry milk or with 5% BSA in Tris-buffered saline and Tween 20 (TTBS) for 1 hour at room temperature (RT). The primary anti-mBACH1 (Santa Cruz Biotechnology) and anti-mHO-1 (Abcam) antibodies were diluted in 2.5% milk in 1xTTBS, with a dilution ratio of 1:200 and 1:1000, respectively. The membranes were incubated overnight at 4°C. The membranes were washed three times with 1xTTBS for 5 min at RT, incubated with horseradish peroxidase labelled secondary antibodies (Merck-Millipore, Advansta) at 1:10,000-1:30,000 dilution ratios for 40 min at RT, followed by three times wash with 1xTTBS for 5 min at RT. The targeted protein bands were visualized using ECL-Kit (Thermo Fischer and Advansta).

Enzyme-linked immunosorbent assay (ELISA)

Serum samples and cell culture supernatants derived from BMDM were collected at the indicated times. Samples were centrifuged at 1000x*g* for 10 min at 4°C, and the supernatants were separated and stored at -80°C until analysis. These cell culture supernatants were then probed for the presence of the following cytokine using ELISA kits according to the manufacturer's instructions: TNFα, IL-1β, IL-6, and IL-10 (BioLegend). Plates were read using the BIO-TEK Synergy HT Multi-Detection Microplate Reader.

QUANTIFICATION AND STATISTICAL ANALYSIS

Statistical analysis

Statistical analysis for qRT-PCR and ELISA methods: the error bars represent standard deviation (SD). The two-tailed Student's *t* test was used to evaluate the significance of differences between two groups. The statistical analysis and graphs were performed and generated using GraphPad Prism software, version 8. Quantification and alignments of NGS analysis for RNA-seq, ChIP-seq and ATAC-seq are also described in more detail in the appropriate method sections.

RNA-seq analysis

Raw sequence reads were aligned to the mm10 reference genome with HISAT2 (v2.1.0) using default parameters.[38] From the BAM files, transcripts were assembled with StringTie (v1.3.4d).[39] BAM files were indexed with SAMtools (v1.7), and then coverage (bedgraph) files were generated by HOMER's makeUCSCfile program.[9,40] Gene expression levels were determined in FPKM values.

For secondary analyses, genes, that showed a higher than 0 FPKM value in at least one sample were considered expressed and were included in the comparative analyses. Then, for each sample, the FPKM (Fragments Per Kilobase of transcript per Million mapped reads) value was normalized by the decile value of the given sample. The differentially expressed genes were determined with one-way ANOVA supplemented with a post-hoc Tukey HSD statistical test using the stats, tidyverse, and sqldf packages in R. The applied cut-off values (p-value and/or fold change (FC)) were indicated in the figure descriptions in all cases. The multi-dimensional scaling (MDS) plot was generated by plotMDS function of the limma package, and the sample-to-sample distance plot was visualized

by the edgeR[49] and pheatmap packages in R (v3.5.1).[48] The biological pathways were predicted with Metascape (v3.5.20230501).[50] K-means clustering of the genes was carried out by Cluster 3.0 and the applied similarity metric was the centered correlation.[44]

ATAC-seq analysis

Raw sequence reads were aligned to the mm10 reference genome assembly with default parameters by using the BWA tool (v07.17) and BAM files were generated with SAMtools (v1.7).[9,43] Narrow peaks were predicted with the callpeak function of MACS2 and their widths were fixed to 200 bp relative to their summits.[41] Artifacts were removed according to the blacklisted genomic regions of ENCODE.[62] Genome coverage (bedgraph) files were generated by HOMER's makeUCSCfile, then they were indexed to tdf files with igvtools (v2.3.98).[45] The fragment length was set to 150-bp.

For the secondary analyses, consensus peak sets were generated separately from the CTX-injured muscle samples and the control and *Bach1*$^{-/-}$ samples in BMDM by using the mergeBed command of bedtools (v2.27.1).[41] Peaks that could be predicted from at least two samples were part of the consensus set in both cases. Then, for each sample, RPKM (Reads Per Kilobase per Million mapped reads) values were calculated on the consensus peak set by the coverageBed command of bedtools, and the RPKM values were normalized by the decile value of the given sample.

By using the decile normalized values, the differentially opened chromatin regions were defined by one-way ANOVA supplemented with a post-hoc Tukey HSD statistical test. As a cut-off, $p \leq 0.05$ and $FC \geq 1.5$ was applied. K-means clustering of the genomic regions was carried out by Cluster 3.0 and the applied similarity metric was the centered correlation.[44]

Transcription factor ChIP-seq analysis

The basic analysis of ChIP-seq samples (alignment, peak prediction and filtering, generation of coverage files) was performed in the same way as for ATAC-seq samples. BACH1 consensus peak set was generated by using 8 unstimulated samples and peaks that were present in at least 2 samples were considered as part of the consensus. Coverage values were calculated from the representative sample on the summit of the BACH1 consensus set. The separation of the promoter (promoter-TSS and 5' UTR) and enhancer (introns, intergenic, exons, 3' UTR, and TTS) regions was determined by HOMER'a annotatePeaks. Overlap between the MF-specific enhancers[20] and BACH1 peaks was performed by the intersectBed command of bedtools. The genomic distribution of the peaks was carried out also by HOMER's annotatePeaks, where promoter-TSS covers covers both promoter-TSS (TSS -1000-bp/+100-bp, according to the HOMER's definition), and 5' UTR, and intergenic includes both intergenic and non-coding regions. For the BACH1 chIP-seq redistribution heat map, the *de novo* gained and induced-gained BACH1 ChIP-seq peaks were separated based on their coverage (RPKM) values in the control sample (de novo induced: <1 RPKM; induced >1 RPKM). Then, the density of the gained peaks was depicted together in the same row with the density of the closest reduced peak. The (*de novo*) gained-reduced peak pairs were plotted in the order of their increasing distance from each other, and to this, their orientation from each other was converted to the same direction. The maximum distance between a (*de novo*) gained and reduced BACH1 peak was set to 250-kb.

RNA Polymerase II ChIP-seq analysis

The basic analysis of RNA Polymerase ChIP-seq samples (alignment, filtering of the peaks, generation of coverage files) was performed in the same way as for ATAC-seq samples. During peak calling broad peaks/domains were predicted.Transcriptional activity of the mm10 genes (n=24659) was calculated by the coverageBed (bedtools) on the TSS+100-kb region of the gene body or up to the TTS if the total length of the gene was shorter than 100-kb (the RNA Polymerase II moves ~44,4-bp per second,[62] thus during the 1-hr treatment, this is the distance where RNA Polymerase II activity could reliably measure). The calculated RPKM values were normalized by the decile value of the given sample. By using the decile normalized values, genes with different transcriptional activity were defined by one-way ANOVA supplemented with a post-hoc Tukey HSD statistical test. As a cut-off, $p \leq 0.05$ was applied for the determination of genes responsive to any treatment(s) in the control samples, and $p \leq 0.05$ and $FC \geq 1.5$ was applied to determine the genes affected by *Bach1*$^{-/-}$. K-means clustering of the genomic regions was carried out by Cluster 3.0 and the applied similarity metric was the centered correlation.[44]TSSs of the genes with different transcriptional activity were extended to ±100-kb (or maximum to the nearest gene(s), and the BACH1 peaks overlap with the extended regions were used for *de novo* motif enrichment analysis separately for each cluster.

De novo motif enrichment analysis and motif remap

De novo motif enrichment analysis was carried out by HOMER's findMotifsGenome program and was performed on the summit 200-bp regions of the peaks.[9] The targeted motif lengths were 10, 12, 14, and 16 bp. P-values were calculated by comparing the enrichment within the target regions and that of a random set of regions (background) generated by HOMER. For motif enrichment heat maps, matrices of the MF-specific TF motifs or the enriched motifs were mapped on the summit 200-bp regions of the peaks and then the frequency of their occurrence was plotted. For motif distribution plots, matrices of the enriched motifs were mapped following the order of regions in the tag density heat maps by using the -mbed parameter of HOMER's annotatePeaks in 20-bp windows within 2-kb frames relative to the peak centers. The top MARE and TRE motif scores for the redistributed BACH1 peak sets were determined by using the -mscore parameter of HOMER's annotatePeaks.

Visualization

Row-normalized gene expression heatmaps were visualized in R by pheatmap package. Read distribution (tag density) heat maps were visualized by JavaTreeView v1.1.6r4.[45] Histograms, pie- and (stacked) bar charts, box-, violin-, line-, and volcano plots were plotted by using GraphPad Prism v.9. The area-proportional Venn diagram was generated by BioVenn, the Chow-Ruskey diagram was plotted by Intervene.[46,47] Genome coverage (bedgraph) files were visualized by IGV v2.4.16 where the replicates that belong together were depicted as overlay tracks.[51] Proportional dot plots were visualized by ggplot by using the tidyverse, and ggthemr packages in R.

Capture Hi-C analysis & Loop dynamics simulation

cHi-C raw sequence output was processed with *Hicup* (v0.6.1)[53] to produce a filtered set of mapped interaction pairs in the mm10 genome. Interactions between virtual restriction fragments were detected using *Chicago* (v1.6.0)[54] and custom weights calculated from high-confidence interactions in the data. Bigwig files containing mapped normalized interaction pairs were uploaded to the IGV browser to visualize chromatin loops together with ChIP-seq tracks. *LoopSage*[29] was used to generate thermodynamic ensembles of 3D structures for topologically associated domain (TAD) regions by loop extrusion model (LEM) consisting of a stochastic simulation phase, employing a Monte Carlo approach to simulate the binding positions of cohesins, BACH1 and elongating RNA Polymerase, and a dynamical simulation phase, utilizing these positions to create 3D structures, allowing us to observe phase transition between sparse and condensed states in chromatin. For the loop strength and length analysis and to assess the relationship between transcriptional changes and chromatin looping dynamics, we used differential PolIISer2P occupancy data from heme-treated (n = 676 genes) and BACH1-deficient (n = 214 genes) BMDM. Chromatin loops were derived from capture Hi-C experiments performed on wild-type (WT), heme-treated, and BACH1-deficient samples. Loops were classified into 7 categories based on their presence or absence across the three conditions (WT, heme, BACH1-deficient), resulting from the 2^3–1 possible combinations. For loops detected in multiple conditions, the loop strength was averaged across experiments. Differentially expressed genes (DEGs) were assigned to loops based on proximity: a gene's transcription start site (TSS) was considered matched to a loop if either loop anchor overlapped with the TSS ±125 kb. Loops were then grouped into three categories relative to each DEG set: Loops present only in the experiment of interest (heme or BACH1-deficient), Loops present only in WT, and Common loops present in both the experiment of interest and WT. Distributions of loop strength and loop length were compared using Mann-Whitney U tests. Two-dimensional distributions of $\log_{10}$-transformed loop length and loop score were visualized for all loop categories.

Immunity, Volume *59*

Supplemental information

The transcription factor BACH1 couples chromatin priming and repression to enable macrophage plasticity and adaptation

Petros Tzerpos, Dóra Bojcsuk, Krisztian Bene, Noemí Caballero-Sánchez, Zofia Parteka-Tojek, Krzysztof Banecki, Sevastianos Korsak, Sarah M. Pritchett, Andreas Patsalos, Darby Oleksak, Wilhelm K. Berger, Michalis E. Sarris, Nikolaos Giannakis, Sophie Chantalat, Timea Cseh, Evangelia K. Papachristou, Ferenc Erdélyi, Zoltán Máté, Gabor Szabo, Gergely Nagy, Jason S. Carroll, Charalampos G. Spilianakis, John W.R. Schwabe, Dariusz Plewczynski, and Laszlo Nagy

Immunity, Volume *59*

Supplemental information

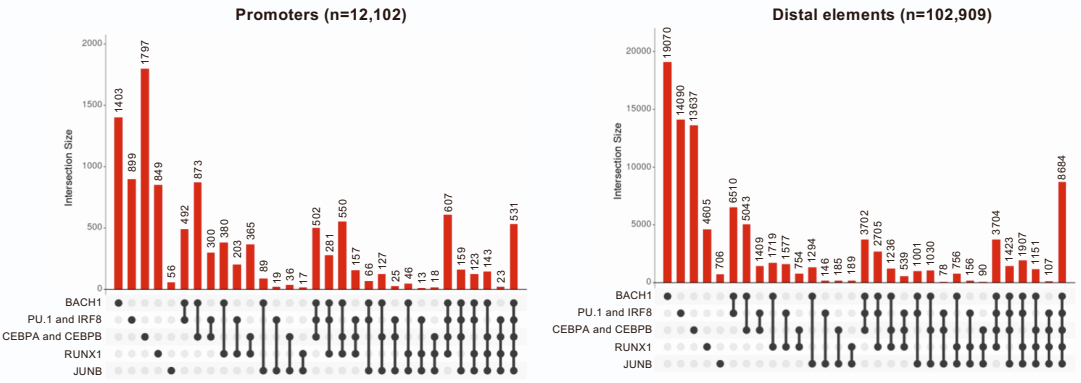
The transcription factor BACH1 couples chromatin priming and repression to enable macrophage plasticity and adaptation

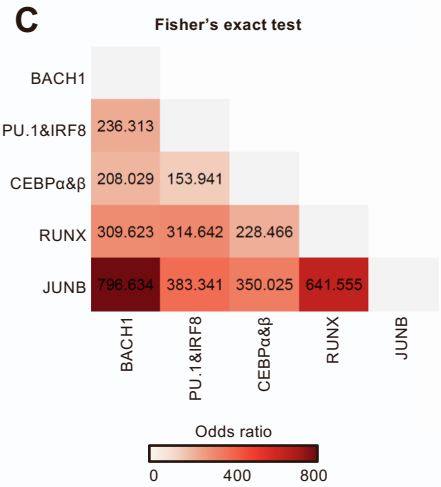
Petros Tzerpos, Dóra Bojcsuk, Krisztian Bene, Noemí Caballero-Sánchez, Zofia Parteka-Tojek, Krzysztof Banecki, Sevastianos Korsak, Sarah M. Pritchett, Andreas Patsalos, Darby Oleksak, Wilhelm K. Berger, Michalis E. Sarris, Nikolaos Giannakis, Sophie Chantalat, Timea Cseh, Evangelia K. Papachristou, Ferenc Erdélyi, Zoltán Máté, Gabor Szabo, Gergely Nagy, Jason S. Carroll, Charalampos G. Spilianakis, John W.R. Schwabe, Dariusz Plewczynski, and Laszlo Nagy

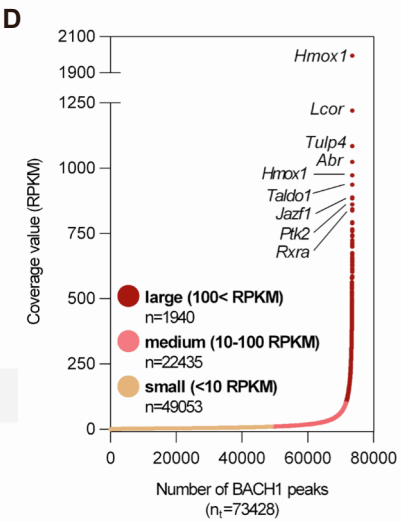
Figure S1.

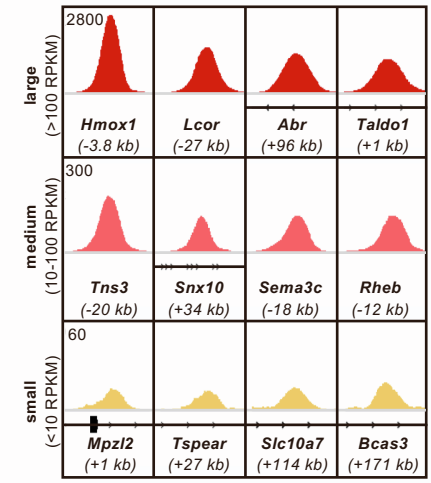
A

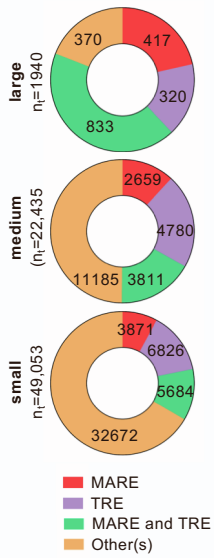
Transcription factor	Number of TFBSs
BACH1	73,428
PU.1	35,682
IRF8	38.724
CEBPα	46,776
CEBPβ	25,373
RUNX	35,348
JUNb	21,156
Pool of MF-specific regulatory regions	**115,021 (total)**
Promoters	**12,102**
Enhancers	**102,919**











G

"large" BACH1 peaks (n=1940)

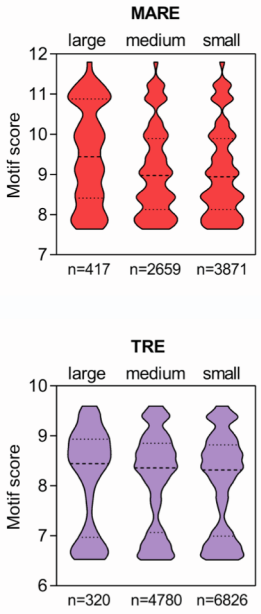
P-value	Target %	Bg%	Motif
1e-1109	64.43%	4.87%	MARE
1e-238	49.18 %	16.67 %	PU.1
1e-104	14.85%	3.10%	MAF
1e-90	19.95%	6.22%	USF2
1e-60	11.49%	3.11%	CEBP
1e-26	12.99%	6.29%	RUNX

"medium" BACH1 peaks (n=22435)

P-value	Target %	Bg%	Motif
1e-4700	43.07%	7.39%	TRE
1e-2662	40.54%	11.54%	PU.1
1e-515	21.15%	10.12%	CEBP
1e-498	5.43%	0.95%	PU.1:IRF
1e-267	9.23%	3.93%	RUNX
1e-219	9.61%	4.58%	USF2
1e-165	6.31%	2.81%	MEF2
1e-105	6.70%	3.65%	EGR

"small" BACH1 peaks (n=49053)

P-value	Target %	Bg%	Motif
1e-5308	26.16%	4.95%	TRE
1e-4279	35.59%	11.36%	PU.1
1e-760	12.89%	5.74%	CEBP
1e-376	15.95%	9.91%	EGR
1e-313	12.20%	7.35%	RUNX



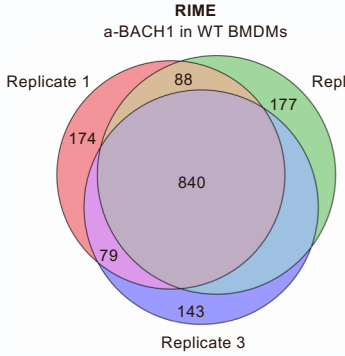


Figure S1. BACH1 cistrome analysis in naïve macrophages, related to Figure 1.

(A) The table contains the number of the predicted peaks from the MF-specific TF ChIP-seq samples, and in the case of BACH1, the consensus peakset (present in at least 2 samples from 8 unstimulated samples. The number of promoters and enhancer from the pool of these binding sites are also indicated.

(B) Upset plots representing the unique and common target sites of the cistromes of the shown TFs in untreated BMDMs in distal elements and promoters.

(C) TF peak overlap statistical analysis (Fischer's exact test).

(D) The coverage values (as RPKM) of BACH1 TF binding sites (n=73,428) are sorted and separated into large, medium, and small sites.

(E) IGV visualization of BACH1 ChIP-seq coverages on representative large, medium, and small BACH1 TF binding sites. The interval scales and the distances from the closest gene TSS are highlighted in all cases.

(F) The pie charts show the number of the small, medium, and large BACH1 peaks that contain MARE, or TRE, or both MARE and TRE motifs within their middle 200-bp regions.

(G) *De novo* motif enrichment of large, medium, and small BACH1 TF binding sites.

(H) Violin plots represent the motif score of MARE and TRE within the summit 200-bp region of large, medium, and small BACH1 TF binding sites. The number of identified motifs is also indicated.

(I) Number of peptides identified by a-BACH1 RIME in untreated WT BMDMs (n=3).

Figure S2.

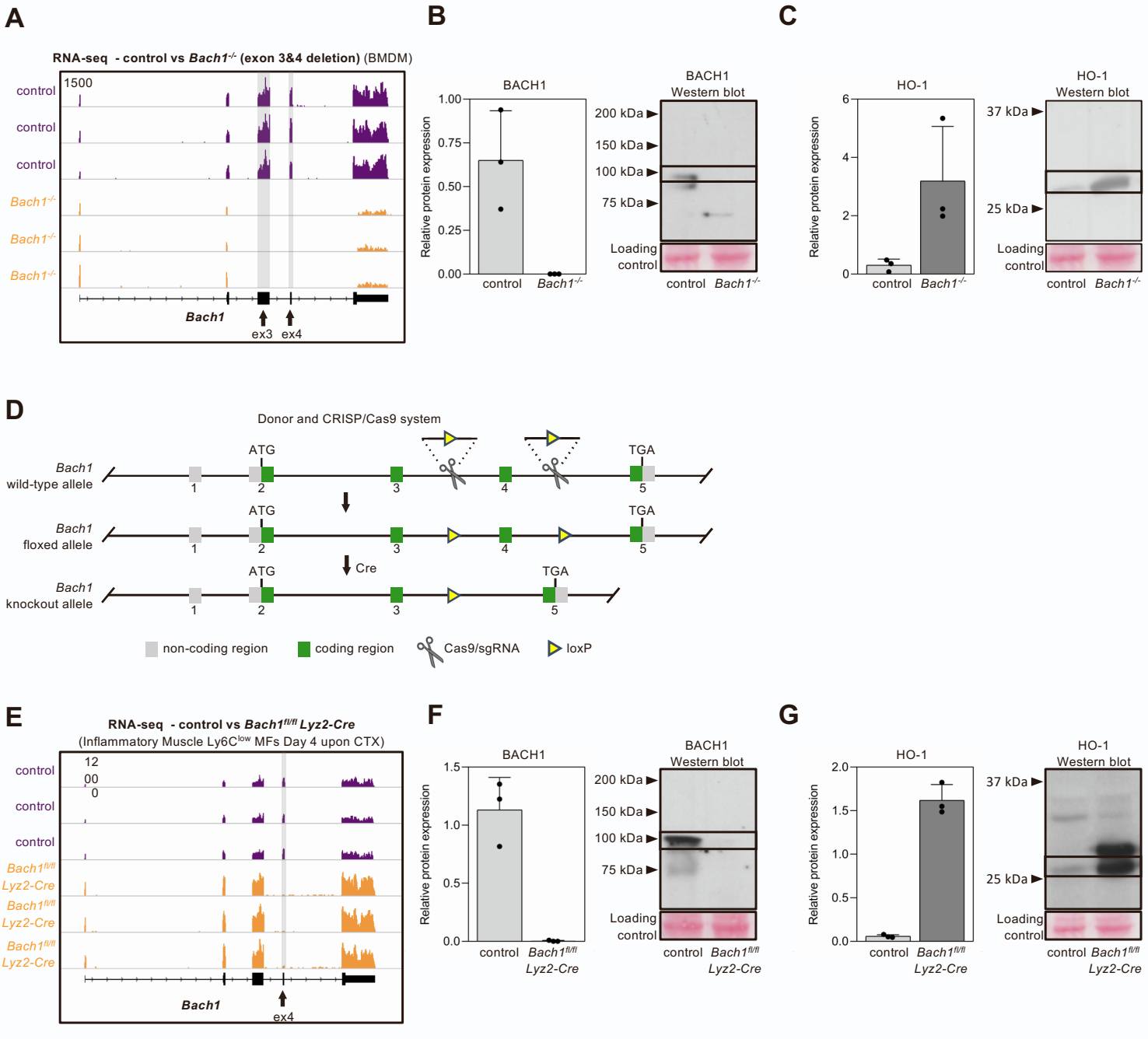

A
RNA-seq - control vs Bach1-/- (exon 3&4 deletion) (BMDM)
control
control
control
Bach1-/-
Bach1-/-
Bach1-/-
1500
Bach1
ex3
ex4
B
BACH1
Relative protein expression
1.00
0.75
0.50
0.25
0.00
control
Bach1-/-
BACH1
Western blot
200 kDa
150 kDa
100 kDa
75 kDa
Loading control
control
Bach1-/-
C
HO-1
Relative protein expression
6
4
2
0
control
Bach1-/-
HO-1
Western blot
37 kDa
25 kDa
Loading control
control
Bach1-/-
D
Donor and CRISP/Cas9 system
Bach1 wild-type allele
Bach1 floxed allele
Bach1 knockout allele
ATG
TGA
Cre
1
2
3
4
5
non-coding region
coding region
Cas9/sgRNA
loxP
E
RNA-seq - control vs Bach1fl/fl Lyz2-Cre
(Inflammatory Muscle Ly6Clow MFs Day 4 upon CTX)
control
control
control
Bach1fl/fl Lyz2-Cre
Bach1fl/fl Lyz2-Cre
Bach1fl/fl Lyz2-Cre
12
00
0
Bach1
ex4
F
BACH1
Relative protein expression
1.5
1.0
0.5
0.0
control
Bach1fl/fl Lyz2-Cre
BACH1
Western blot
200 kDa
150 kDa
100 kDa
75 kDa
Loading control
control
Bach1fl/fl Lyz2-Cre
G
HO-1
Relative protein expression
2.0
1.5
1.0
0.5
0.0
control
Bach1fl/fl Lyz2-Cre
HO-1
Western blot
37 kDa
25 kDa
Loading control
control
Bach1fl/fl Lyz2-Cre

Figure S2. New full-body and conditional Bach1 knock-out mice, related to STAR methods.

(A) IGV visualization of RNA-seq coverages of *Bach1* gene in control and *Bach1*$^{-/-}$ BMDMs. The knocked-out exons (3 and 4) are highlighted in grey. The interval scale is also highlighted for the represented genomic region.

(B) Western blot of BACH1 expression in control and *Bach1*$^{-/-}$ BMDMs. Bar graphs show mean values of the relative protein expression. Experiments were repeated three times. One representative blot is shown. Total protein serves as a loading control. Error bars represent +SD.

(C) Western blot of HO-1 expression in control and *Bach1*$^{-/-}$ BMDMs. Experiments were repeated three times. One representative blot is shown. Total protein serves as a loading control. Error bars represent +SD.

(D) Schematic visualization of the generation of *Bach1*$^{fl/fl}$*Lyz2-Cre mice.*

(E) IGV visualization of RNA-seq coverages of *Bach1* gene in control and *Bach1*$^{fl/fl}$*Lyz2-Cre* BMDMs. The floxed exon 4 is highlighted in grey. The interval scale is also highlighted for the represented genomic region.

(F) Western blot of BACH1 expression in control and *Bach1*$^{fl/f}$ *Lyz2-Cre* BMDMs. Bar graphs show mean values of the relative protein expression. Experiments were repeated three times. One representative blot is shown. Total protein serves as a loading control. Error bars represent +SD.

(G) Western blot of HO-1 expression in control and *Bach1*$^{fl/fl}$*Lyz2-Cre* BMDMs. Bar graphs show mean values of the relative protein expression. Experiments were repeated three times. One representative blot is shown. Total protein serves as a loading control. Error bars represent +SD.

Figure S3.

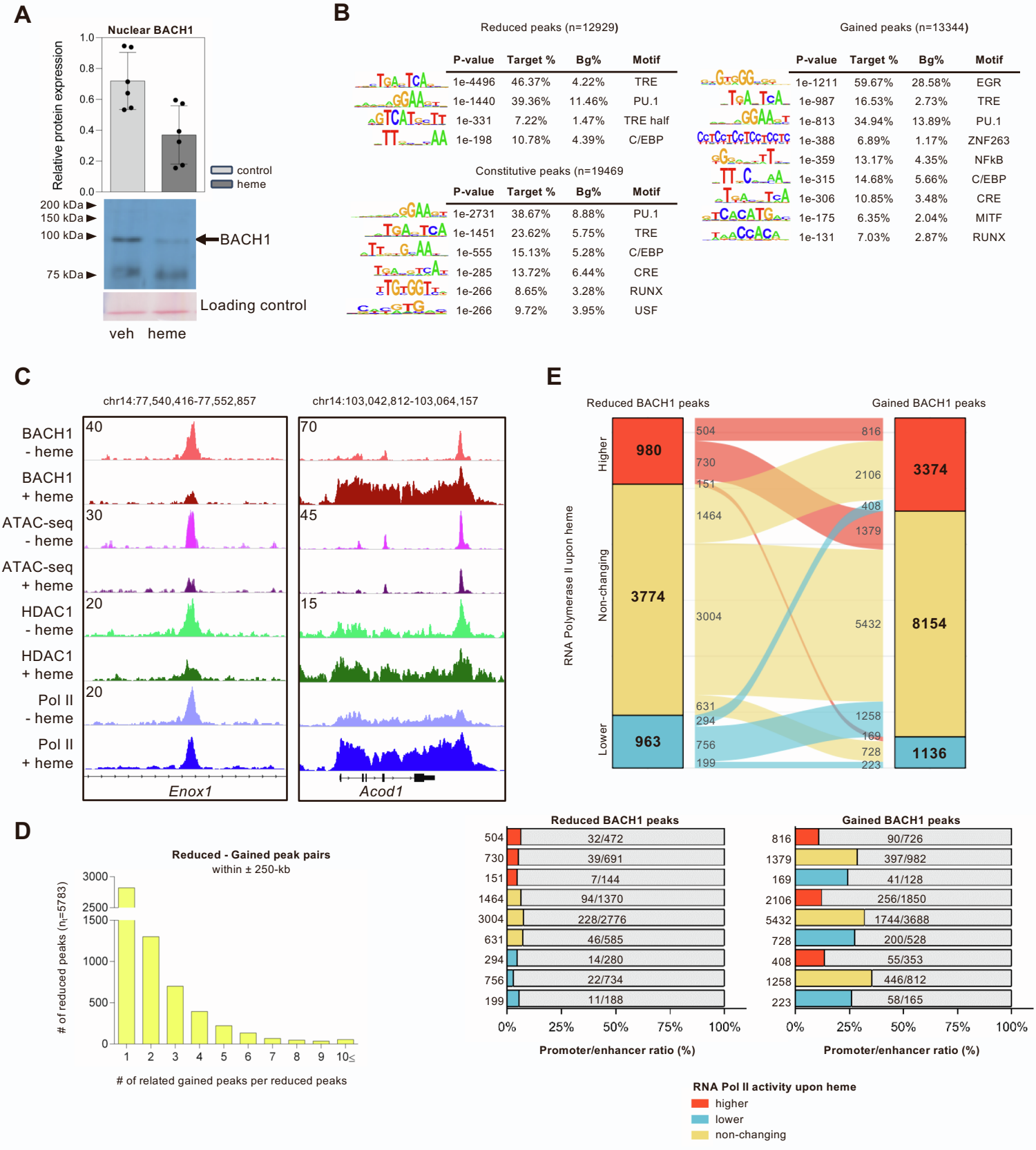

A
Nuclear BACH1
Relative protein expression
control
heme
200 kDa
150 kDa
100 kDa
75 kDa
BACH1
Loading control
veh
heme
B
Reduced peaks (n=12929)
P-value Target % Bg% Motif
1e-4496 46.37% 4.22% TRE
1e-1440 39.36% 11.46% PU.1
1e-331 7.22% 1.47% TRE half
1e-198 10.78% 4.39% C/EBP
Constitutive peaks (n=19469)
P-value Target % Bg% Motif
1e-2731 38.67% 8.88% PU.1
1e-1451 23.62% 5.75% TRE
1e-555 15.13% 5.28% C/EBP
1e-285 13.72% 6.44% CRE
1e-266 8.65% 3.28% RUNX
1e-266 9.72% 3.95% USF
Gained peaks (n=13344)
P-value Target % Bg% Motif
1e-1211 59.67% 28.58% EGR
1e-987 16.53% 2.73% TRE
1e-813 34.94% 13.89% PU.1
1e-388 6.89% 1.17% ZNF263
1e-359 13.17% 4.35% NFkB
1e-315 14.68% 5.66% C/EBP
1e-306 10.85% 3.48% CRE
1e-175 6.35% 2.04% MITF
1e-131 7.03% 2.87% RUNX
C
chr14:77,540,416-77,552,857
chr14:103,042,812-103,064,157
BACH1 - heme
BACH1 + heme
ATAC-seq - heme
ATAC-seq + heme
HDAC1 - heme
HDAC1 + heme
Pol II - heme
Pol II + heme
Enox1
Acod1
D
Reduced - Gained peak pairs
within ± 250-kb
of reduced peaks (n=5783)
of related gained peaks per reduced peaks
E
Reduced BACH1 peaks
Gained BACH1 peaks
RNA Polymerase II upon heme
Higher
Non-changing
Lower
980
3774
963
3374
8154
1136
Promoter/enhancer ratio (%)
RNA Pol II activity upon heme
higher
lower
non-changing

Figure S3. Heme-elicited changes in BACH1 protein expression and cistrome, related to Figure 2.

(A) Western blot of nuclear BACH1 expression in the vehicle and heme-treated BMDM. Bar graphs show mean values of the relative protein expression. Total protein serves as a loading control. Error bars represent +SD (n=6)

(B) *De novo* motif enrichment of repressed, constitutive, and gained BACH1 binding sites.

(C) Genome browser examples of BACH1 & HDAC1 ChIP-seq, ATAC-seq and RNA-PolII ChIP-seq before and upon heme.

(D) The bar chart represents the number of the reduced BACH1 binding sites as a function of the number of gained peaks (from 1 to 10<) assigned to them.

(E) Sankey diagram shows the pairing of genomic regions with reduced BACH1 binding to nearby regions with gained BACH1 binding upon heme treatment, colored by associated changes in RNA PolII Ser2P ChIP-seq signal. Note that more than one gained peak can be associated with a reduced peak and that all reduced BACH1 peaks connect to gained BACH1 sites with either higher transcriptional activity or no change.

Figure S4.

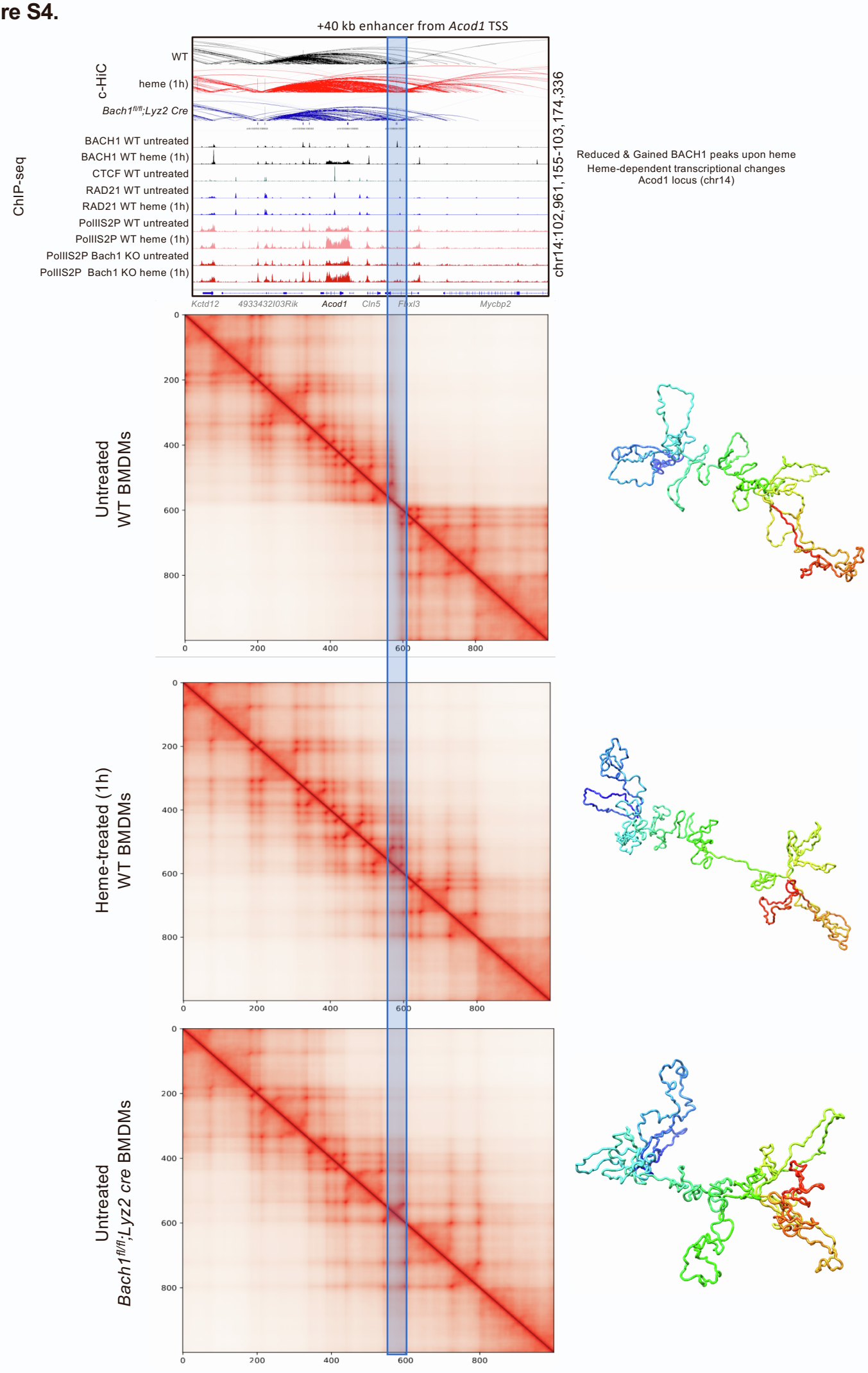
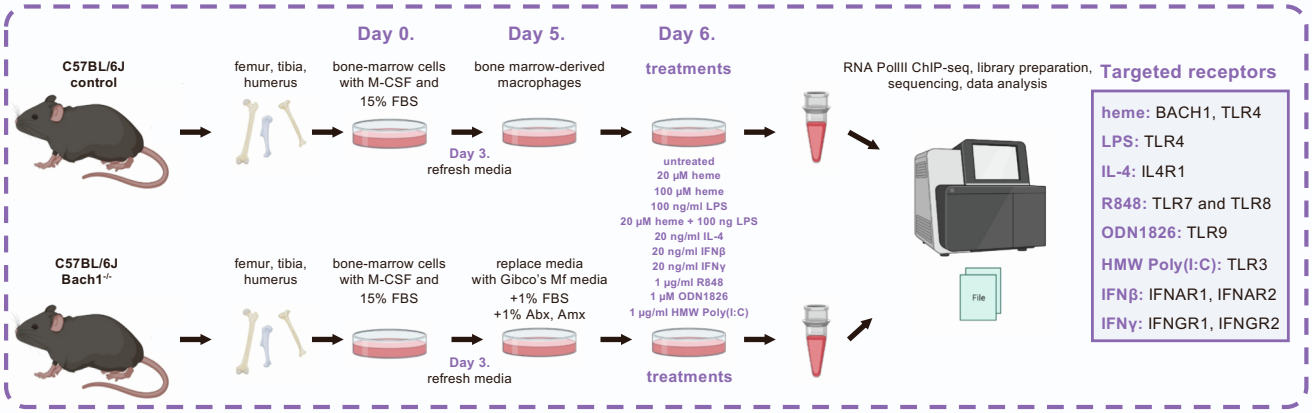

+40 kb enhancer from Acod1 TSS
c-HiC
WT
heme (1h)
Bach1fl/fl;Lyz2 Cre
ChIP-seq
BACH1 WT untreated
BACH1 WT heme (1h)
CTCF WT untreated
RAD21 WT untreated
RAD21 WT heme (1h)
PolIIS2P WT untreated
PolIIS2P WT heme (1h)
PolIIS2P Bach1 KO untreated
PolIIS2P Bach1 KO heme (1h)
chr14:102,961,155-103,174,336
Reduced & Gained BACH1 peaks upon heme
Heme-dependent transcriptional changes
Acod1 locus (chr14)
Kctd12
4933432I03Rik
Acod1
Cln5
Fbxl3
Mycbp2
Untreated WT BMDMs
Heme-treated (1h) WT BMDMs
Untreated Bach1fl/fl;Lyz2 cre BMDMs
0
200
400
600
800

Figure S4. LoopSage Simulation of Chromatin Dynamics at the *Acod1* Locus, related to Figure 3.

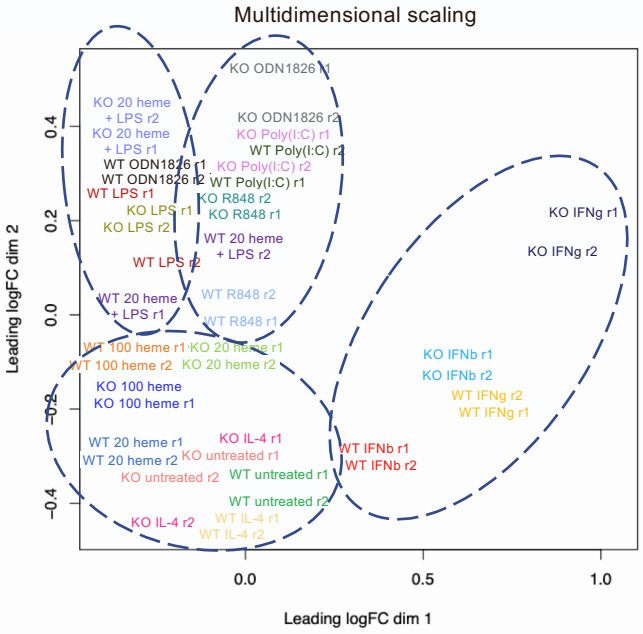
Predicted contact maps and polymer simulations based on LoopSage pipeline[29] in *Acod1* locus in untreated, heme stimulated and *Bach1*-deficient BMDMs.

Figure S5.

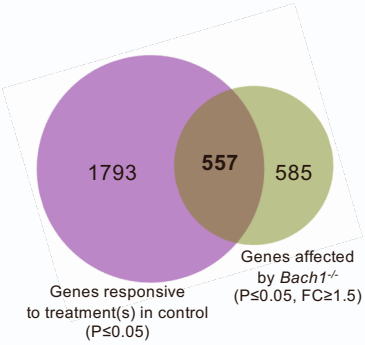
A



B



C



D

2,350 unique genes

Genes with different PolII activity in control (P≤0.05)

untreated vs. treated	DEGs
untreated vs 100ng LPS	1100
untreated vs 100μM heme	683
untreated vs 10ng IFNβ	1011
untreated vs 10μg HMW poly(I:C)	953
untreated vs 1μg R848	868
untreated vs 1M ODN1826	1068
untreated vs 20ng IFNγ	1070
untreated vs 20ng IL-4	615
untreated vs 20μM heme + 100ng LPS	1023
untreated vs 20μM heme	471

E

1,142 unique genes

Genes with different PolII activity between control and *Bach1*$^{-/-}$ (P≤0.05; FC≥1.5)

control vs. *Bach1*$^{-/-}$	DEGs
untreated	128
100ng LPS	113
100μM heme	75
20ng IFNβ	111
10μg HMW poly(I:C)	185
R848	202
1μM ODN1826	419
20ng IFNγ	340
20ng IL-4	105
20μM heme + 100ng LPS	200
20μM heme	179

F

***De novo* motif enrichment of the clusters' associated regulatory regions**

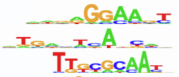
	P-value	Target %	Bg%	Motif	
	1e-33	34.34 %	7.87 %	PU.1	C1
	1e-23	10.94 %	0.74 %	MARE	
	1e-52	42.86 %	15.40 %	PU.1	C2
	1e-36	19.71 %	4.67 %	TRE	
	1e-17	9.58%	2.20 %	CEBP	
	1e-27	13.20 %	0.85 %	MARE	C3
	1e-20	19.20 %	3.66 %	PU.1	
	1e-10	12.00 %	2.94 %	CEBP	
	1e-17	16.26 %	1.08 %	PU.1	C4
	1e-14	9.76 %	0.28 %	Myb	
	1e-14	13.01 %	0.81 %	TRE	
	1e-20	60.00%	24.11 %	PU.1	C5
	1e-16	13.55 %	1.03 %	MARE	
	1e-15	5.16 %	0.03 %	EICE	
	1e-12	19.35 %	3.76 %	ETS	
	1e-74	24.29 %	4.37 %	TRE	C6
	1e-67	33.24 %	9.37 %	PU.1	
	1e-40	23.44 %	7.31 %	CEBP	
	1e-17	5.40 %	0.88 %	MARE	
	1e-107	39.03 %	11.39 %	PU.1	C7
	1e-60	16.56 %	3.40 %	IRF	
	1e-52	21.33 %	6.29 %	TRE	
	1e-29	10.66 %	2.82 %	CEBP	
	1e-30	14.73 %	1.73 %	ETS	C8
	1e-19	12.75 %	2.23 %	MARE	
	1e-16	15.01 %	3.72 %	CEBP	
	1e-56	29.19 %	7.51 %	PU.1	C9
	1e-43	22.79 %	5.72 %	TRE	
	1e-32	9.02 %	1.02 %	CEBP	
	1e-12	9.34 %	3.03 %	NFkB	
	1e-164	46.84 %	15.87%	PU.1	C10
	1e-115	23.74 %	5.50 %	TRE	
	1e-87	24.44 %	7.38 %	CEBP	
	1e-24	12.22 %	5.20 %	RUNX	
	1e-22	16.15 %	8.18 %	CRE	
	1e-21	4.71%	1.12 %	NFkB	
	1e-16	8.78 %	3.80 %	MEF2	
	1e-16	10.74 %	5.19 %	IRF	
	1e-130	40.47 %	13.43 %	PU.1	C11
	1e-110	20.35 %	3.86 %	TRE	
	1e-63	21.21 %	6.81 %	CEBP	
	1e-14	20.12 %	12.39 %	IRF	
	1e-126	40.08 %	13.21 %	PU.1	C12
	1e-86	11.32 %	1.28 %	MARE	
	1e-56	22.64 %	8.19 %	CEBP	
	1e-22	15.74 %	7.49 %	CRE	
	1e-20	3.18 %	0.47 %	EICE	
	1e-17	10.08 %	4.31 %	RUNX	

Figure S5. BACH1-dependent impact on transcriptional regulation upon multiple MF activation agents, related to Figure 4.

(A) Schematic representation of the experimental design of the PolIISer2 ChIP-seq experiments in BMDMs treated with multiple MF activation agents.

(B) Multidimensional scaling represents the Euclidean distances between the untreated and treated RNA Polymerase II ChIP-seq samples in control and *Bach1*$^{-/-}$ BMDMs. For the comparison, the normalized coverage values calculated on the promoters (TSS+100-kb) were used.

(C) The proportional Venn diagram depicts the overlap between the genes, significantly responsive ($p \leq 0.05$) to any of the applied treatments in control and genes, significantly affected by *Bach1*$^{-/-}$ ($p \leq 0.05$ and $FC \geq 1.5$) upon any of the applied treatments. **(D, E)** The table contains the number of genes with **(D)** significantly different RNA Polymerase II activity between untreated and treated BMDMs ($p \leq 0.05$) and between **(E)** control and *Bach1*$^{-/-}$ BMDMs upon different treatments ($p \leq 0.05$ and $FC \geq 1.5$).

(F) *De novo* motif enrichment of the BACH1 peaks, associated with the C1-C12 clusters' genes (TSS±100-kb), defined in Figure 4E.

Figure S6.

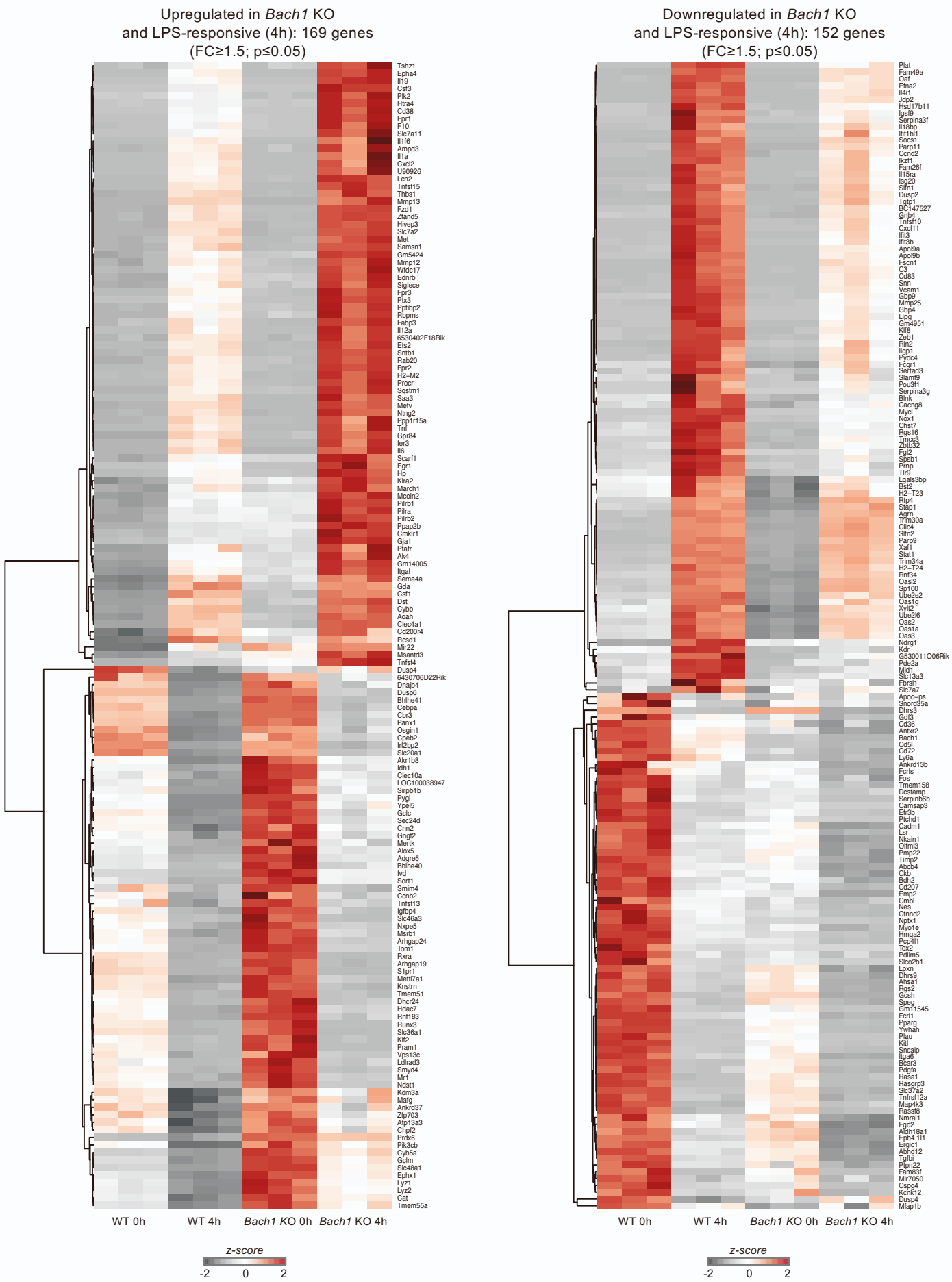

Upregulated in *Bach1* KO
and LPS-responsive (4h): 169 genes
(FC≥1.5; p≤0.05)
Tshz1
Epha4
Il19
Csf3
Plk2
Htra4
Cd38
Fpr1
F10
Slc7a11
Il1f6
Ampd3
Il1a
Cxcl2
U90926
Lcn2
Tnfsf15
Thbs1
Mmp13
Fzd1
Zfand5
Hivep3
Slc7a2
Met
Samsn1
Gm5424
Mmp12
Wfdc17
Ednrb
Siglece
Fpr3
Ptx3
Pglfbp2
Rbpms
Fabp3
Il12a
6530402F18Rik
Ets2
Sntb1
Rab20
Fpr2
H2−M2
Procr
Sqstm1
Saa3
Mefv
Ntng2
Ppp1r15a
Tnf
Gpr84
Ier3
Il6
Scarf1
Egr1
Hp
Kira2
March1
Mcoln2
Pilrb1
Pilra
Pilrb2
Ppap2b
Cmklr1
Gja1
Ptafr
Ak4
Gm14005
Itgal
Sema4a
Gda
Csf1
Dst
Cybb
Aoah
Clec4a1
Cd200r4
Rcsd1
Mir22
Msantd3
Tnfsf4
Dusp4
6430706D22Rik
Dnajb4
Dusp6
Bhlhe41
Cebpa
Cbr3
Panx1
Qsgin1
Cpeb2
Irf2bp2
Slc20a1
Akr1b8
Idh1
Clec10a
LOC100038947
Sirpb1b
Pygl
Ypel5
Gclc
Sec24d
Cnn2
Gngt2
Mertk
Alox5
Adgre5
Bhlhe40
Ivd
Sort1
Smim4
Ccnb2
Tnfsf13
Igfbp4
Slc46a3
Nxpe5
Msrb1
Arhgap24
Tom1
Rxra
Arhgap19
S1pr1
Mettl7a1
Knstrn
Tmem51
Dhcr24
Hdac7
Rnf183
Runx3
Slc36a1
Klf2
Pram1
Vps13c
Ldlrad3
Smyd4
Mr1
Ndst1
Kdm3a
Mafg
Ankrd37
Zfp703
Atp13a3
Chpf2
Prdx6
Pik3cb
Cyb5a
Oclm
Slc48a1
Ephx1
Lyz1
Lyz2
Cat
Tmem55a
WT 0h
WT 4h
Bach1 KO 0h
Bach1 KO 4h
z-score
-2
0
2
Downregulated in *Bach1* KO
and LPS-responsive (4h): 152 genes
(FC≥1.5; p≤0.05)
Plat
Fam49a
Oaf
Efna2
Il4i1
Jdp2
Hsd17b11
Igsf9
Serpina3f
Il18bp
Ifit1bl1
Socs1
Parp11
Ccnd2
Ikzf1
Fam26f
Il15ra
Isg20
Slfn1
Dusp2
Tgtp1
BC147527
Gnb4
Tnfsf10
Cxcl11
Ifit3
Ifit3b
Apol8a
Apol9b
Fscn1
C3
Cd83
Snn
Vcam1
Gbp9
Mmp25
Gbp4
Lpg
Gm4951
Klf8
Zeb1
Rin2
Iigp1
Pydc4
Fcgr1
Selftad3
Slamf9
Pou3f1
Serpina3g
Blnk
Cacng8
Mycl
Nox1
Chst7
Rgs16
Tmcc3
Zbtb32
Fgl2
Sgsb1
Prnp
Tlr9
Lgals3bp
Bst2
H2−T23
Ptpt4
Stap1
Agrn
Trim30a
Clic4
Slfn2
Parp9
Xaf1
Stat1
Trim34a
H2−T24
Rnf34
Oasl2
Sp100
Ube2e2
Oas1g
Xylt2
Ube2l6
Oas2
Oas1a
Oas3
Ndrg1
Kdr
G530011O06Rik
Pde2a
Mid1
Slc13a3
Fbrsl1
Slc7a7
Apoo−ps
Snord35a
Dhrs3
Gdf3
Cd36
Anbr2
Bach1
Cd5l
Cd72
Ly6a
Ankrd13b
Fcrls
Fos
Tmem158
Dcstamp
Serpinb6b
Camsap3
Efr3b
Ptchd1
Cadm1
Lsr
Nkain1
Olfml3
Pmp22
Timp2
Abcb4
Ckb
Bdh2
Cd207
Emp2
Cmbl
Nes
Ctnnd2
Nptx1
Myo1e
Hmga2
Pcp4l1
Tox2
Pdlim5
Slco2b1
Lpxn
Dhrs9
Ahsa1
Rgs2
Gcsh
Speg
Gm11545
Fcrl1
Pparg
Ywhah
Plau
Kitl
Sncaip
Itga6
Bcar3
Pdgfa
Rasa1
Rasgrp3
Slc37a2
Tnfrsf12a
Mag4k3
Rassf8
Nmral1
Fgd2
Adh18a1
Epb4.1l1
Ergic1
Abhd12
Tgfbi
Ptpn22
Fam83f
Mir7050
Cspg4
Kcnk12
Dusp4
Mtap1b
WT 0h
WT 4h
Bach1 KO 0h
Bach1 KO 4h
z-score
-2
0
2

Figure S6. BACH1-dependent and LPS-responsive genes, related to Figure 5.

Heatmaps with differentially expressed genes (p≤0.05 , FC>1.5) between the control and *Bach1*$^{-/-}$ BMDMs upon LPS stimulation (4h).

Figure S7.

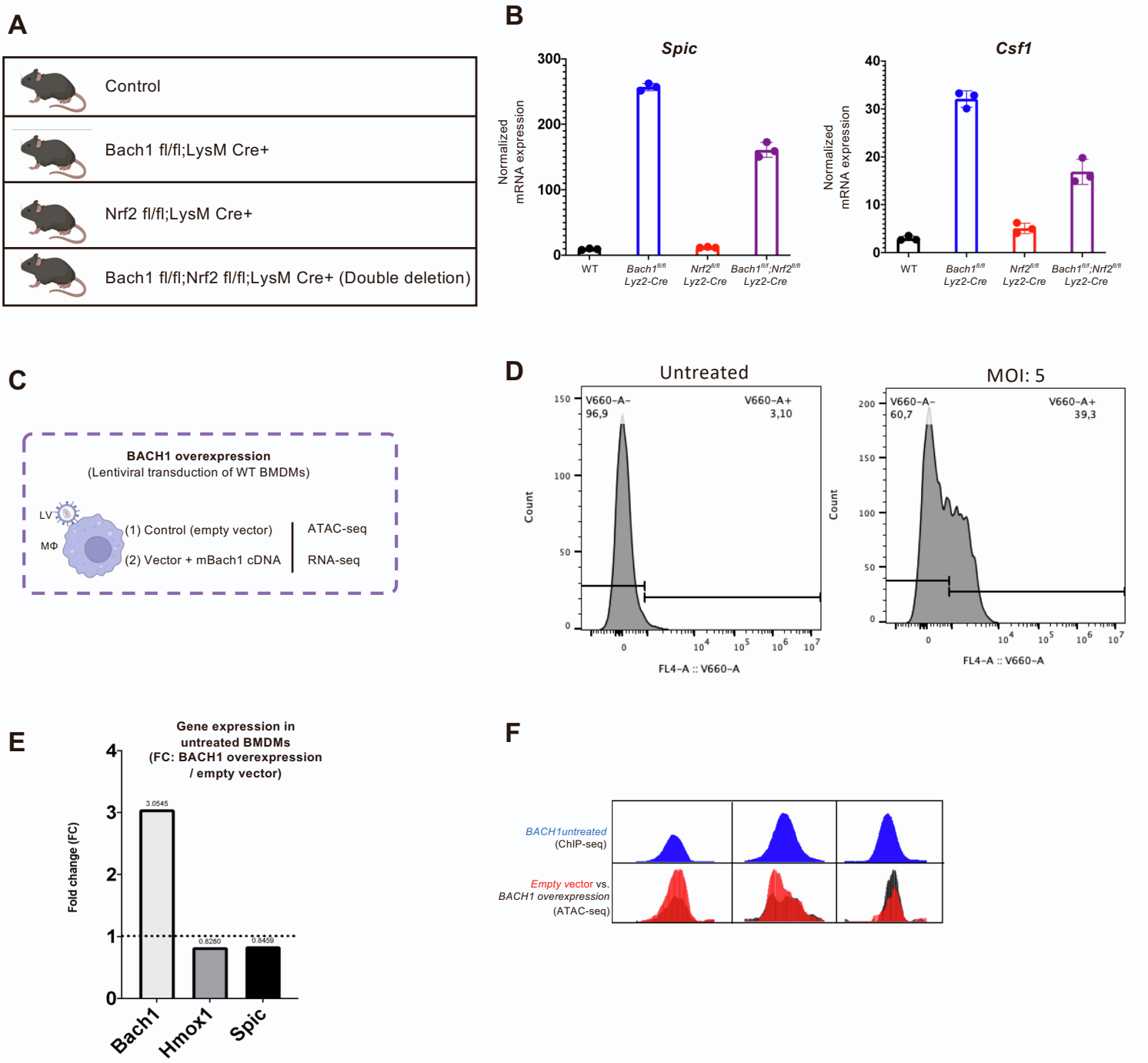

A
Control
Bach1 fl/fl;LysM Cre+
Nrf2 fl/fl;LysM Cre+
Bach1 fl/fl;Nrf2 fl/fl;LysM Cre+ (Double deletion)
B
Spic
Csf1
Normalized mRNA expression
WT
Bach1fl/fl Lyz2-Cre
Nrf2fl/fl Lyz2-Cre
Bach1fl/fl;Nrf2fl/fl Lyz2-Cre
C
BACH1 overexpression
(Lentiviral transduction of WT BMDMs)
LV
MΦ
(1) Control (empty vector)
(2) Vector + mBach1 cDNA
ATAC-seq
RNA-seq
D
Untreated
MOI: 5
V660-A-
V660-A+
96,9
3,10
60,7
39,3
Count
FL4-A :: V660-A
E
Gene expression in untreated BMDMs (FC: BACH1 overexpression / empty vector)
Fold change (FC)
3.0545
0.8280
0.8459
Bach1
Hmox1
Spic
F
BACH1untreated (ChIP-seq)
Empty vector vs. BACH1 overexpression (ATAC-seq)

Figure S7. Sufficiency of BACH1 in gene repression and efficiency of lentiviral transduction in BMDMs, related to Figure 5.

(A) Outline of the genotypes of myeloid *Bach1*, *Nrf2* and double-deficient mice used in Figure 5G.

(B) RT-qPCR analysis of *SpiC* and *Csf1* expression in control, *Bach1*, *Nrf2* and Double deficient BMDMs (n = 3).

(C) Experimental plan for BACH1 overexpression with lentiviral transduction of WT BMDMs.

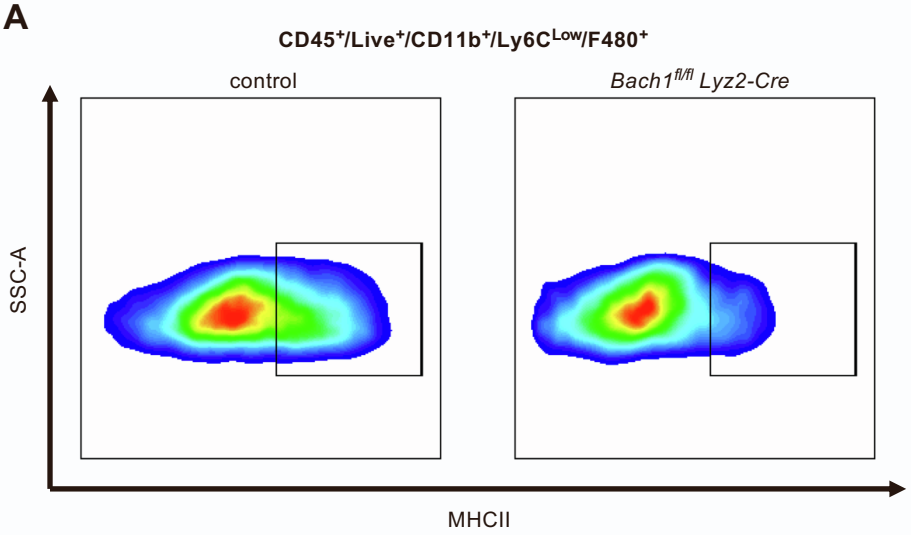
(D) FACS analysis of the efficiency of lentiviral transduction in WT BMDMs with control RFP expressing plasmid vectors (MOI:5).

(E) RT-qPCR for *Bach1*, *Hmox1*, *Spic* genes in lentiviral transduced of WT BMDMs with plasmid vector overexpressing BACH1 (n=3).

(F) Representative examples of altered chromatin accessibility kinetics following BACH1 overexpression.

Figure S8.

A

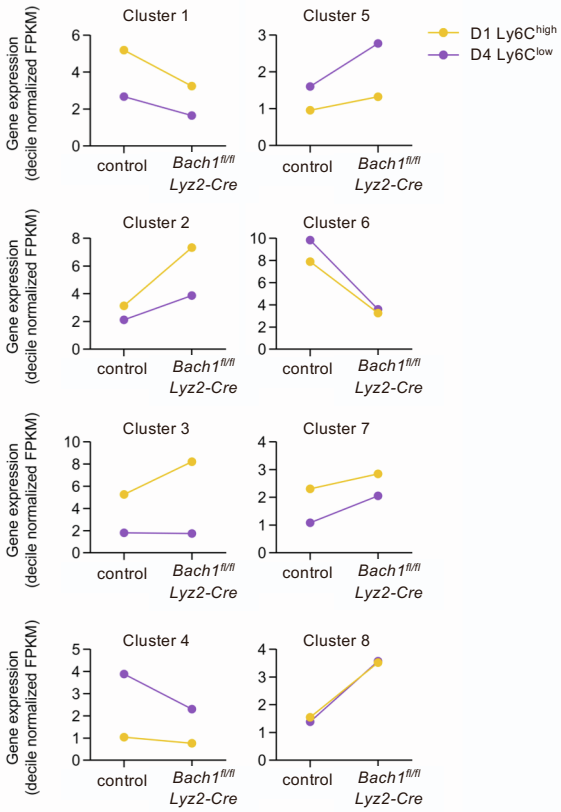


B

RNA-seq

control vs. *Bach1*$^{fl/fl}$ *Lyz2-Cre*	Upregulated in *Bach1*$^{fl/fl}$ *Lyz2-Cre*	Downregulated in *Bach1*$^{fl/fl}$ *Lyz2-Cre*
Day 1 Ly6C^{high}	345	267
Day 4 Ly6C^{low}	482	459

C

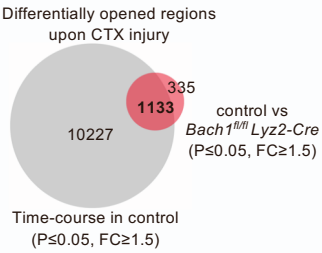


D

ATAC-seq

Time-course in control	DORs	
D1 Ly6C^{high} vs. D2 Ly6C^{high}	296	
D1 Ly6C^{high} vs. D2 Ly6C^{low}	2749	
D1 Ly6C^{high} vs. D4 Ly6^{high}	3269	
D1 Ly6C^{high} vs. D4 Ly6C^{low}	3751	**11360**
D2 Ly6C^{high} vs. D2 Ly6C^{low}	1863	
D2 Ly6C^{high} vs. D4 Ly6C^{high}	2926	
D2 Ly6C^{low} vs. D4 Ly6C^{low}	3777	
D4 Ly6C^{high} vs. D4 Ly6C^{low}	2332	
control vs. *Bach1*$^{fl/fl}$ *Lyz2-Cre*		
D1 Ly6C^{high} vs. D1 Ly6C^{high}	131	
D2 Ly6C^{high} vs. D2 Ly6C^{high}	19	
D2 Ly6C^{low} vs. D2 Ly6C^{low}	652	**1468**
D4 Ly6C^{high} vs. D4 Ly6C^{high}	435	
D4 Ly6C^{low} vs. D4 Ly6C^{low}	299	

E



F

RNA-seq - DEGs cluster	Associated ATAC-seq peaks
#1	14
#2	80
#3	35
#4	64
#5	38
#6	32
#7	20
#8	53
	Total= 336

Figure S8. FACS, RNA-seq & ATAC-seq analysis in macrophages during CTX-induced muscle injury in control and control and *Bach1*$^{fl/f}$ *Lyz2-Cre*, related to Figure 6.

(A) Representative FACS plot of MHCII expression in MFs (CD45^{+}/Live^{+}/CD11b^{+}/Ly6C^{Low}/F480^{+}) from CTX-injured TA mucscles (Day4 post CTX) in control and *Bach1*$^{fl/f}$ *Lyz2-Cre.*

(B) The table contains the number of significantly (p≤0.05 and FC≥1.5) up- and downregulated genes between control and *Bach1*$^{fl/fl}$*Lyz2-Cre* TA muscle samples at day 1 Ly6C^{high} and day 4 Ly6C^{low} cell populations after cardiotoxin (CTX) injury.

(C) The line plots represent the decile normalized average gene expression (as FPKM) level of the defined 8 clusters in control and *Bach1*$^{fl/fl}$*Lyz2-Cre* samples both at day 1 Ly6C^{high} (yellow) and day 4 Ly6C^{low} (purple) cell populations.

(D) The top table contains the number of differentially (p≤0.05 and FC≥1.5) accessible chromatin regions between day 1 Ly6C^{high}, day 2 and 4 Ly6C^{high} and Ly6C^{low} cell populations after CTX injury in control, while the bottom table contains the number of differentially (p≤0.05 and FC≥1.5) accessible chromatin regions between control and *Bach1*$^{fl/fl}$*Lyz2-Cre* TA muscle samples in day 1 Ly6C^{high}, day 2 and 4 Ly6C^{high} and Ly6C^{low} cell populations after CTX injury. The total number of individual regions is also highlighted in both cases.

(E) The proportional Venn diagram depicts the overlap between the differentially opened chromatin regions in control and control vs. *Bach1*$^{fl/fl}$*Lyz2-Cre* samples.

Figure S9.

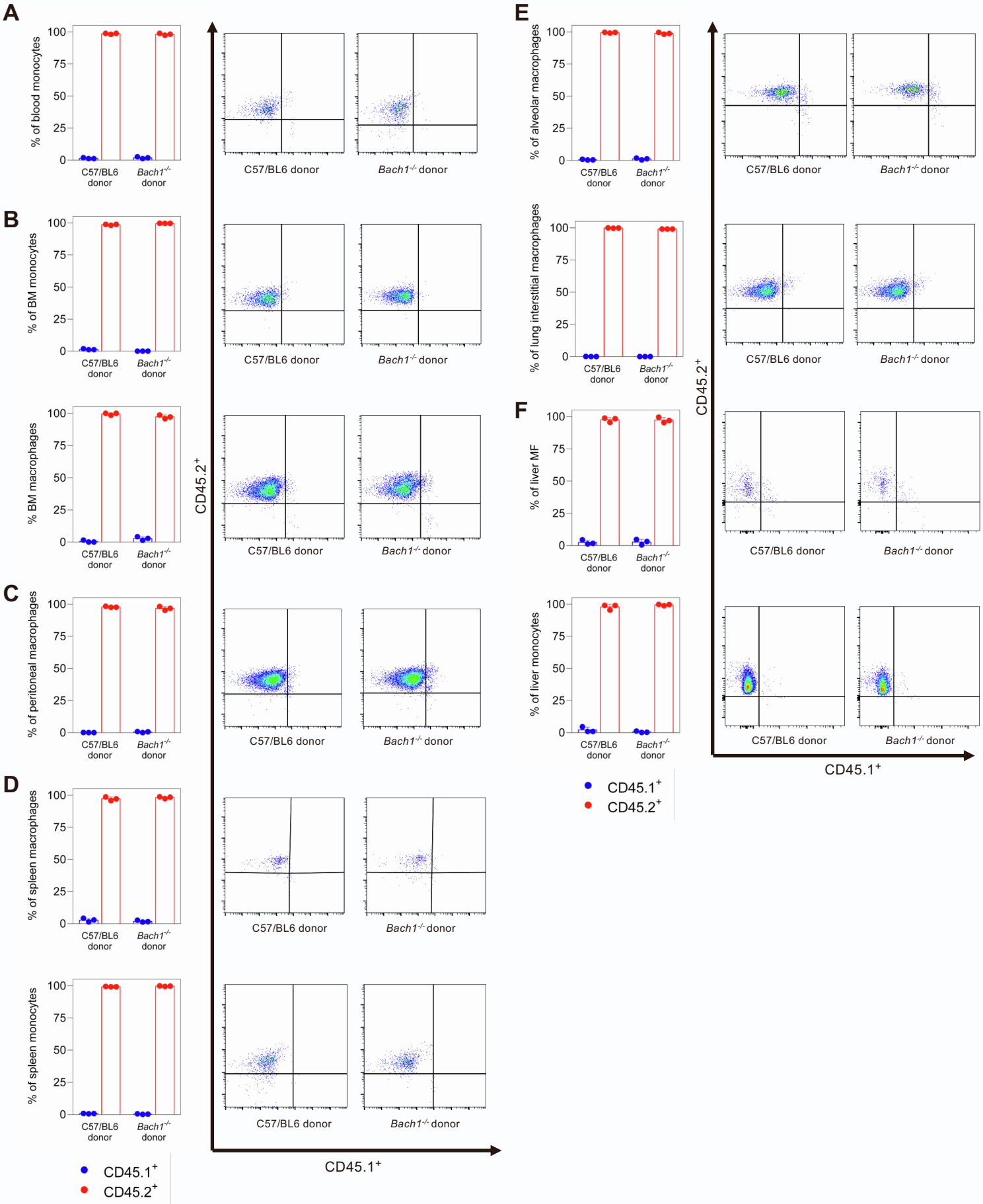

A
% of blood monocytes
B
% of BM monocytes
% BM macrophages
C
% of peritoneal macrophages
D
% of spleen macrophages
% of spleen monocytes
E
% of alveolar macrophages
% of lung interstitial macrophages
F
% of liver MF
% of liver monocytes
C57/BL6 donor
Bach1-/- donor
CD45.2+
CD45.1+
CD45.1+
CD45.2+

Figure S9. Flow cytometry of control and *Bach1*$^{-/-}$ tissue resident MFs upon bone marrow cell transplantation, related to Figure 7.

Flow cytometry data show the mean frequency values of CD45.1^{+} and CD45.2^{+} cell populations of **(A)** blood monocytes, **(B)** bone marrow monocytes and MFs, **(C)** large peritoneal MF, **(D)** spleen red pulp MF and spleen monocytes, **(E)** lung alveolar and interstitial MF, and **(F)** liver MF and monocytes. Dot plots show one representative mouse of eight mice. Error bars represent +SD.

Figure S10.

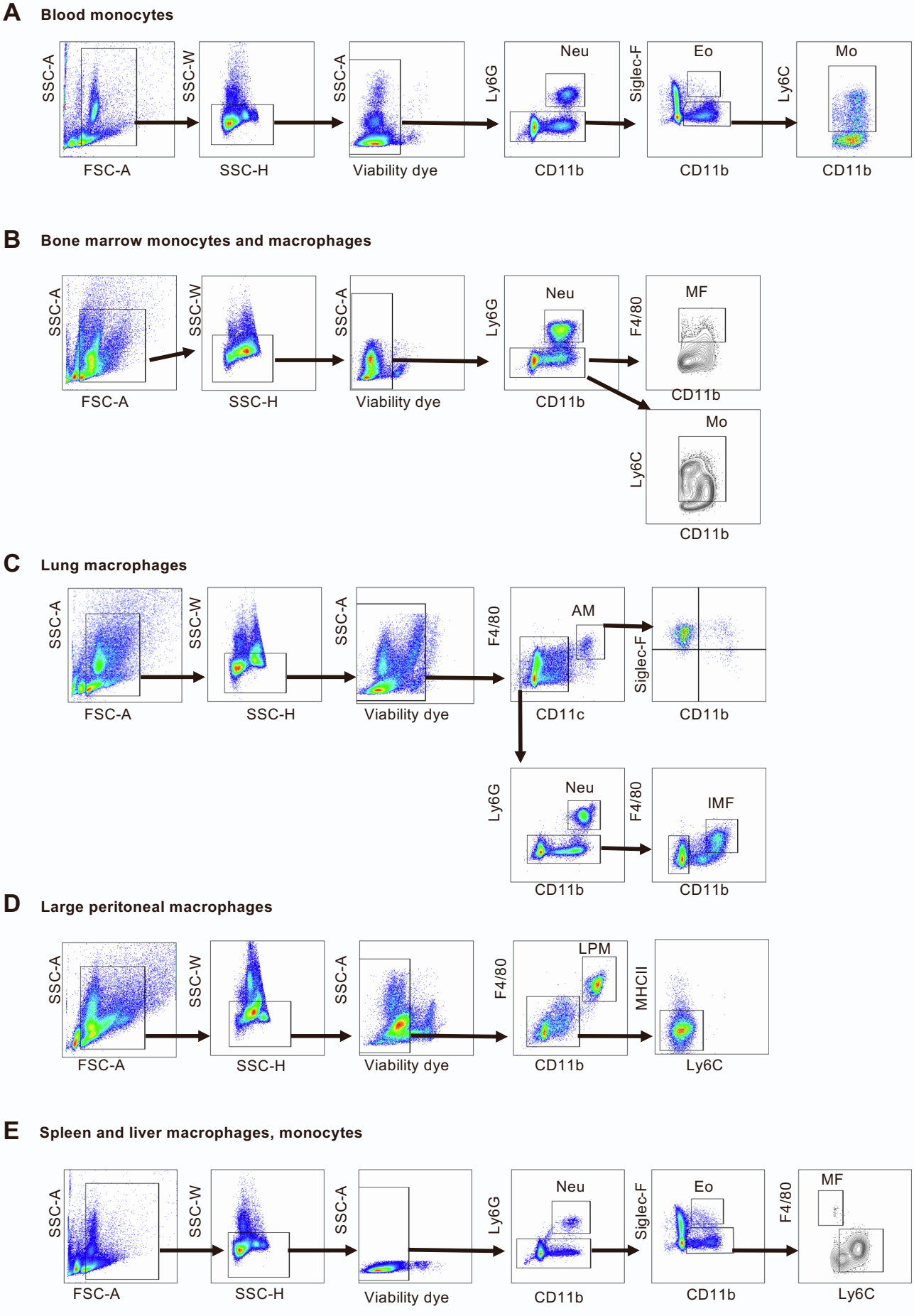

A
Blood monocytes
SSC-A
FSC-A
SSC-W
SSC-H
SSC-A
Viability dye
Ly6G
Neu
CD11b
Siglec-F
Eo
CD11b
Ly6C
Mo
CD11b
B
Bone marrow monocytes and macrophages
SSC-A
FSC-A
SSC-W
SSC-H
SSC-A
Viability dye
Ly6G
Neu
CD11b
F4/80
MF
CD11b
Ly6C
Mo
CD11b
C
Lung macrophages
SSC-A
FSC-A
SSC-W
SSC-H
SSC-A
Viability dye
F4/80
AM
CD11c
Siglec-F
CD11b
Ly6G
Neu
CD11b
F4/80
IMF
CD11b
D
Large peritoneal macrophages
SSC-A
FSC-A
SSC-W
SSC-H
SSC-A
Viability dye
F4/80
LPM
CD11b
MHCII
Ly6C
E
Spleen and liver macrophages, monocytes
SSC-A
FSC-A
SSC-W
SSC-H
SSC-A
Viability dye
Ly6G
Neu
CD11b
Siglec-F
Eo
CD11b
F4/80
MF
Ly6C

Figure S10. Gating strategy for tissue-derived myeloid cells by flow cytometry, related to Figure 7.

Each plot is gated in SSC-W^{lo}SSC-H^{lo} singlet and live cell fraction. CD11b^{+}Ly6G^{+} neutrophil granulocytes (Neu) and Siglec-F^{+}CD11b^{+} eosinophil granulocytes (Eo) are excluded during the gating.

(A) Blood monocytes (Mo) are Ly6G^{-}SiglecF^{-}CD11b^{+}Ly6C^{+}.

(B) Bone marrow macrophages (MF) are Ly6G^{-}SiglecF^{-}CD11b^{+}F4/80^{+}Ly6C^{-}, and monocytes are Ly6G^{-}SiglecF^{-}CD11b^{+}F4/80^{-}Ly6C^{+}.

(C) Lung alveolar macrophages (AM) are F4/80^{+}CD11c^{+}Siglec-F^{+}CD11b^{-}, and lung interstitial macrophages (IMF) are CD11c^{-}Ly6G^{-}F4/80^{med}CD11b^{+}.

(D) Large peritoneal macrophages are F4/80^{hi}CD11b^{hi}CD115^{hi}MHCII^{lo}Ly6C^{-}. Small peritoneal macrophages are F4/80^{med}CD11b^{med}CD115^{lo}MHCII^{hi}.

(E) Spleen red pulp macrophages are Ly6G^{-}Siglec-F^{-}CD11b^{lo}F4/80^{+}Ly6C^{-}. Splenic monocytes are Ly6G^{-}SiglecF^{-}F4/80^{-}CD11b^{+}Ly6C^{+}.